DEFINING DUB SPECIFICITY FOR THE CORONAVIRUS PAPAIN-LIKE PROTEASE

by

COURTNEY MARIE DACZKOWSKI

(Under the Direction of Scott Pegan)

ABSTRACT

Coronaviruses are single-stranded, positive-sense RNA viruses from the family *Coronaviridae*, whose members have severe impact on human health and cause significant economic hardships. Pertinent examples of coronaviruses include porcine epidemic diarrhea virus (PEDV), porcine deltacoronavirus (PDCoV), and severe acute and Middle East respiratory syndrome coronavirus (SARS-CoV; MERS-CoV). Interestingly, these viruses encode a dual functioning protease, the papain like-protease (PLP), that aids in RNA replication via processing of the viral polyprotein as well as antagonizes the host antiviral innate immune response. The latter function is achieved through the removal of post-translational modifications of host and viral proteins by ubiquitin (Ub) or Ub-like interferon-stimulated-gene-product-15 (ISG15), processes known as deubiquitination and deISGylation. The overall coronavirus PLP deubiquitinase and deISGylase activities are not well characterized, especially among the different porcine coronaviruses. Ub is known to be almost completely conserved amongst eukaryotes; however, ISG15 is highly divergent with sequence identities as low as 35% among a broad range of animals. The implications of this sequence divergence on the ability of coronavirus PLPs to recognize and cleave certain species of ISG15 conjugates is poorly understood. In addition, the lack of coronavirus PLPs with altered deISGylase activity has been an obvious barrier in defining the roles

of deubiquitinase and deISGylase activities on pathogenesis and viral host evasion. This study aims to address these three major knowledge gaps to provide insight into the deubiquitination and deISGylation roles of the coronavirus PLPs. First, the biochemical characterization of the PLPs from PEDV and PDCoV are described in detail. Second, a biochemical and structural look into the coronavirus PLP interface with ISG15 utilizing the first X-ray structures of SARS-CoV in complex with the principle binding domain of human and mouse ISG15. Third, utilizing structural information, from the first X-ray structure of MERS-CoV in complex with the C-terminal domain of human ISG15, disruptive mutants were generated that lacked deISGylase activity but retained wild-type deubiquitinase activity. These studies provide insight into the varied deubiquitinase and deISGylase activity of the coronavirus PLP and provides important new molecular tools to engineer coronavirus PLPs to further advance the understanding of CoV pathogenesis.

INDEX WORDS: Coronavirus, Papain-like Protease, Ubiquitin, ISG15, Antiviral Innate Immunity

DEFINING DUB SPECIFICITY FOR THE CORONAVIRUS PAPAIN-LIKE PROTEASE

by

COURTNEY MARIE DACZKOWSKI

B.S., James Madison University, 2011

M.S., Georgia Southern University, 2014

A Dissertation Submitted to the Graduate Faculty of The University of Georgia in Partial Fulfillment of the Requirements for the Degree

DOCTOR OF PHILOSOPHY

ATHENS, GEORGIA

2018

DEFINING DUB SPECIFICITY FOR THE CORONAVIRUS PAPAIN-LIKE PROTEASE

by

COURTNEY MARIE DACZKOWSKI

Major Professor:	Scott Pegan
Committee:	Houjian Cai
	William Lanzilotta
	Zachary Wood

Electronic Version Approved:

Suzanne Barbour
Dean of the Graduate School
The University of Georgia
May 2018

DEDICATION

I would like to dedicate my dissertation to my family; this journey would have been near impossible to complete without your love and support. Dad, thank you for your endless love and continued support. I continue to look up to you every day and just knowing I can call you at any time for a pick-me-up or any type of advice is more than I could ever ask for. You are truly the best dad in the world. Mom, you are the strongest woman I know. I will always look up to you and I hope to one day be able to raise my children with the love and confidence that you continually exude. Thank you for always loving me and being there for me when I needed you most. To my wolf-pack: Allie, Tori, Andrew, and Brent you are the best siblings a girl could ever ask for. I love you four to pieces and being your big sister is an honor. I am proud of each and every one of you and I want to thank you for always making me laugh and knowing exactly what to say when I am feeling down. No matter where life takes us, I will always be here for you just like you are here for me. I love you all, thank you!

I also want to dedicate my dissertation to my other half and significant-other Nathan. I know over the last few years I have had my ups and downs, but you stuck with me and continued to love me no matter what. Thank you for your continued support and dedicating your time to proof-reading, science talk, and listening to me practice talks over and over again. I could not have made it to the end without you. I love you very much.

ACKNOWLEDGEMENTS

I would like to acknowledge my advisor Dr. Scott Pegan. I know that last four years have had some challenging moments, which might have included some tears and swear words, but I want to thank you for your mentorship and for believing in me. I appreciate everything you have done to help me get to this point and pushing me to become a better scientist. I would not change the last four years, I don't ever want to repeat them, but I would not change anything, and I just want to thank you. To my committee Dr. Cai, Dr. Wood, and Dr. Lanzilotta, thank you for your valuable input and continued push over the last four years. Your contributions to my scientific career are priceless.

I would also like to acknowledge my lab members past and present: John Dzimianski, Stephanie Bester, Brendan Freitas, Caroline Langley, and Dr. Octavia Goodwin. I know working with me can be tough sometimes but thank you for hanging in there and always being around if I ever needed help. I also want to say thank you to my two awesome undergrads, Brianna Beldon and Savannah Mace. You two are amazing and I want to thank you for your hard work. A special thank you to my lab member John; you are not only my colleague but truly a friend. I can't thank you enough for always being available to listen to me and bounce ideas around when it comes to science. I will never forget how much you have helped me, thank you. Octavia, I would not have made it if you did not join the lab. Thank you for being there for me, making me laugh, encouraging me to keep pushing forward, and being a shoulder to cry on when things got rough. I do not think I will ever be able to repay you for all you have done for me.

To Sudeepti Kuppa and Laura Wilt, the last four years have been quite the ride. I would not have made it through if it were not for you two. I cannot explain or put into words how much I appreciate all of the support you have given me. Whether it was advice on personal life craziness or helping me prepare for presentations and exams you were always there for me no matter what. Thank you so much for everything, I am not sure if I can stress enough how much I truly appreciate all you have done for me.

TABLE OF CONTENTS

Page

LIST OF TABLES

Page

LIST OF FIGURES

Page

CHAPTER 1

INTRODUCTION

The antiviral innate immune response

The innate immune system is often viewed as the first line of defense against viral infection and can be triggered in host cells upon infection with viruses, parasites, or bacteria. For viruses specifically, viral proteins and/or viral nucleic acids are sensed as foreign material and initiate the activation of the innate immune response (1). This response is comprised of several signaling pathways that ultimately involve the production of antiviral and proinflammatory molecules like interferons (IFNs), chemokines, and cytokines (2-4). Type-I interferons, IFN-α and IFN-β, further induce an antiviral state through the downstream activation of interferon stimulated genes (ISGs), which aid in limiting viral replication within host cells and the spread of virus to neighboring cells (1-5). Together all of these innate immune pathways are triggered and further regulated by post-translational modifications of host and viral proteins by phosphate, ubiquitin (Ub), and ubiquitin-like proteins, which effect activity, stability, and localization of host cellular immune factors (3, 6-9).

In more detail, the innate immune response is first initiated through the detection of pathogen-associated molecular patterns (PAMPs), to include double- or single-stranded RNA (dsRNA/ssRNA) or viral proteins that are detected through one of several pattern-recognition receptors (PRRs) (10-12). Two of the important PRRs include toll-like receptors (TLRs) and retinoic acid-inducible gene I (RIG-I)-like receptors (RLRs), which includes RIG-I and melanoma differentiation factor 5 (MDA5). TLRs, specifically TLR7, lead to the production of type-I IFNs,

IFN-α and IFN-β, and pro-inflammatory cytokines through the NK-κB pathway, via a signaling cascade directed through the adaptor protein MyD88 (myeloid differentiation primary response gene 88) (Figure 1.1) (10). MyD88 signals downstream through the recruitment of interleukin-1 receptor-associated kinase 4 (IRAK4) in order to activate IRAK1/2. The IRAK complex dissociates from MyD88 and activates TGF-β-activated kinase 1 (TAK1) through the binding to tumor necrosis factor (TNF) receptor-associated factor 6 (TRAF6). TAK1 then recruits TAK1-binding protein 1/2/3 (TAB1/2/3), activating the IKKα/β/γ complex (IKKγ is also referred to as NEMO), which is responsible for the phosphorylation event of IκB and release of NK-κB. NK-κB is translocated to the nucleus in order to induce the production of TNFα along with other pro-inflammatory cytokines. In addition, a complex is formed between TRAF6, IRAK4, TRAF3, IKKα, and IRAK1, which activates interferon regulatory factor 7 (IRF7) and the production of IFNs (10).

In comparison, RIG-I, once bound to ssRNA, is activated and further interacts with the mitochondrial antiviral signaling (MAVS) protein (also known as IPS-1), which aggregates on the outer membrane on the mitochondria (13-17). MAVS activates TRAF3, which induces the recruitment of the complex of TBK1 (TANK-binding kinase) and IKKε. This complex signals downstream for the phosphorylation of IRF3 and IRF7, which dimerizes and further leads to the induction of type-I IFNs and pro-inflammatory cytokines via NK-κB (1, 2, 9). An additional pathway that is known to induce type-I IFNs via IRF3 induction, is through cyclic-GM-P-AMP synthase (cGAS). cGAS stimulates the production of cGAMP, which then activates a protein on the endoplasmic reticulum, STING (stimulator of IFN genes). STING then follows the same pathway as RIG-I with the activation of TRAF3, the recruitment of the IKKε/TBK1 complex, downstream induction of IRF3 and IRF7, and subsequent expression of type-I IFNs (11, 12, 18).

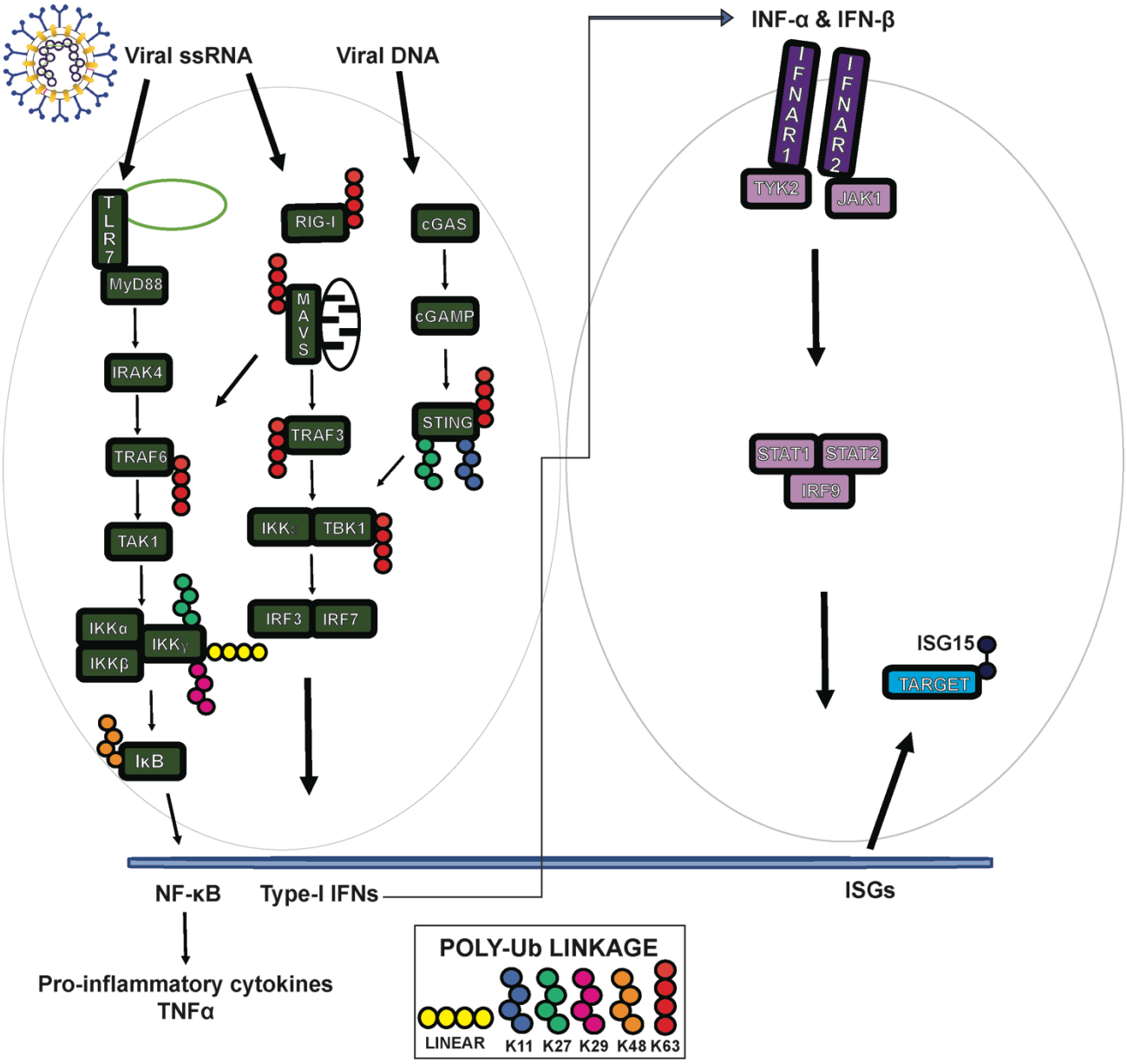

Figure 1.1. Antiviral innate immune response. Overview of the antiviral innate immune pathways and the post-translational modification by Ub and ISG15 involved in the response to viral RNA. Adapted from (1).

The expression of type-I IFNs leads to the production and secretion of IFN-α and IFN-β, which can then bind to the IFNAR1/2 (interferon alpha/beta receptor 1/2) on neighboring cells. This leads to the activation of the JAK-STAT pathway, which begins with the activation of tyrosine kinase 2 (TYK2) and Janus kinase 1 (JAK1) (10). Together these two enzymes phosphorylate both signal transducer and activator of transcription 1 and 2 (STAT1/2), which interact with IRF9 and IFN-stimulated gene factor 2 (ISG3). The STAT1/2 and IRF9 complex is translocated to the nucleus where it promotes the expression of interferon-stimulated genes (ISGs) (2, 19). One of the most important ISGs in the antiviral innate immune response is ISG15, which is known to interfere with viral replication and translation (5, 20-22).

The roles of ubiquitin and interferon stimulated gene product 15 in the antiviral innate immune response

The induction of the antiviral state by IFNs and ISGs not only rely on phosphorylation events described above, but also by post-translational modifications of host and viral proteins by Ub and ISG15. Ub is a small 76 amino acid single-domain protein, that adopts a β-grasp fold (a ubiquitin-like fold), and is almost completely conserved amongst all eukaryotes (23). Ub is conjugated to proteins, through a process known as ubiquitination, via a covalent attachment of Ub to available lysine residues on target proteins (3, 24-26). Ubiquitination occurs in three steps, activation, conjugation, and ligation, and involves three separate enzymes, ubiquitin-activating enzymes (E1), ubiquitin-conjugating enzymes (E2), and ubiquitin-protein ligases (E3) (3, 22). The activation step is ATP-dependent and involves the E1 forming a thioester linkage with the single Ub molecule. The second step involves the transfer of the Ub molecule to the E2's active site cysteine, which is then covalently attached, in the last step, via an isopeptide bond between the C-terminal glycine of Ub and the target protein's lysine residue executed by the E3 (25, 26).

In addition to being covalently bound to lysine residues of target proteins, Ub is also able to form poly-ubiquitin (poly-Ub) chains. This process occurs through the linking of 2 or more Ub molecules to itself at one of the seven different lysine residues, K6, K11, K27, K29, K33, K48, and K63 (3). These poly-Ub chains have been observed to be of all different lengths, contain different branching patterns, and can either be homogenous or heterogeneous with respect to the lysine linkage (Rape, 2016). A linear chain of poly-Ub can also occur and forms through the attachment of one Ub molecule to the receptor Ub's amino terminal methionine (M1) (27).

The most well studied poly-Ub linkages are K48 and K63, which are involved in the proteasomal degradation of proteins via the proteasome and signal transduction for protein and substrate stabilization respectively (3, 28, 29). The additional positions, also known as atypical positions, are not as well studied but have been implicated in several different cellular processes (30). K6 linked Ub has been observed to be involved in the DNA damage response while K11 linked Ub has been seen to play a role in TNF signaling, cell cycle regulation, and membrane trafficking (31-37). K27 poly-Ub has been observed to be involved in the mitochondrial damage response and development of regulatory T cells and K29- and K33-linkages are implicated in AMP-activated protein kinase (AMPL) regulation with K33-linkages also involved in T-cell receptor responses (38-42). Lastly, linear poly-Ub recently was shown to be required for downstream signaling by TNF and interleukin (IL)-1β and involved in the prevention of cell death induced by TNF (43, 44).

Polyubiquitination of several different enzymes within the innate immune system are observed to be key regulatory steps in the all of the complex pathways described above. In the TLR and RLR signaling pathways, K63-linked poly-Ub not only serves as a scaffold in the TRAF3 and TRAF6 complexes but induces activation and recruitment of the downstream signaling

complexes. K63 linked poly-Ub conjugated to TRAF3 activates the IKKε-TBK1 complex, which directly leads to IRF3 phosphorylation and subsequent production of type-I IFNs. K63 linked poly-Ub conjugated to TRAF6 leads to the recruitment of TAK and IKK-NEMO complex, which induces pro-inflammatory cytokines via the NK-κB pathway (8, 45, 46). K63-linkages are also important in the oligomerization and activation of RIG-I and aid in the binding of RIG-I to MAVS on the outer member of the mitochondria (8). K48-linked poly-Ub is most notably involved in signaling for IκB to be sent to the proteasome for degradation. This is a crucial step for downstream signaling to continue in the NK-κB pathway and the release of pro-inflammatory cytokines (47). Several atypical poly-Ub chains, K11, K27, and K29 along with linear polyUb, have been observed to be involved in the activation of NEMO and STING, which are important in the NK-κB pathway and type-I IFN production (48, 49).

Along the same lines as Ub, various other ubiquitin-like modifiers have been identified to be involved in some capacity within the innate immune response, with ISG15 being one of the most prominent (50, 51). ISG15 is an 8.5 kDa protein containing two Ub-like domains, which adopt a β-grasp fold similar to that of Ub even though sequence identity is low (51). Similar to ubiquitination, ISGylation is a three-step, three-enzyme process where ISG15 is conjugated to target proteins (52). The three-step process utilizes Ub-like enzymes, E1-like Ub-activating enzyme (UbEL1), Ub conjugating homolog 8 (UbcH8), and HECT domain-containing E3 ligase (HERC5) to conjugate the C-terminal glycine of ISG15 to host and viral proteins (53-57). This is made possible only after the removal of the last eight amino acids on the C-terminal end of ISG15, which exposes the glycine necessary for ISGylation to occur (52, 58). One major difference between Ub and ISG15 is ISG15 cannot make poly linkages and is only conjugated to proteins as a single modification.

Several contrasting reports have been recently published on ISG15's role within the antiviral immune response and whether it is directly involved in viral interference/inhibition and/or directly involved in the type-I interferon response itself (52). For several viruses studied, for example influenza virus, human immunodeficiency virus (HIV-1), and human papilloma virus (HPV), ISG15 has been shown to directly inhibit the virus to some degree (22, 59). Studies done on HIV-1 and avian sarcoma leucosis virus (ASLV) have shown that ISG15 can directly inhibit viral particle release and inhibit virus budding respectively (60-62). ISG15 has also been shown to shown to ISGylate host proteins after type-I interferons have been stimulated (22). Jak1 and STAT1 have been shown to be ISGylated along with IRF3, RIG-I, and protein kinase R (PKR), which are directly involved in the antiviral immune response and recognition of viral RNA (63-65). More specifically, ISG15 has been observed to stabilize IRF3; therefore, regulating the type-I IFN response in a positive manner (66, 67). Even though ISG15 has received a lot of attention recently in regard to its antiviral response, a clear picture on the role and mechanisms of ISG15 and whether viruses have clear countermeasures for ISGylation remains to be clarified. Possible discrepancies between studies can attributed to the type of virus and/or virus strain being used, the animal model, and the infection route (22).

Viral deubiquitinating (DUB) proteases

There are two major classes of viruses that encode proteases with the capability of suppressing the type-I IFN response by removing post translational modifications by Ub and ISG15. These viral-encoded deubiquitinating (DUBs) proteases are the viral ovarian tumor (vOTU) from the negative-sense, single-stranded RNA viruses from the genus *Nairovirus* and the papain-like protease (PLP) from the positive-sense, single-stranded RNA viruses from the family *Coronaviridae* (68-71). Unlike PLPs, a wealth of information about vOTUs from nairoviruses has

provided insight in to the different substrate specificity profiles present between the different species of viruses. It appears that substrate specificity is driven by the differences in the primary structure of the protease, which leads to vastly different substrate specificities and differences in ISG15 species accommodations (23, 68).

Using tools in the way of engineered vOTUs, the vOTU from Crimean-Congo hemorrhagic fever virus (CCHFV), demonstrated the role of vOTU's viral deubiquitination and deISGylation activities in the context of infection (72). The role of Ub was demonstrated to be directly involved in the antiviral innate immune response while the role of ISG15 was involved in later stages (72). However, the role of ISG15 species differences and the role of ISGylation of both host and viral proteins remains complex and not well understood. Specifically, differences in viral infections, the host species infected and the lack of mutations to delineate between deubiquitination and deISGylation have proven difficult in understanding ISG15s specific role. This lack of knowledge extends to the PLP with the overall DUB activity and the role of both ubiquitination and ISGylation in the context of viral infection and pathogenesis yet to be fully understood.

Coronaviruses (CoVs) and arteriviruses encode the PLP and are known to cause devastating diseases in a wide variety of species to include humans. Coronaviruses are positive-sense, single stranded RNA viruses with large genomes around 30 kb (73). These viruses have been shown to have a high frequency of RNA recombination within their large genomes, which gives rise to the ability for these viruses to adapt to new hosts through mutations (73). Coronaviruses can contain up to two PLPs, PLP1 and PLP2, with a single encoded protease being referred to as the PLpro (71, 74). Interestingly, at least one encoded viral PLP is a dual acting protease, containing the ability to act as a DUB and also is responsible for the essential function of proteolytic processing of the encoded polypeptide (71). This dual functionality of the PLP has

led to interest in the PLP to be a therapeutic target. However, many questions remain to be answered about the DUB activity of the PLP. Specifically, the overall substrate specificity across CoV PLPs and if species differences within ISG15 can play a role in the PLP's engagement with ISG15 is vastly unknown. In addition, the lack of molecular tools related to engineered PLPs with altered deubiquitination and deISGylation activity within the CoV PLP, has made studying pathogenicity and viral infection difficult. To provide insight into the CoV PLP, substrate specificity, the molecular drivers behind this specificity, and the influence of ISG15 species-species differences was sought. The following studies outline the development of new molecular tools in order to open the possibility for the development of reverse genetic systems to further study the CoV PLPs function in terms of viral processes and pathogenesis.

CHAPTER 2

BIOCHEMICAL CHARACTERIZATION OF THE PAPAIN-LIKE PROTEASE FROM TWO PORCINE CORONAVIRUSES, PORCINE EPIDEMIC DIARRHEA VIRUS AND PORCINE DELTACORONAVIRUS

Daczkowski, C.M., S.L. Mace, K. Faaberg, and S.D. Pegan.

To be submitted to [Virology]

Introduction

Porcine epidemic diarrhea virus (PEDV) and porcine deltacoronavirus (PDCoV) are two devastating deleterious porcine viruses that are currently threatening the safety and economics of the United States pork industry. It was estimated that the total economic impact for the US alone could range from an astonishing $900 million to $1.8 billion (1, 2). Cases of PEDV were first confirmed in North American swine in April of 2013 and within just 14 months had spread to 30 different states affecting almost 50% of swine herds (3-5). Compounding the devastation, PEDV has an astounding mortality rate close to 100% in neonatal pigs (3). PDCoV was first clinically diagnosed in February 2014 in Ohio and by March had quickly spread to six other states (6). In comparison, PDCoV has been observed to have a lesser mortality rate compared to PEDV, at approximately 40%, but has indistinguishable clinical symptoms of vomiting, severe diarrhea, and dehydration, to PEDV and a related virus transmissible gastroenteritis virus (TGEV) (7). The US PEDV and PDCoV strains show an approximate 99% sequence identity to the Chinese strains, which currently are causing severe outbreaks in porcine populations throughout China (7-11). These strains are thought to be the origin for the US strain; however, the exact mode of introduction to the US is still unknown (12, 13).

PEDV and PDCoV are both enveloped, single-stranded, positive sense RNA coronaviruses (CoVs) found in the order *Nidovirales*, family *Coronaviridae*, and subfamily *Coronavirinae*. Recently, the traditional 3 group taxonomy of CoVs was replaced with 4 genera, *Alphacoronavirus, Betacoronavirus, Gammacoronavirus* and the newest genus *Deltacoronavirus*, with PEDV and PDCoV falling into the *Alpha-* and *Deltacoronavirus* genera respectively (14). CoVs are known to infect a wide variety of species including mammals and birds with viruses from the *Alpha-*, *Beta-*, and *Deltacoronavirus* genera readily infecting porcine. The genome of

PEDV is 28 kb long while the PDCoV genome is considerably smaller at 25.4 kb; however, both share a similar overall genome organization (14). Like other positive single-stranded RNA viruses, both of these viruses encode two cysteine proteases, the papain-like protease (PLP) and the 3C-like protease or main protease (3CLpro; M^{pro}). In the case of PEDV as well as several other members of *Alpha-* and *Betacoronavirus*, two copies of the PLP are encoded and denoted as PLP1 and PLP2. A single PLP is encoded in the PDCoV genome, the PLpro, and is a homolog to the PEDV PLP2 (14). Together, these proteases are responsible for the proteolytic processing of the long polyprotein into the respective 16 different nonstructural proteins (nsps), which are essential for the formation of the membrane-bound replicase complex utilized during RNA replication (15-19). The PLP is responsible for cleaving nsps 1-3 while the 3C-like protease cleaves 4-16; however, the CoV PLP has been observed to play additional roles other than promoting viral replication (16, 20).

Several CoV PLPs, such as the PLpro from severe acute respiratory syndrome coronavirus (SARS-CoV), Middle East respiratory syndrome coronavirus (MERS-CoV), avian infectious bronchitis virus (IBV) and the PLP2 from mouse hepatitis virus (MHV), have been suggested to down regulate the innate immune system by cleaving post-translational modifications of host proteins by ubiquitin (Ub) and Ub-like interferon stimulated gene product 15 (ISG15) (Figure 2.1) (17, 21, 22). The processes of ubiquitination and ISGylation of viral and host proteins are essential for several pathways within the innate immune system, which is thought of as the first line of defense against viral infections (23, 24). More specifically, this includes the induction of interferons (IFNs), within the type I interferon response (IFN-I), interferon stimulated genes (ISGs) and cytokines as well as an inflammatory response through the NFκB pathway (25, 26). The combined activities of deubiquitination and deISGylation by the PLP have been observed to

antagonize the IFN-I response suggesting the PLP to be a virulence factor that can be manipulated for therapeutic purposes. This has been demonstrated through the disruption of deubiquitinating and deISGylating activities from the MERS-CoV PLpro, which subsequently resulted in the partial suppression of Ub-dependent mitochondrial antiviral-signaling protein (MAVS) mediated signaling leading to removal of the antagonized IFN-I response (27). In addition, destabilizing mutations within the MHV PLP2, which diminished both activities, resulted in a reversal of the antagonism of IFN-I response (18). Taken together, these results demonstrate the need to further understand the PLPs from reemerging coronaviruses, especially CoVs infecting swine like PEDV and PDCoV, to better understand this key viral evasion mechanism and associated pathogenicity.

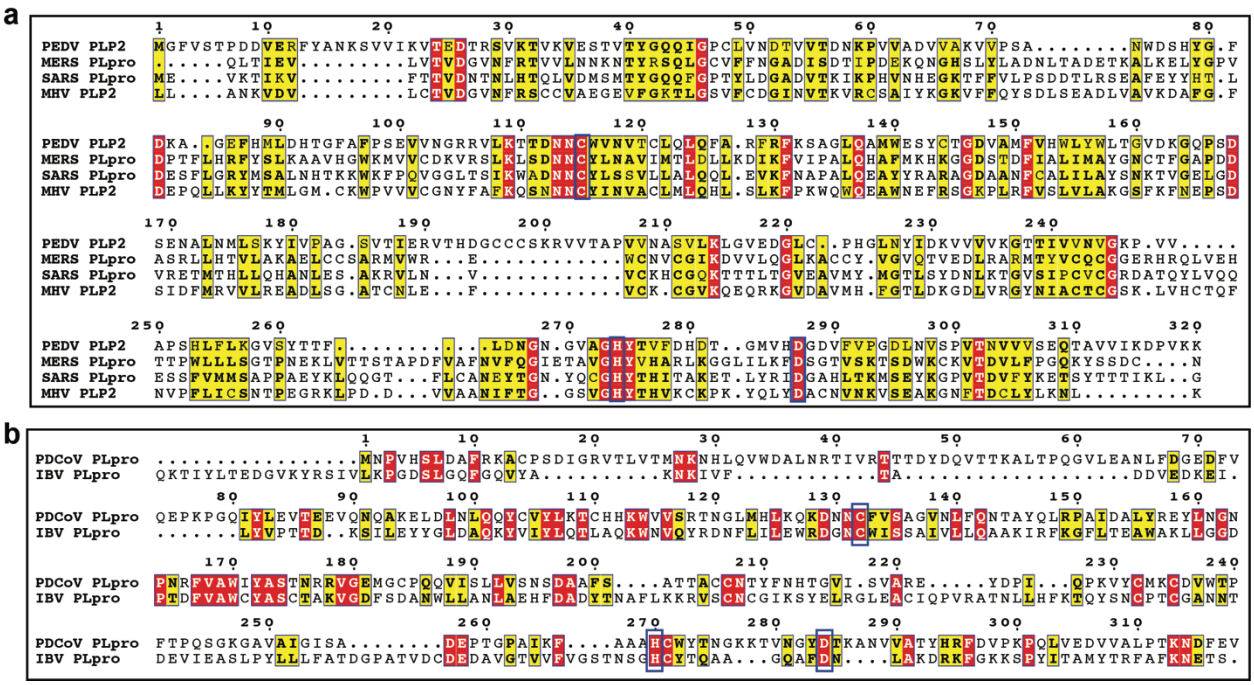

Figure 2.1. Sequence alignment of PLpros and PLP2s from coronaviruses. (a/b) The PLpro or PLP2 from PEDV (accession number APG77337.1), MERS-CoV (accession number AFS88944), SARS-CoV (accession number P0C6U8), PDCoV (accession number ANI85845), and IBV (accession number AKP63382). Residues from the catalytic triad are boxed in blue.

The biochemically characterized CoV PLPs, have been observed to possess varying degrees of deubiquitinase and deISGylase activities. Ubiquitination, and subsequent deubiquitinase activity, is not limited to a single mono-Ub event but includes polyubiquitination at one of the seven available lysine positions on Ub (positions 6, 11, 27, 29, 33, 48, and 63) (28, 29). Both mono- and polyubiquitination of viral and host proteins are essential in several different signaling pathways. For example, K63-linked poly-Ub has been observed to be directly involved in the activation of retinoic acid-inducible gene I and mitochondrial antiviral signaling protein, which is a critical innate immune pathway in recognizing foreign single-stranded RNA (ssRNA) (30, 31). Also, K48-linked poly-Ub has been observed to be involved in triggering the degradation of IκB in the NFκB pathway and K11-linked poly-Ub has recently been implicated in TNF signaling (32-36). However, the exact role of deubiquitination activities in promoting CoV PLPs as antagonists of the IFN pathway is still unknown. In addition, Ub has been shown to be conserved almost completely amongst eukaryotes while the sequence identity of ISG15s can be as low as 35% amongst a broad range of animals (37). Species-species variances in ISG15 have been shown to impact the ability of a similar viral protease class, the nairovirus viral ovarian tumor domain protease (vOTU), to engage and process different ISG15s effectively. Data on the nairovirus vOTU show evidence for the direct correlation of species ISG15 a protease can engage and the ability for the virus to infect that given species. This could potentially begin to explain the zoonotic potential of CoVs and the ability to infect a wide variety of species.

Regrettably, the PLP2 from PEDV and the PLpro from PDCoV have not been biochemically characterized with respect to specific deubiquitinating and deISGylating activities. Work on the PEDV PLP2 in cells has demonstrated that the PEDV PLP2 is directly involved in the antagonism of the IFN response and can cleave poly-Ub chains from RIG-I and stimulator of

interferon genes (STING); however, the exact catalytic activity and substrate preference has yet to be reported (38). Here the biochemical characterization of the PLPs from PEDV and PDCoV are described in detail. Utilizing purified PLP from both PEDV and PDCoV in *in vitro* assays, has allowed for the removal of hurdles due to additional cellular pathways that can complicate data interpretation, and allowed for the use of simplified kinetics. Interestingly, these data report the possibility for a CoV PLP to heavily prefer one substrate over the other and that the preference for ISG15 from different species might not be as broad as previously anticipated.

Results and Discussion

Biochemical characterization of substrate preference

In order to investigate the different substrate preferences for the PLPs from PEDV and PDCoV, biochemical information on the specific deubiquitinating and deISGylating activities was evaluated. Enzymatic activity was assessed utilizing an amino-4-methylcourmain (AMC) fluorophore conjugated to the C-terminal end of Ub, human ISG15, and a short peptide sequence, RLRGG, which is the shared recognition sequences of the two prior substrates. The peptide is used as a control in order to examine overall catalytic efficiency of the two proteases. Deubiquitinating and deISGylating substrate preference was determined by monitoring the release of the fluorophore over time. Intriguingly, the PLP2 originating from PEDV and the PLpro originating from PDCoV had vastly different deubiquitinating and deISGylase activity (Figure 2.2). PEDV PLP2 seems to be solely a deubiquitinase cleaving Ub-AMC conjugates at 0.29 ± 1.4E-3 molecules/min, which is three orders of magnitude above what was seen for the deISGylase activity at 3.2E-4 ± 3.9E-5 molecules/min (Figure 2.2a). This is in contrast to PDCoV PLpro, which has significantly higher deISGylase activity at 4.6E-2 ± 2.2E-3 molecules/min compared to its deubiquitinase at 4.8E-3 ± 4.0E-4 molecules/min (Figure 2.2b). Even though the substrate

profiles for the two proteases differ, the overall peptide activity is similar for the PEDV PLP2 and PDCoV PLpro, 1.0E-2 ± 5.6E-5 and 2.3E-2 ± 1.8E-5 molecules/min respectively (Figure 2.2).

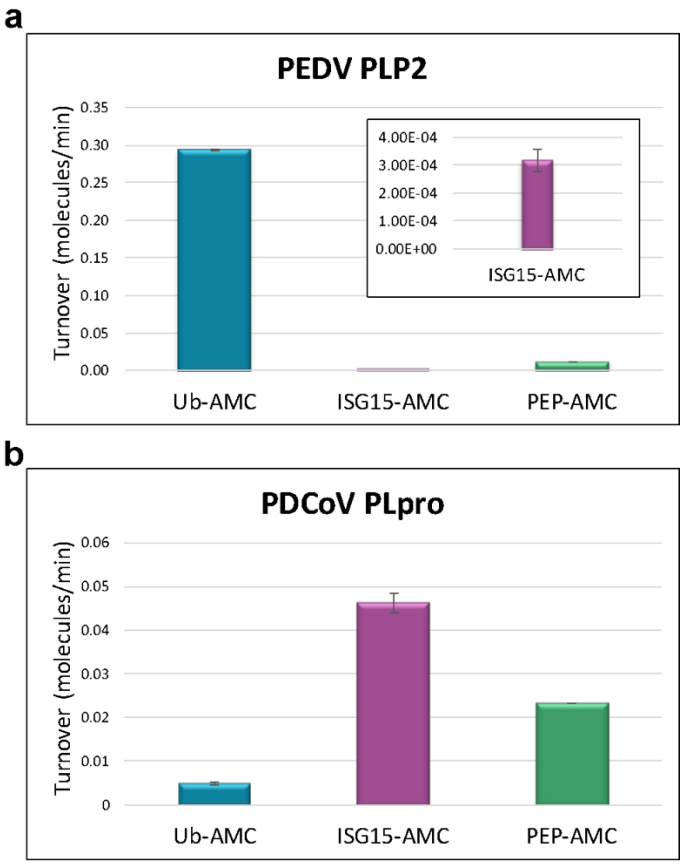

Figure 2.2. Enzymatic activity of the PEDV PLP2 and PDCoV PLpro. (a/b) Protease activity of the PEDV PLP2 and PDCoV PLpro assessed utilizing 1 μM Ub- and ISG15-AMC and 50 μM RLRGG-AMC. Readout is measured via an increase in fluorescence over time and is reported as turnover (molecules/min).

Di-ubiquitin specificity

In some cases, it is possible for DUBs to have higher turnover rates for poly-Ub linkages compared to mono-Ub potentially due to an increase in favorable contacts between the larger Ub substrate (39). Even though the PLpro from PDCoV had little to no Ub-AMC activity, it is possible that both the PEDV PLP2 and PDCoV PLpro have similar poly-Ub activity. To investigate this further both PLPs were tested against a panel of the seven lysine linked di-Ub (K6, K11, K27,

K29, K33, K48, and K63) and linear di-Ub (Figure 2.3a). In the past, PLPs have been observed to prefer K48-linked poly-Ub linkages (40). For the PEDV PLP2 significant activity towards K48-linked di-Ub was observed, which is similar to the activity observed for SARS-CoV PLpro. Intriguingly, significant activity was also observed for K63-, K11-, and K6-linked di-Ub. The PDCoV PLpro was also observed to have minor activity towards K63- and K48-linked di-Ub and very little activity towards K6-, K11-, and K27-linked di-Ub; however, this activity was only observed when the PDCoV PLpro was increased 10 times the amount compared its porcine counterpart.

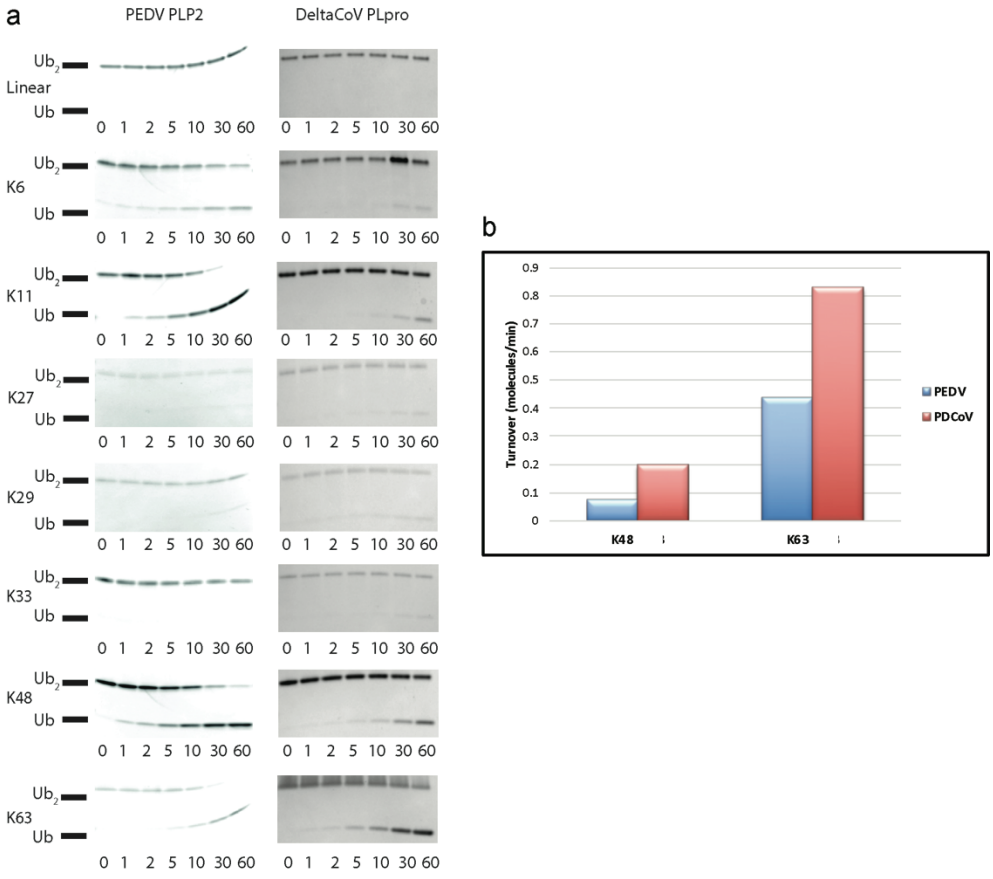

Figure 2.3. PLP preference for poly-Ub linkage substrates. (a) Di-Ub linkages (10 μM) were incubated with PEDV PLP2 (200 nM) and PDCoV PLpro (2 μM) at 37 °C for 60 min. Seven time points were taken and analyzed on a 10% Mini-Protean Tris-Tricine precast gel (Bio-Rad). (b) Cleavage activity for K48- and K63-linked di-Ub FRET substrates at 1 μM. Turnover (molecules/min) was evaluated based on the increase of fluorescence over time.

To take a more quantitative approach to assess di-Ub activity, K48- and K63-linked di-Ub fluorescence resonance energy transfer (FRET) substrates were used (Figure 2.3b). The activity toward each FRET substrate was monitored by an increase in fluorescence via the proteases ability to cleave the di-Ub molecule, which separates the FRET pairing. For both the PEDV PLP2 and PDCoV PLpro the di-Ub panel results mirrored that of the di-Ub FRET cleavage assay results (Figure 2.3b). However, the overall di-Ub FRET activity for PEDV PLP2 was low for the K48- and K63-linkages compared to what was seen with the cleavage assay, likely suggesting the FRET pair positioning interfered with the protease's interaction with the substrates. This provides a potential link to the antiviral innate immune response pathways these PLPs could be involved in suppressing, especially with K11-, K48- and K63-linked poly-Ub being heavily implicated in these immune regulatory pathways. Specifically, K48-linked poly-Ub is responsible for activation of the inflammatory response through the NF-κB pathway via proteasomal degradation of inhibitor of nuclear factor κB (IκB). K63-linked poly-Ub has been directly linked to antiviral signaling by RIG-I/MAVS, which induces type-I IFNs. Lastly, K11-linked poly-Ub has been recently shown to be involved in the ubiquitination of STING and TNF signaling, which induces pro-inflammatory cytokines in response to a viral infection. Taken together, the ability of the PEDV PLP2 to process several different Ub-linkages might suggest a link to the increased pathogenicity of PEDV compared to that of PDCoV.

Species-species ISG15 activity

Ub has been observed to be almost completely conserved amongst eukaryotes while ISG15 sequence identity can vary as low as 35% amongst a broad range of species (37). Currently, there is a knowledge gap as to whether or not these species sequence variations within ISG15 could play a role in the susceptibility to cleavage by CoV PLPs. Recently, an assay was developed to test the

deISGylase activity of nairovirus vOTUs where the cleavage from pro-ISG15 into mature ISG15, by the vOTU, was monitored over time (37). The nairovirus vOTUs were shown to cleave species ISG15 they readily infect or are known species that were known reservoirs of the virus; however, they were able to cleave other species they do not infect as well. Utilizing the same assay, the PLpro from PDCoV was tested against eight different species of ISG15 including porcine, human, sheep, mouse, northern tree shrew, fish, camel, and bat (Figure 2.4). Intriguingly, the PDCoV PLpro was only able to cleave porcineISG15 (pISG15). Interestingly, the subfamily of *Deltacoronavirus* is said to have emerged from a bird host but birds do not have an ISG15 homolog. The fact that the PDCoV PLpro has significant deISGylase activity, compared to its PEDV PLP2 counterpart, and is only able to cleave pISG15 in the 60 min time frame, suggests an evolutionary push to adapt and overcome the immune system within the porcine host. This also suggests that the deISGylase activity seen with the hISG15-AMC assay could be higher if a porcine ISG15 was conjugated to the AMC fluorophore.

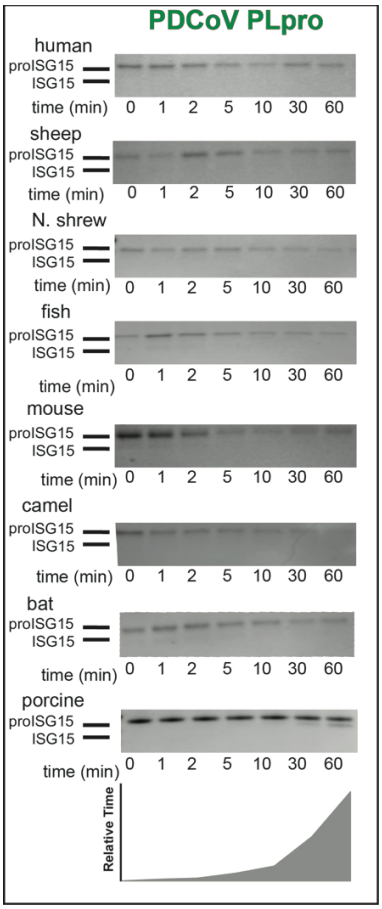

Figure 2.4. ProISG15 cleavage assay for PDCoV PLpro. Cleavage profiles for PDCoV PLpro with proISG15s from human, sheep, northern tree shrew, jackknife fish, mouse, dromedary camel, vesper bat, and porcine. Reactions were conducted at 37 °C for 60 min with 10 μM of each proISG15 and 500 nM PDCoV PLpro. Seven time points were taken and analyzed on a 10% Mini-Protean Tris-Tricine precast gel (Bio-Rad).

References

1. Schulz LL, Tonsor GT. 2015. Assessment of the economic impacts of porcine epidemic diarrhea virus in the United States. J Anim Sci 93:5111-8.

2. Paarlberg PL. 2014. Updates estimated economic welfare impacts of porcine epidemic diarrhea virus (PEDV). Purdue University, Deptartment of Agricultural Economic.

3. Stevenson GW, Hoang H, Schwartz KJ, Burrough ER, Sun D, Madson D, Cooper VL, Pillatzki A, Gauger P, Schmitt BJ, Koster LG, Killian ML, Yoon KJ. 2013. Emergence of Porcine

epidemic diarrhea virus in the United States: clinical signs, lesions, and viral genomic sequences. J Vet Diagn Invest 25:649-54.

4. Goede D, Murtaugh MP, Nerem J, Yeske P, Rossow K, Morrison R. 2015. Previous infection of sows with a "mild" strain of porcine epidemic diarrhea virus confers protection against infection with a "severe" strain. Vet Microbiol 176:161-4.

5. Goede D, Morrison RB. 2016. Production impact & time to stability in sow herds infected with porcine epidemic diarrhea virus (PEDV). Prev Vet Med 123:202-207.

6. USDA. 2014. Swine Enteric Coronavirus Disease Testing Summary Report. (https://www.aphis.usda.gov/animal_health/animal_dis_spec/swine/downloads/secd_sit_rep_11_14_14.pdf. Accessed

7. Wang L, Byrum B, Zhang Y. 2014. Detection and genetic characterization of deltacoronavirus in pigs, Ohio, USA, 2014. Emerg Infect Dis 20:1227-30.

8. Chen Q, Li G, Stasko J, Thomas JT, Stensland WR, Pillatzki AE, Gauger PC, Schwartz KJ, Madson D, Yoon KJ, Stevenson GW, Burrough ER, Harmon KM, Main RG, Zhang J. 2014. Isolation and characterization of porcine epidemic diarrhea viruses associated with the 2013 disease outbreak among swine in the United States. J Clin Microbiol 52:234-43.

9. Huang YW, Dickerman AW, Pineyro P, Li L, Fang L, Kiehne R, Opriessnig T, Meng XJ. 2013. Origin, evolution, and genotyping of emergent porcine epidemic diarrhea virus strains in the United States. MBio 4:e00737-13.

10. Marthaler D, Jiang Y, Collins J, Rossow K. 2014. Complete Genome Sequence of Strain SDCV/USA/Illinois121/2014, a Porcine Deltacoronavirus from the United States. Genome Announc 2.

11. Lee S, Lee C. 2014. Complete Genome Characterization of Korean Porcine Deltacoronavirus Strain KOR/KNU14-04/2014. Genome Announc 2.

12. Bowman AS, Krogwold RA, Price T, Davis M, Moeller SJ. 2015. Investigating the introduction of porcine epidemic diarrhea virus into an Ohio swine operation. BMC Vet Res 11:38.

13. Pasick J, Berhane Y, Ojkic D, Maxie G, Embury-Hyatt C, Swekla K, Handel K, Fairles J, Alexandersen S. 2014. Investigation into the role of potentially contaminated feed as a source of the first-detected outbreaks of porcine epidemic diarrhea in Canada. Transbound Emerg Dis 61:397-410.

14. Woo PCY, Lau SKP, Lam CSF, Lau CCY, Tsang AKL, Lau JHN, Bai R, Teng JLL, Tsang CCC, Wang M, Zheng B-J, Chan K-H, Yuen K-Y. 2012. Discovery of Seven Novel Mammalian and Avian Coronaviruses in the Genus Deltacoronavirus Supports Bat Coronaviruses as the Gene Source of Alphacoronavirus and Betacoronavirus and Avian Coronaviruses as the Gene Source of Gammacoronavirus and Deltacoronavirus. Journal of Virology 86:3995-4008.

15. Thiel V, Ivanov KA, Putics Á, Hertzig T, Schelle B, Bayer S, Weißbrich B, Snijder EJ, Rabenau H, Doerr HW, Gorbalenya AE, Ziebuhr J. 2003. Mechanisms and enzymes involved in SARS coronavirus genome expression. Journal of General Virology 84:2305-2315.

16. Barretto N, Jukneliene D, Ratia K, Chen Z, Mesecar AD, Baker SC. 2005. The papain-like protease of severe acute respiratory syndrome coronavirus has deubiquitinating activity. J Virol 79:15189-98.

17. Ratia K, Saikatendu KS, Santarsiero BD, Barretto N, Baker SC, Stevens RC, Mesecar AD. 2006. Severe acute respiratory syndrome coronavirus papain-like protease: Structure of a viral deubiquitinating enzyme. Proceedings of the National Academy of Sciences 103:5717-5722.

18. Mielech AM, Deng X, Chen Y, Kindler E, Wheeler DL, Mesecar AD, Thiel V, Perlman S, Baker SC. 2015. Murine Coronavirus Ubiquitin-Like Domain Is Important for Papain-Like Protease Stability and Viral Pathogenesis. Journal of Virology 89:4907-4917.

19. Harcourt BH, Jukneliene D, Kanjanahaluethai A, Bechill J, Severson KM, Smith CM, Rota PA, Baker SC. 2004. Identification of Severe Acute Respiratory Syndrome Coronavirus Replicase Products and Characterization of Papain-Like Protease Activity. Journal of Virology 78:13600-13612.

20. Ratia K, Kilianski A, Baez-Santos YM, Baker SC, Mesecar A. 2014. Structural Basis for the Ubiquitin-Linkage Specificity and deISGylating Activity of SARS-CoV Papain-Like Protease. PLoS Pathog 10:e1004113.

21. Lindner HA, Lytvyn V, Qi H, Lachance P, Ziomek E, Ménard R. 2007. Selectivity in ISG15 and ubiquitin recognition by the SARS coronavirus papain-like protease. Archives of Biochemistry and Biophysics 466:8-14.

22. Kong L, Shaw N, Yan L, Lou Z, Rao Z. 2015. Structural View and Substrate Specificity of Papain-like Protease from Avian Infectious Bronchitis Virus. The Journal of Biological Chemistry 290:7160-7168.

23. Davis ME, Gack MU. 2015. Ubiquitination in the antiviral immune response. Virology 479-480:52-65.

24. Sadler AJ, Williams BR. 2008. Interferon-inducible antiviral effectors. Nat Rev Immunol 8:559-68.

25. Frieman M, Ratia K, Johnston RE, Mesecar AD, Baric RS. 2009. Severe acute respiratory syndrome coronavirus papain-like protease ubiquitin-like domain and catalytic domain regulate antagonism of IRF3 and NF-kappaB signaling. J Virol 83:6689-705.

26. Devaraj SG, Wang N, Chen Z, Chen Z, Tseng M, Barretto N, Lin R, Peters CJ, Tseng C-TK, Baker SC, Li K. 2007. Regulation of IRF-3-dependent Innate Immunity by the Papain-like Protease Domain of the Severe Acute Respiratory Syndrome Coronavirus. Journal of Biological Chemistry 282:32208-32221.

27. Bailey-Elkin BA, Knaap RC, Johnson GG, Dalebout TJ, Ninaber DK, van Kasteren PB, Bredenbeek PJ, Snijder EJ, Kikkert M, Mark BL. 2014. Crystal structure of the Middle East respiratory syndrome coronavirus (MERS-CoV) papain-like protease bound to ubiquitin facilitates targeted disruption of deubiquitinating activity to demonstrate its role in innate immune suppression. J Biol Chem 289:34667-82.

28. Komander D, Clague MJ, Urbe S. 2009. Breaking the chains: structure and function of the deubiquitinases. Nat Rev Mol Cell Biol 10:550-63.

29. Kulathu Y, Komander D. 2012. Atypical ubiquitylation - the unexplored world of polyubiquitin beyond Lys48 and Lys63 linkages. Nat Rev Mol Cell Biol 13:508-23.

30. Faaberg KS, Han J, Wang Y. 2006. Molecular dissection of porcine reproductive and respiratory virus putative nonstructural protein 2. Adv Exp Med Biol 581:73-7.

31. Zeng W, Sun L, Jiang X, Chen X, Hou F, Adhikari A, Xu M, Chen ZJ. 2010. Reconstitution of the RIG-I pathway reveals a signaling role of unanchored polyubiquitin chains in innate immunity. Cell 141:315-30.

32. Alkalay I, Yaron A, Hatzubai A, Orian A, Ciechanover A, Ben-Neriah Y. 1995. Stimulation-dependent I kappa B alpha phosphorylation marks the NF-kappa B inhibitor for degradation via the ubiquitin-proteasome pathway. Proc Natl Acad Sci U S A 92:10599-603.

33. Chen Z, Hagler J, Palombella VJ, Melandri F, Scherer D, Ballard D, Maniatis T. 1995. Signal-induced site-specific phosphorylation targets I kappa B alpha to the ubiquitin-proteasome pathway. Genes Dev 9:1586-97.

34. Castaneda CA, Kashyap TR, Nakasone MA, Krueger S, Fushman D. 2013. Unique structural, dynamical, and functional properties of k11-linked polyubiquitin chains. Structure 21:1168-81.

35. Dynek JN, Goncharov T, Dueber EC, Fedorova AV, Izrael-Tomasevic A, Phu L, Helgason E, Fairbrother WJ, Deshayes K, Kirkpatrick DS, Vucic D. 2010. c-IAP1 and UbcH5 promote K11-linked polyubiquitination of RIP1 in TNF signalling. EMBO J 29:4198-209.

36. Wang D, Fan J, Fang L, Luo R, Ouyang H, Ouyang C, Zhang H, Chen H, Li K, Xiao S. 2015. The nonstructural protein 11 of porcine reproductive and respiratory syndrome virus inhibits NF-kappaB signaling by means of its deubiquitinating activity. Mol Immunol 68:357-66.

37. Deaton MK, Dzimianski JV, Daczkowski CM, Whitney GK, Mank NJ, Parham MM, Bergeron E, Pegan SD. 2016. Biochemical and Structural Insights into the Preference of Nairoviral

DeISGylases for Interferon-Stimulated Gene Product 15 Originating from Certain Species. Journal of Virology 90:8314-8327.

38. Xing Y, Chen J, Tu J, Zhang B, Chen X, Shi H, Baker SC, Feng L, Chen Z. 2013. The papain-like protease of porcine epidemic diarrhea virus negatively regulates type I interferon pathway by acting as a viral deubiquitinase. Journal of General Virology 94:1554-1567.

39. Capodagli GC, Deaton MK, Baker EA, Lumpkin RJ, Pegan SD. 2013. Diversity of Ubiquitin and ISG15 Specificity among Nairoviruses' Viral Ovarian Tumor Domain Proteases. Journal of Virology 87:3815-3827 %! Diversity of Ubiquitin and ISG15 Specificity among Nairoviruses' Viral Ovarian Tumor Domain Proteases.

40. Ratia K. 2008. Structure, function, and inhibition of the papain-like protease from SARS coronavirus. . Doctor of Philosophy University of Illinois at Chicago.

CHAPTER 3

STRUCTURAL INSIGHTS INTO THE INTERACTION OF CORONAVIRUS PAPAIN-LIKE PROTEASES AND INTERFERON-STIMULATED GENE PRODUCT 15 FROM DIFFERENT SPECIES[1]

[1]Daczkowski, C.M., J.V. Dzimianski, J.R. Clasman, O. Goodwin, A.D. Mesecar, and S.D. Pegan. 2017. *Journal of Molecular Biology*. 429(11): 1661-1683.

Reprinted here with permission of publisher

Abstract

Severe Acute and Middle East Respiratory syndrome coronaviruses (SARS-CoV and MERS-CoV) encode multifunctional papain-like proteases (PLPs) that have the ability to process the viral polyprotein to facilitate RNA replication as well as antagonize the host innate-immune response. The latter function involves reversing post-translational modification of cellular proteins conjugated with either ubiquitin (Ub) or Ub-like interferon stimulated gene product 15 (ISG15). Ubiquitin is known to be highly conserved among eukaryotes but surprisingly ISG15 is highly divergent among animals. The ramifications of this sequence divergence to recognition of ISG15 by coronaviral papain-like protease at the structural and biochemical levels are poorly understood. Therefore, the activity of PLPs from SARS-CoV, MERS-CoV and mouse hepatitis virus (MHV) was evaluated against seven ISG15s originating from an assortment of animal species susceptible, and not, to certain coronavirus infections. Excitingly, our kinetic, thermodynamic and structural analysis revealed an array of different preferences among PLPs. Included in these studies is the first insight into a coronoavirus PLP's interface with ISG15 via SARS-CoV PLP in complex with the principle binding domain of human and mouse ISG15s. The first X-ray structure of the full-length mouse ISG15 protein is also reported and highlights a unique, twisted-hinge region of ISG15 that is not conserved in human ISG15 suggesting a potential role in differential recognition. Taken together, this new information provides a structural and biochemical understanding of the distinct specificities amongst coronavirus PLPs observed and addresses a critical gap of how PLPs can interact with ISG15s from a wide variety of species.

Introduction

Coronaviruses (CoVs) are enveloped, positive-stranded RNA viruses that cause mild to severe infections in a wide range of mammals and birds. Specifically, severe acute and Middle East respiratory syndrome coronaviruses (SARS-CoV; MERS-CoV) are well-recognized viral pathogens that have emerged from different animal reservoirs to cause deadly disease in humans. SARS-CoV first emerged in 2002 with a case fatality rate of 10%, claiming the lives of over 800 people and infecting more than 8000 [1; 2]. Ten years later, MERS-CoV emerged with a shocking case fatality rate near 35% and has spread to 27 different countries to date [3]. The continuing threat of MERS-CoV was recently underscored by one of its most recent outbreaks in Republic of Korea. This outbreak quickly led to 36 deaths, which has brought the total MERS-CoV global deaths to over 600 [4; 5].

Similar to other positive stranded RNA viruses, CoVs encode two types of cysteine proteases, including the papain-like protease (PLP) and 3C-like protease, also known as the main protease. Together, these enzymes cleave the viral polyprotein into 16 different nonstructural proteins (Nsps 1-16) in order to generate the membrane-bound replicase complex for RNA replication [6; 7; 8; 9]. CoVs encode either a single PLP, termed PLpro, or two PLPs that process a total of three cleavage sites within the polyprotein [7; 10]. For instance, SARS-CoV and MERS-CoV encode a single PLpro, while other CoVs such as mouse hepatitis virus (MHV) encode for both the papain-like protease 1 (PLP1) and papain-like protease 2 (PLP2) (Figure 3.1a).

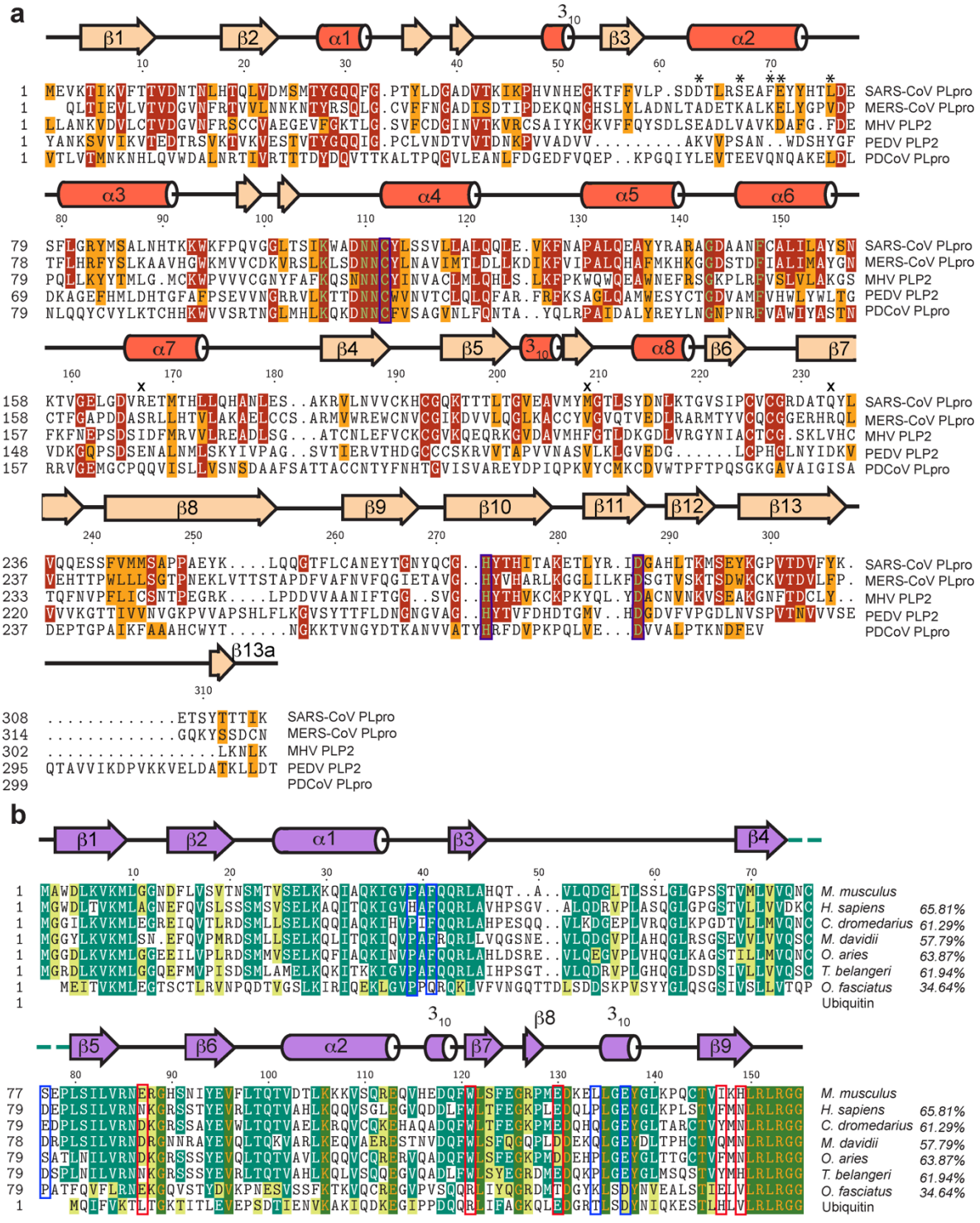

Figure 3.1 (a) The PLPs from SARS CoV (Accession number P0C6U8), MERS CoV (Accession number AFS88944.1), MHV (Accession number P0C6V0), PEDV (Accession number AKP80587.1), and Porcine deltacoronavirus (PDCoV) (Accession number AHM88399.1). The sequence numbering ruler is based on the SARS-CoV PLpro sequence. Residues forming the catalytic triad are boxed in purple. The secondary structure of SARS-CoV PLpro based on DSSP

is denoted, with α- and 3_{10}-helices in reddish orange and β-sheets in wheat. Residues forming the "ridge" of SARS-CoV PLpro are marked with an asterisk (*). Residues of SARS-CoV PLpro mutated in this study are denoted ("x"). (b) Sequence alignment of ISG15s from mouse (*Mus musculus*; Accession: AAB02697.1), human (*Homo sapiens*; Accession: AAH09507.1), dromedary camel *Camelus dromedarius*; Accession: XP_010997700.1), vesper bat (*Myotis davidii*; Accession: ELK23605.1), sheep (*Ovis aries;* Accession: AF152103.1), northern tree shrew (*Tupaia belangeri*; Accession: AFH66859.1), and jackknife fish (*Oplegnathus fasciatus*; Accession: BAJ16365.1) along with ubiquitin. The sequence numbering ruler is based on mouse ISG15. Secondary structure of mouse ISG15 based on DSSP is denoted in purple. The hinge region between β4 and β5 is denoted using a dashed line in teal. Percentages indicate sequence identity relative to mouse ISG15. Residue positions identified in this study that form key interactions with SARS-CoV PLpro are boxed in red. Residue positions implicated in driving the specific tertiary fold features of mouse and human ISG15 are boxed in blue.

Beyond cleaving the viral polyprotein, PLPs have additional activities that promote virus replication. The X-ray structure of the first CoV PLP determined from SARS revealed that these enzymes resemble the structure of human ubiquitin-specific proteases (USPs) and are thereby known as viral USPs, often acting as deubiquitinating enzymes with the ability to remove the post-translational modification ubiquitin (Ub) from target proteins [8]. Some PLPs are also deISGylating enzymes with the ability to reverse the post-translational modification of the Ub-like protein interferon stimulated gene product 15 (ISG15) from cellular proteins [11]. Such activities were implicated in SARS-CoV's suppression of the innate immune responses, particularly antagonizing type-I interferon (IFN) signaling and chemokine and cytokine production [12; 13]. Simultaneous disruption of both activities, either by mutation in MERS CoV PLpro's Ub/Ub-like binding region [14], or a destabilizing mutation in MHV PLP's ubiquitin-like domain (Ubl) [10] has been observed to prevent antagonization of IFN signaling, chemokine and cytokine production, as well as viral pathogenesis respectively. Overall, these studies suggest that the deubiquitinating and deISGylating activities of PLPs, sometimes packaged together as deubiquitinating enzyme (DUB) activity, are a likely contributor to viral pathogenesis.

Intriguingly, the precise role of each individual activity in promoting PLPs ability to act as an IFN antagonist has yet to be precisely defined. So far, several X-ray structures of PLpro and PLP2 bound with Ub molecules have been reported [8; 15; 16]. However, no structure of any CoV PLP in complex with an ISG15 molecule has yet been reported. Due to the lack of structural detail about the interface between CoV PLPs and ISG15, understanding how CoVs PLPs specifically engage with ISG15s versus Ub has been especially difficult to understand. The lack of structural information has led to problems in defining the differences between CoV PLPs' deubiquitinating and deISGylating activities among different CoVs. A further complication in our understanding stems from the fact that the sequence identity of ISG15 among mammals is low, ranging from 58% to as low as 35% when a broader range of animals is compared (Figure 3.1b). In contrast, Ub is highly conserved among eukaryotes.

The sequence diversity of ISG15 among animals and the impact of this diversity on the recognition of these ISG15s by viral USPs has not been well studied despite the potential implications. For example, certain CoVs, such as SARS-CoV and MERS-CoV, are known to replicate and survive in a broad range of animals including bats, camels, mice, civets, shrews, badgers, pigs and humans [10; 17; 18]. In contrast, other CoVs such as MHV only replicate in mice, suggesting that some CoV PLPs may have evolved strict specificity for their single host's ISG15[19]. The potential for species-species variances in ISG15 have already been shown to be a key factor in other viruses including influenza B where it was shown that NS1 is unable to bind mouse ISG15 unlike its non-human primate and human counterparts limiting influenza B virus infection in mice [20; 21; 22]. Also, biodiversity that occurs between species within ISG15s was recently shown to impact the ability of nairovirus viral ovarian tumor domain proteases (vOTUs) to effectively process certain ISG15s [23]. Overall, many CoV PLPs have been observed to show robust

deubiquitinating activities; [11; 24] however, recent *in vivo* studies have started to unveil the importance of PLPs deISGylating activity [25; 26]. This has led to a need for a better and more detailed understanding of the interactions between CoV PLPs and ISG15 at the molecular level.

Adding to the ambiguity of how CoV PLPs or other deISGylating enzymes interact with ISG15, especially when it comes to understanding species-to-species variations, is the lack of available full-length ISG15 structures that have been determined. This is especially important when the intramolecular arrangement of the two domains of ISG15 is considered. For example, the hinge region of ISG15 shows a significant degree of sequence diversity between the different species (Figure 1b). Although several structures of human ISG15 (hISG15) have been reported, no complete structure of ISG15 from another species has been resolved. Moreover, the recent elucidation of the structure of the C-terminal domain portion of mouse ISG15 (mISG15) prompted questions on the impact of ISG15 biodiversity on the overall ISG15 structural fold [23].

To address these critical gaps in our understanding of ISG15 recognition by CoV PLPs, PLpro from SARS-CoV and MERS-CoV, as well as PLP2 from MHV, were examined for differences in their selectivity among ISG15s from various animals. The X-ray crystal structures of SARS-CoV PLpro bound to the C-terminal domain of ISG15 originating from mouse and human were determined and analyzed in conjunction with enzyme kinetic and thermodynamic data derived from ITC. In addition, the first X-ray structure of a complete non-human ISG15 structure, mouse ISG15 (mISG15), was also determined to elucidate potential sequence and structural differences that may account for species specificity of CoV PLPs. Together, these studies provide significant and new insight into the CoV PLP's ability to accommodate the structural differences not only between Ub and hISG15, but also different species ISG15s.

Results

Species specific cleavage of proISG15s by CoV PLPs

Currently, there is a paucity of available biochemical data on the impact of species-to-species sequence variations within ISG15 and the effect that these differences may have on the ability of CoV PLPs to recognize and cleave ISG15. Therefore, we employed a recently developed assay for deISGylating vOTUs that takes advantage of the ability of a protease or DUB to cleave immature ISG15 [23]. The PLpro enzymes from SARS-CoV and MERS-CoV, as well as the enzyme PLP2 from MHV, were purified and assessed for their ability to cleave proISG15s derived from 7 different species including human, sheep, northern tree shrew, jackknife fish, mouse, dromedary camel, and vesper bat (Figure 3.2). Each of these proISG15 proteins is appended with the proISG15 extension from *Homo sapiens* (Figure 3.2). ISG15 from jackknife fish was included in the analysis to add a more distantly related ISG15 homologue.

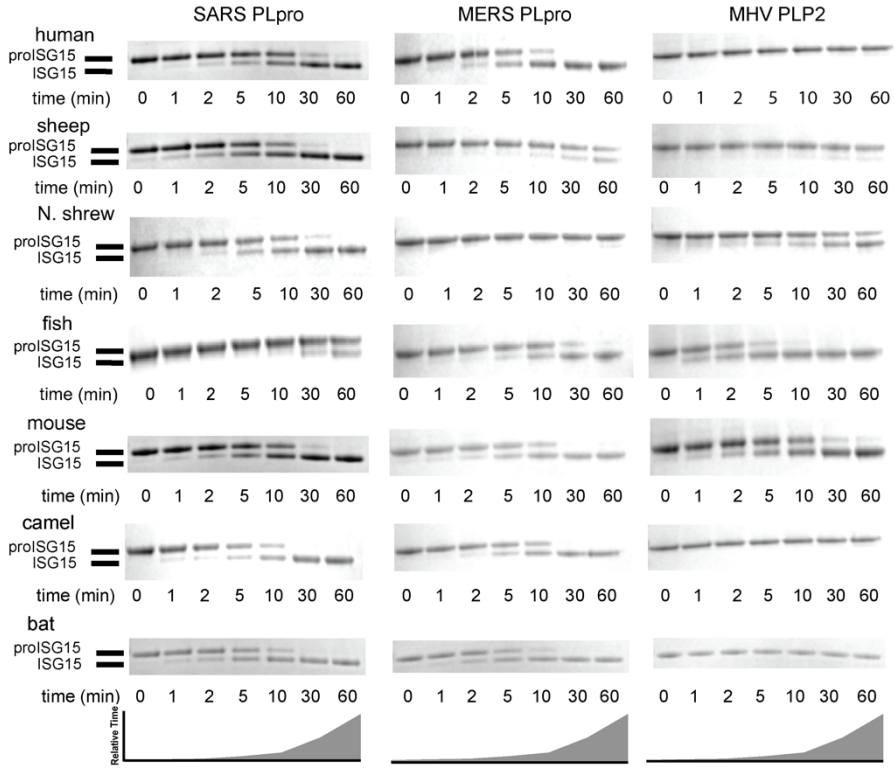

Figure 3.2 Cleavage profiles of SARS-CoV PLpro, MERS-CoV PLpro, and MHV PLP2 with proISG15s derived from human, sheep, northern tree shrew, jackknife fish, mouse, dromedary

camel, and vesper bat. Reactions were conducted at 37°C with 10 μM of each proISG15 and 20 nM of each PLpro/PLP2 with samples taken at the indicated time points.

SARS-CoV and MERS-CoV PLpros are both capable of fully processing proISG15 from human, mouse, camel and bat within 60 minutes. SARS PLpro is also able to fully process proISG15 from sheep and shrew within that same time but it has little to no activity against jackfish proISG15. In contrast, MERS PLpro is fully capable of processing jackfish proISG15 but it processes proISG15 from shrew and sheep poorly. MHV PLP2 on the other hand displays a much narrower specificity for ISG15s from different species. It shows little to no cleavage of proISG15s derived from human, sheep, camel, or bat sources but does show modest activity for the northern tree shrew. MHV PLP2 shows strong activity towards jackfish and mouse proISG15, the latter activity being consistent with MHV's pathogenicity as a murine CoV.

Species specific affinity of ISG15 for SARS-CoV and MERS-CoV PLpros

Analysis of the cleavage patterns in Figure 2 suggests that SARS and MERS PLpros are more promiscuous in recognizing and cleaving various proISG15s compared to MHV PLP2, which may relate to the fact that these human pathogens are capable of replicating in different hosts, e.g. bats, camels and the shrew, in contrast to MHV which can only replicate in the mouse. Differences in cleaving ability of proISG15s by SARS and MERS PLpro may be due to sequence and structural differences, which may affect binding affinities for the ISG15s. This possibility was explored using Isothermal Titration Calorimetry (ITC) to measure the binding affinities of different ISG15s missing the P'-sites (Table 3.1; Figure 3.3). Removal of the P'-sites was done to avoid potential confounding factors related to CoV PLPs other prominent function of processing the viral polyprotein to promote viral replication. This part of the process requires that PLPs recognize and cleave the peptide bond after the LXGG sequences within the polyprotein, and the ability of PLPs to cleave this bond has been shown to be reliant on residues flanking the peptide cleavage site [6; 9].

This requisite function is not associated with other viral deISGylating proteases such as nairovirus vOTUs [23]. Therefore, ITC measurements were performed using ISG15 substrates missing the pro-sequence so the binding affinity could be assessed independent of any P'-sites contribution associated with using the ISG15-pro-form protein.

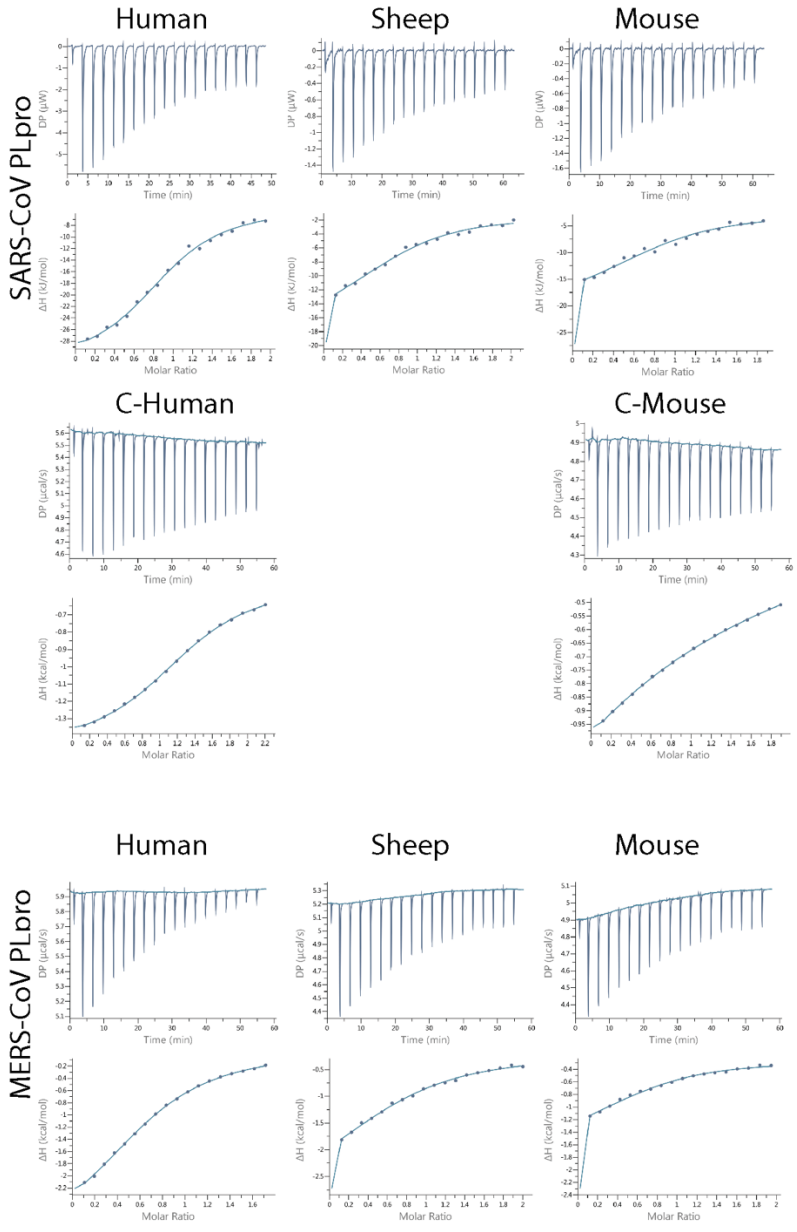

Figure 3.3 ITC binding isotherms with the raw heat (top panel) and the integrated heats of injection (bottom panel) shown for each interaction.

Table 3.1 Isothermal Titration Calorimetry.

Protein	N (sites)	K_D (μM)	ΔH (kJ/mol)	ΔG (kJ/mol)	-TΔS (kJ/mol)
SARS-CoV PLpro					
Human	0.932 ± 0.032	20.50 ± 4.48	-27.20 ± 1.90	-26.80	0.38
C-Human	1.31 ± 0.015	57.6 ± 3.21	-4.03 ± .019	-24.18	-20.17
Sheep	1	200 ± 41	-106 ± 10	-21.10	84.8
Mouse	1	196 ± 68	-92 ± 15	-21.20	70.4
C-Mouse	1	1870 ± 173	-20.71 ± 0.486	-15.56	5.10
MERS-CoV PLpro					
Human	0.785 ± 0.027	59.3 ± 12.7	-11.34 ± 0.268	-24.15	-12.80
Sheep	1	172 ± 38.5	-19.92 ± 0.420	-21.51	-1.59
Mouse	1	376 ± 52.8	-43.51 ± 0.535	-19.54	24.10

Intriguingly, both SARS-CoV and MERS-CoV PLpro have stronger affinity toward hISG15 than shISG15 and mISG15. The dissociation constants (K_d) of SARS-CoV and MERS-CoV PLpro for hISG15 are 20.5 ± 4.5 μM and 59.3 ± 4.5 μM, respectively. Unlike their affinities for hISG15, the affinities of both PLpros for shISG15 and mISG15 were significantly weaker and as a result, a competitive ITC binding assay (Table 3.1; Figure 3.3) had to be used to determine their K_d values. In regards to SARS-CoV PLpro, ITC analyses revealed similar K_d's of 200 ± 41 μM and 198 ± 64 μM for shISG15 and mISG15. More divergence in affinity for mISG15 and shISG15 were seen with MERS-CoV PLpro. Like SARS-CoV PLpro, affinity of MERS-CoV PLpro for shISG15 was similar with a K_d of 147 ± 36 μM. However, a substantially weaker affinity of MERS-CoV PLpro for mISG15 was observed (K_d of 376 ± 53 μM).

The measured thermodynamic parameters revealed that both SARS-CoV and MERS-CoV PLpro follow a similar trend and prefer hISG15 over shISG15 and mISG15. Specifically, the association of shISG15 and mISG15 to PLpros is unfavorable with increasingly higher entropic factors. Although PLpros originating from MERS-CoV and SARS-CoV exhibited a similar preference for hISG15, the thermodynamics driving the affinity differ. The SARS-CoV and

hISG15 binding event was driven by enthalpic factors and was slightly entropically unfavorable. In contrast, the MERS-CoV affinity of hISG15 was more balanced possessing an entropic and enthalpic component.

Crystallization of SARS-CoV PLpro bound to the C-terminal domains of human and mouse ISG15

While X-ray crystal structures have been solved of SARS and MERS PLpro bound to Ub, our understanding of the interactions of these enzymes with ISG15 has been largely limited to enzymatic, mutational and computational modeling studies [11; 15]. To gain molecular insight into the specific interactions between PLPs and ISG15, we crystallized and determined the X-ray structures of SARS PLpro bound to the C-terminal domains of ISG15 from both human (ChISG15) and mouse (CmISG15). Attempts at co-crystallization of full-length ISG15s from human and other species with SARS CoV PLpro, as either various covalent adducts or non-covalently bound species, were made but were unsuccessful. However, the complex of SARS-CoV PLpro bound to the C-terminal domain of human ISG15 (ChISG15), which is the principle binding domain of ISG15, crystallized readily[11]. Specifically, we utilized a form of ChISG15 and CmISG15 that were modified with propargylamine at the c-terminus (ChISG15-PA or CmISG15-PA) to form a suicide substrate that covalently links to the active site cysteine. From here on in, these covalently modified complexes of SARS PLpro are designated to as SARS-CoV PLpro-ChISG15 and SARS-CoV PLpro-CmISG15 for simplicity.

X-ray SARS-CoV PLpro bound to the C-terminal domain of human ISG15

The X-ray structure of the SARS-CoV PLpro-ChISG15 complex was determined to 2.62 Å with two complete copies of SARS-CoV PLpro-ChISG15 within the asymmetric unit (Table 3.2). The structure of CoV PLPs contains the classic tertiary fold associated with PLPs consisting of the finger, palm, thumb, and ubiquitin-like (Ubl) domains (Figure 3.4a). However, despite

sharing the same tertiary fold, the manner in which SARS-CoV PLpro engages the C-terminal domain of hISG15 is distinct from that of Ub. Overlaying the SARS-CoV PLpro-ChISG15 structure with the structure of SARS-CoV PLpro with mono-Ub (PDB entry 4MM3) reveals that, compared to Ub, ChISG15 is shifted by approximately 12° in its global orientation (Figure 3.4b).

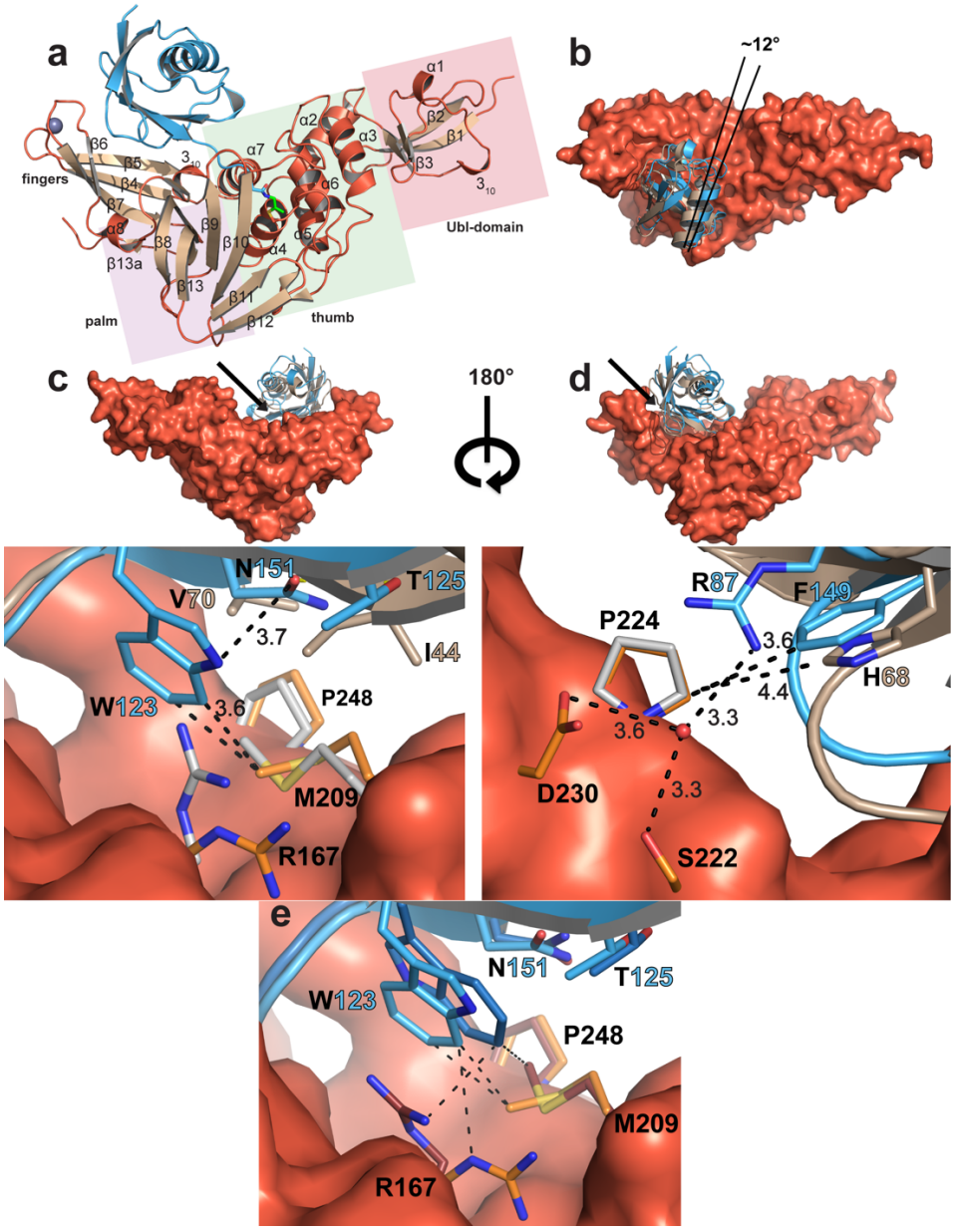

Figure 3.4 (a) Cartoon representation of the SARS-CoV PLpro complexed with ChISG15 (blue). Secondary structure of the PLpro is designated, with helices and loops rendered in reddish orange and β-sheets rendered in wheat. The structural domains of the PLpro are identified, consisting of the fingers (white), palm (purple), thumb (green), and Ubl (red) labeled with colored boxes. The

vinyl thioether propargylamine linker is colored green, and the Zn(II) ion in light purple. (b) Overlay of ChISG15 (blue) bound to SARS PLpro (reddish orange) compared to a Ub (light brown)-bound structure (PDB entry 4MM3) based on a secondary structure alignment of the respective PLpros. The approximate degree of shift in orientation of analogous α-helices is indicated. (c) Comparison of the interaction of ChISG15 (blue) versus Ub (light brown) with the hydrophobic patch of SARS-CoV PLpro, with the site of interaction within the overall structure indicated by an arrow. Side chain conformations of the PLpro are colored orange for the ChISG15 bound structure, gray for the Ub-bound structure. Residues E127-D133 of ChISG15 and A46-T55 of Ub were removed for clarity. Inter- and intramolecular distances (Å) are shown by black dashes. (d) Comparison of ChISG15 versus Ub at the site of the additional hydrophobic interaction in the ChISG15-bound structure. Colored as in (c). Intermolecular distances (Å) are shown as as black dashes. (e) Interchain variability of ChISG15 Trp123 in binding to SARS-CoV PLpro. The two copies within the asymmetric unit were overlaid based on a secondary structure alignment of the PLpros. Side chains of the PLpro colored in orange correspond to the ChISG15 colored light blue, and the PLpro side chains colored burgundy to the ChISG15 colored a darker blue. Intermolecular distances are colored in black. Residues E127-D133 of ChISG15 omitted for clarity.

Table 3.2. Data collection and refinement statistics.

	SARS-CoV PLpro-ChISG15 (PDB entry 5TL6)*	SARS-CoV PLpro-CmISG15 (PDB entry 5TL7)*	mISG15 (PDB entry 5TLA)*
Data collection			
Space group	$P2_12_12_1$	$P2_12_12_1$	P2
Cell dimensions			
a, *b*, *c* (Å)	46.9, 87.0, 221.5	76.0, 98.2, 106.6	85.8 60.2 172.7
α, β, γ (°)	90, 90, 90	90, 90, 90	90, 93.1, 90
Resolution (Å)	50.00-2.62 (2.67-2.62)†	50.00-2.44 (2.53-2.44)†	50.00-3.25 (3.31-3.25)†
R_{sym} or R_{merge}	11.1 (58.3)	9.9 (74.2)	5.2 (37.5)
$I / \sigma I$	12.7 (2.07)	18.0 (2.71)	17.4 (2.27)
Completeness (%)	98.4 (96.0)	99.1 (99.8)	98.4 (88.0)
Redundancy	5.0 (3.9)	2.4 (2.1)	2.4 (2.1)
Refinement			
Resolution (Å)	38.67-2.62 (2.71-2.62)	32.20-2.44 (2.53-2.44)	42.18-3.25 (3.36-3.25)
No. reflections	27,644	29,886	27,929
R_{work} (%)/ R_{free} (%)	19.1/25.0	18.7/25.3	25.6/30.9
No. atoms			
Protein	6177	6218	11,491
Ligand/ion	15	10	0
Water	133	231	0
B-factors			
Protein	49.27	61.13	86.7
Ligand/ion	59.94	57.02	0
Water	41.95	58.23	0
R.m.s. deviations			
Bond lengths (Å)	0.004	0.008	0.002
Bond angles (°)	0.54	1.1	0.57

*Datasets collected from a single crystal for each structure. †Values in parentheses are for highest-resolution shell.

Closer examination of the binding interface uncovered key differences in how each substrate engages the surface of the SARS-CoV PLpro. Although there is only a minor variation surrounding a 180° flip of Trp123 between the two copies of ChISG15 in the asymmetric unit, both ChISG15 chains are analogous in how they are accommodated by SARS-CoV PLpro compared to Ub (Figure 3.4e). The differences appear to be driven by how hISG15 and Ub differ in their ability to interact with a hydrophobic region consisting of residues Arg167, Met209, and Pro248. For Ub, the interactions with this region occur by means of a hydrophobic patch consisting of Ile44, Val70, and Leu8 [15]. In contrast, ISG15 lacks such a hydrophobic patch. The interaction is primarily driven by two distinct sets of hydrophobic interactions: hISG15's Trp123 with Met209 of the protease's palm region, and hISG15's Phe149 with a second hydrophobic site driven by Pro224 of the protease's fingers region (Figures 3.4c, d). Surprisingly, while the Ub-bound structure contains other polar and water-mediated interactions between Ub and the palm region of the PLpro, such interactions seem to be less pronounced in the more charged ChISG15 structure [15]. Overall, there are only a few water molecules present within the interface between PLpro and ChISG15 compared to the larger number that are observed in the Ub-bound structure potentially indicating a lesser role of water-mediated hydrogen bond interactions in the binding of hISG15.

To gain a better understanding of the residues mediating specificity for Ub or ISG15, mutants targeting the palm and fingers regions of the of SARS-CoV PLpro were constructed and their catalytic activities towards various substrates were determined (Figure 3.5, Table 3.3). These substrates included Ub- and ISG15-AMC, which are composed of the respective substrate derivatized with the fluorescent leaving group 7-amido-4-methylcoumarin. Additionally, the small peptide Z-RLRGG representing the consensus recognition sequence for both Ub and ISG15

also attached to AMC was included to probe for potential changes affecting protein-protein interactions versus changes that impact intrinsic catalytic activity.

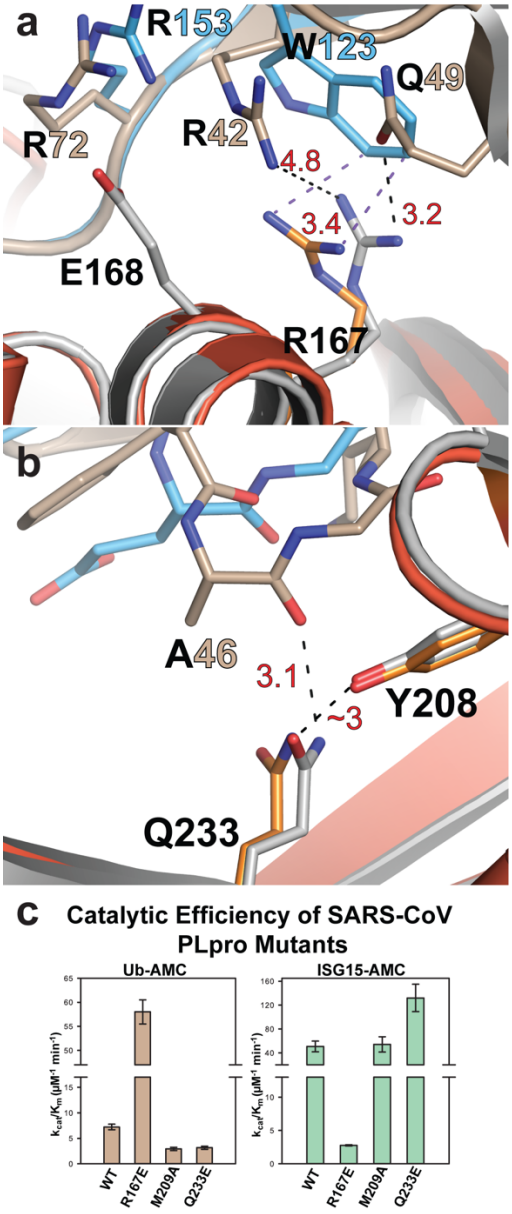

Figure 3.5 (a) and (b) Sites within the ChISG15- and Ub-bound SARS-CoV PLpro structures corresponding to the mutations causing increased Ub-AMC activity (top) versus increased ISG15-AMC activity (bottom). Structures shown as cartoons, colored as in (4c). Intermolecular distances to indicate proximity are shown as black dashes. (c) Activity of SARS-CoV PLpro mutants towards Ub-, and ISG15-AMC. Corresponding data found in Table 3.3.

Table 3.3. Kinetic Parameters of SARS PLpro WT and mutants with different ubiquitin-based fluorescent substrates.

Substrate	**SARS PLpro Enzymes**			
Kinetic Parameter	**WT**	**R167E**	**M209A**	**Q233E**
RLRGG-AMC[a]				
k_{cat}/K_m (μM^{-1} min^{-1})	0.141 ± 0.002	0.062 ± 0.001	0.727 ± 0.007	0.211 ± 0.002
Ub-AMC[a]				
k_{cat}/K_m (μM^{-1} min^{-1})	7.22 ± 0.56	58.0 ± 2.5	2.90 ± 0.32	3.14 ± 0.32
ISG15-AMC[b]				
k_{cat}/K_m (μM^{-1} min^{-1})	50.7 ± 9.0	2.76 ± 0.10[a]	54.3 ± 12.8	132 ± 23

[a]Best-fit slope values derived k_{app} for nonsaturating substrates and approximates k_{cat}/K_m

[b]Steady-state values following Michaelis-Menten kinetics are reported from duplicate measurements

One of the mutants, M209A, reduces the activity towards Ub-AMC by almost two-fold and increases its activity towards Z-RLRGG-AMC by nearly five-fold, while retaining wildtype levels of activity for ISG15-AMC. From a structural prospective, the reduction of Ub-AMC activity is not surprising as M209A shrinks the hydrophobic patch that engages the Ile44 centered hydrophobic patch in Ub. The observed increase of the activity towards Z-RLRGG-AMC is less straightforward. M209 lacks direct interaction with the last five amino acids of Ub, or ISG15. However, its replacement by alanine could sterically open up a space that is more accommodating for the artificial Z-adduct of the peptide. The other two mutants were found to have increased catalytic efficiencies for processing either Ub or ISG15 with a corresponding reduction in activity for the other. R167E is over eight times more efficient than the wild type enzyme at hydrolyzing Ub but is about 20-times less efficient at hydrolyzing ISG15 (Figure 3.5c).

In contrast, Q233E is nearly three-fold more efficient than wildtype at hydrolyzing ISG15 and two-fold less efficient hydrolyzing Ub. In the case of Ub, the mono-Ub structure suggests the charge flip with R167E may introduce an additional electrostatic interaction with either Arg42 or

Gln49 of Ub. For the ChISG15 structure, this change occurs in close proximity to the interaction between Trp123 and Met209. Examination of the structure reveals Arg167 may contribute to π-π interactions involving Trp123 and Arg153 of ChISG15 (Figure 3.4e, Figure 3.5a). Replacing the longer and positively charged arginine with the shorter glutamate removes this contribution. Additionally, this charge flip may disrupt the electrostatic interaction between Arg153 and Glu168 of the PLpro, potentially resulting in a loss of affinity for ChISG15. For Q233E, the change from a neutral polar to a charged group may create a potential electrostatic repulsion with the backbone carbonyl of Ala46 in Ub (Figure 3.5b). For the ChISG15 structure, in comparison, there is not a clear direct interaction between PLpro and ISG15 that would be affected. This suggests that the impact of this mutation may stem from internal changes within the PLpro regarding the flexibility of the finger region rather than direct interactions with the substrate.

X-ray Structure of SARS-CoV PLpro bound to the C-terminal domain of mouse ISG15

In light of the differences in the nature of interactions between different species' ISG15s revealed by ITC, as well as the apparent plasticity that can occur between Ub and hISG15 within the SARS-CoV PLpro active site, insights into the structural sources of this phenomenon were sought. To this end, a structure of SARS-CoV PLpro with the C-terminal domain of mISG15 (CmISG15) was determined to a resolution of 2.4 Å (Figure 3.6a). The structure of the catalytic core domain of SARS-CoV PLpro is consistent with the structure of the ChISG15 SARS-CoV PLpro structure. However, a major difference in the orientation of the Ubl domain of SARS-CoV PLpro is observed when bound to CmISG15. Unlike previous SARS-CoV PLpro structures where the Ubl domains differs only slightly in its position/orientation to the catalytic domain or is unobservable because of weak electron density suggesting potential flexibility, the Ubl in the SARS-CoV PLpro-CmISG15 structure takes a sharp, almost 90° turn in orientation when

compared with previous X-ray structures (Figure 3.6c). The new orientation does not appear to form contacts with the bound CmISG15 suggesting that there is no direct influence on the Ubl to adopt this conformation. Further analysis of the new orientation reveals a seam made up of several electrostatic interactions between the Ubl domain and the thumb domains of the PLpro, indicating that this orientation can be stabilized (Figure 3.6b).

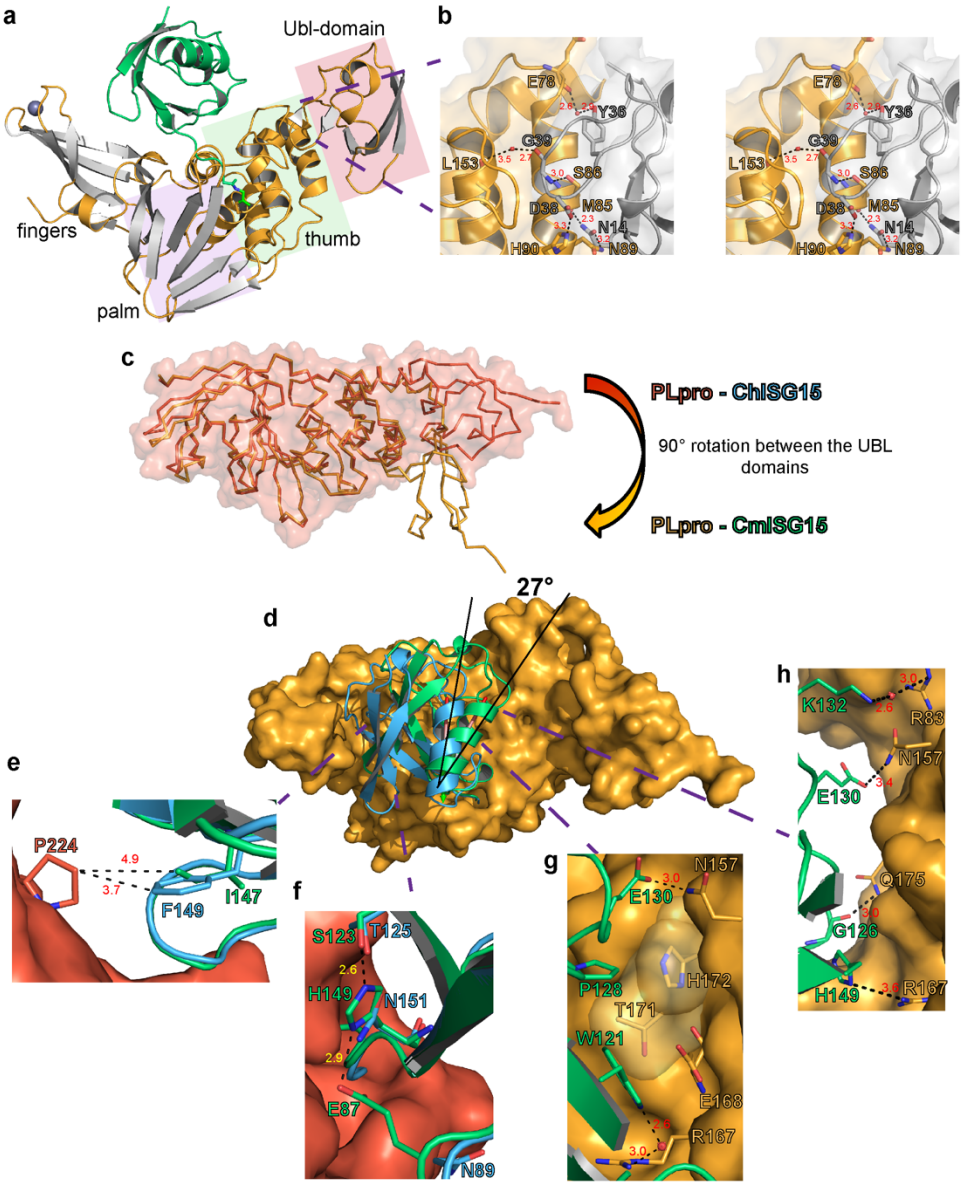

Figure 3.6 (a) Cartoon representation of the SARS-CoV PLpro complexed with CmISG15 (green). Secondary structure of the PLpro is designated, with helices and loops rendered in gold and β-sheets rendered in silver. The structural domains of the PLpro are identified, consisting of the

fingers (white), palm (purple), thumb (green), and Ubl (red) labeled with colored boxes. (b) Cartoon representation in wall-eye stereo view, with transparent surfaces, of the interactions between the thumb domain (gold) and Ubl-domain (gray) for the SARS-CoV PLpro-CmISG15 bound structure. Amino acids involved in interactions are represented as sticks and hydrogen bonds are indicated by black dashes and distances (Å) labeled in red. (c) Ribbon overlay of SARS-CoV PLpro complexed with CmISG15 (gold) and SARS-CoV PLpro complexed with ChISG15 (reddish orange) demonstrating the movement of the Ubl-domain. (d) Overlay of SARS-CoV PLpro (gold) complexed with CmISG15 (green) and the ChISG15 (blue) from the SARS-CoV PLpro complex based on a secondary structure alignment of the respective PLpros. The approximate degree of shift in orientation of analogous α-helices is indicated. (e/f) Comparison between the SARS-CoV PLpro (reddish orange) complexed with ChISG15 (blue) and CmISG15 (green). Electrostatic interactions indicated with black dashes and distances (Å) labeled in red or yellow, respectively. (g/h) Interactions between SARS-CoV PLpro (gold) and CmISG15 (green) with electrostatic interactions indicated with black dashes and distances (Å) labeled in red and hydrophobic interactions indicated by the yellow transparent surface.

The Ubl domain was not the only global difference between the SARS-CoV PLpro-CmISG15 and SARS-CoV PLpro-ChISG15 complexes. Surprisingly, the global orientation of CmISG15 is tilted 27° away from the fingers in SARS-CoV PLpro (Figure 3.6d). Interestingly, four amino acids appear to explain the lack of CmISG15's accommodation in the same orientation to that of bound ChISG15. At position 149 in ChISG15 and 147 in CmISG15, there is an amino acid difference of a phenylalanine and an isoleucine respectively (Figure 3.6e). This change in CmISG15 eliminates the hydrophobic interaction with the fingers region of SARS-CoV PLpro seen in the ChISG15 bound structure and likely aids in the tilt toward the Ubl domain. In addition, there is a change from Asn89, Thr125, and Asn151 in ChISG15 to Glu87, Ser123, and His149 in CmISG15 (Figure 3.6f). These amino acid differences create a hydrogen bond network between Glu87, His149, and Ser123 in the CmISG15, which is absent in the ChISG15 bound structure. This network locks the Glu87 into an unfavorable position for CmISG15 to bind in the same manner as ChISG15. The unfavorable position ultimately results in repulsion of CmIG15 against PLpro.

In concert with a loss of the hydrophobic interaction with the finger region and potential electrostatic repulsions CmISG15 would incur in binding in the same orientation of ChISG15, the CmISG15 bound orientation facilitates the formation of numerous favorable interactions. Consistent with the X-ray structures of other deISGylases bound to the C-terminal domain of human ISG15 [27; 28], the conserved Trp121 of mISG15 is centric to the interface. However, unlike the interaction observed in the SARS-CoV PLpro-ChISG15 structure, Trp121 in the mISG15 does not insert into a hydrophobic pocket. Instead, mISG15's Trp121 and Pro128 form significantly smaller hydrophobic interaction with SARS-CoV PLpro via the proteses's extended alkyl chain of Glu168 generated by the hydrogen bond formed between it and Thr171. In contrast to the bound ChISG15 and outside the last five C-terminus consensus amino acids of Ub and ISG15, this weak hydrophobic interaction between CmISG15 and the protease is the only one observed.

In addition to the hydrophobic binding contributions of mISG15 Trp121, a water molecule is observed to mediate a hydrogen-bonding network between Trp121's indole nitrogen and several nearby PLpro residues (Figure 3.6g/h). Including this hydrogen bond network, CmISG15 forms almost 40% more hydrogen bonds with the protease then observed with ChISG15. One set of these additional electrostatic interactions are centered around SARS-CoV PLpro's Arg83 and CmISG15's Lys132. Others are also observed to form between SARS-CoV PLpro's Asn157, Gln175 and Arg167 and CmISG15's Glu130, the carbonyl of Gly126, and His149 respectively (Figure 3.6g/h). Taken overall, the interface of bound CmISG15 of 872.5 $Å^2$ is similar in size to that of the ChISG15 ~767 $Å^2$ interface, but consists of predominately electrostatic interactions whereas the former has a significantly greater hydrophobic component. In line with this, a greater number of water molecules, approximately 10, can be observed within the interface further indicating the degree to which binding may be driven by more hydrophilic interactions. This

difference may be one of the contributing factors to the overall reduction in binding affinity observed for full-length mISG15 when compared to hISG15 via ITC.

X-ray structure of the full-length, unbound form of mouse ISG15 and comparison human ISG15

Whereas some viral deISGylating enzymes, such as vOTUs, are thought to exclusively interact with the C-terminus of ISG15, SARS PLpro has been shown to contain two Ub-binding sites that likely engage the N-terminus of ISG15s [11; 15]. With only the full-length hISG15 structure available, the impact of ISG15 biodiversity within the N-terminal region has been difficult to assess. To address this issue, the X-ray structure of mISG15 with both domains was determined to assess conformational variability of mISG15 compared to hISG15. Initially, only a low resolution (4 Å) structure could be determined. Truncation of the last five non-structured amino acids led to a structure that could be determined to a higher resolution of 3.25 Å. Using the program Define Secondary Structure of Proteins (DSSP), the secondary structure of mISG15 was determined to be comparable to hISG15. mISG15 contains nine beta sheets, two helices, but only two 3_{10} helices within the C-terminal domain; this differs from the hISG15 which contains two 3_{10} helices per domain of ISG15 (Figure 3.7a)[29]. The asymmetric unit consists of 2 twisting filaments, containing 10 copies of mISG15. Upon examining the differences between the monomers within the asymmetric unit, some flexibility between N- and C-terminal domains was observed (Figure 3.7b/c). This flexibility was probed by aligning the C-terminal domains of each mISG15 monomer and measuring the angle between the point of divergence and the farthest N-termini. There is a 20.2° range of motion between the N- and C-terminal domains of mISG15 (Figure 3.7b). Comparable flexibility was also observed in hISG15 structures, with a 18.3° range of motion (Figure 3.7c) (PDB: 1Z2M, 3R66, 3PSE) [28; 29; 30].

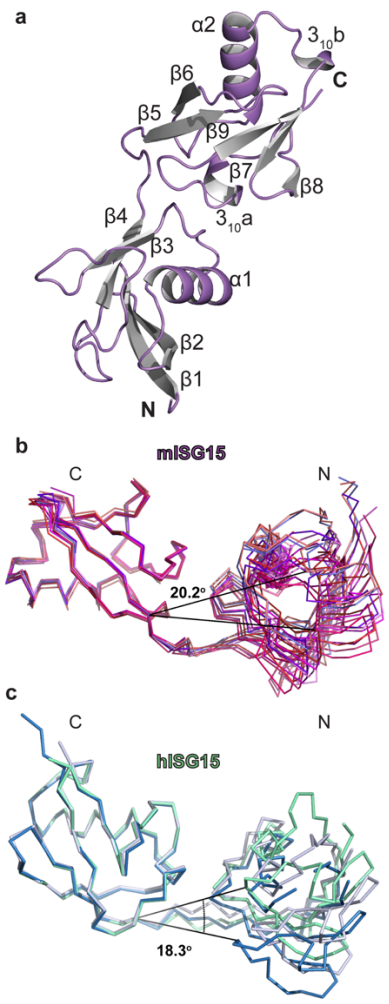

Figure 3.7 (a) Secondary structure of monomer A of full-length mISG15 (purple) with β-sheets colored in silver. (b) Monomers of mISG15 were overlaid, aligning the C-terminal domains, to observe the flexibility of the monomeric units. (c) Monomers of hISG15 (green; PDB 1Z2M, gray; PDB 3R66, blue; PDB 3PSE) were overlaid, aligning the C-terminal domains, to observe the flexibility of the monomeric units.

While each individual domain of hISG15 and mISG15 are similar in secondary structure and both show some structural variability between monomers, there is a drastic difference in the overall conformations of the tertiary structures between mISG15 and that of hISG15. This surprising difference is observed in the overall arrangement of the N- and C-terminal domains. Specifically, the twist about the C- and N-terminal domain of mISG15 in relation to hISG15 ranges from 43.0º to 66.9º (Figure 3.8a). Closer investigation reveals that differences in tertiary

arrangement can be attributed to several molecular interactions within the structures driven by the primary sequence differences of mISG15 compared to hISG15. Specifically, the presence of Asp79 creates a kink in the hinge region of hISG15 as a result of the carboxylate group of Asp79 forming a hydrogen bond with the hydroxyl group of Thr101 (Figure 3.8b). This interaction does not occur in mISG15 since Ser77 replaces Asp79.

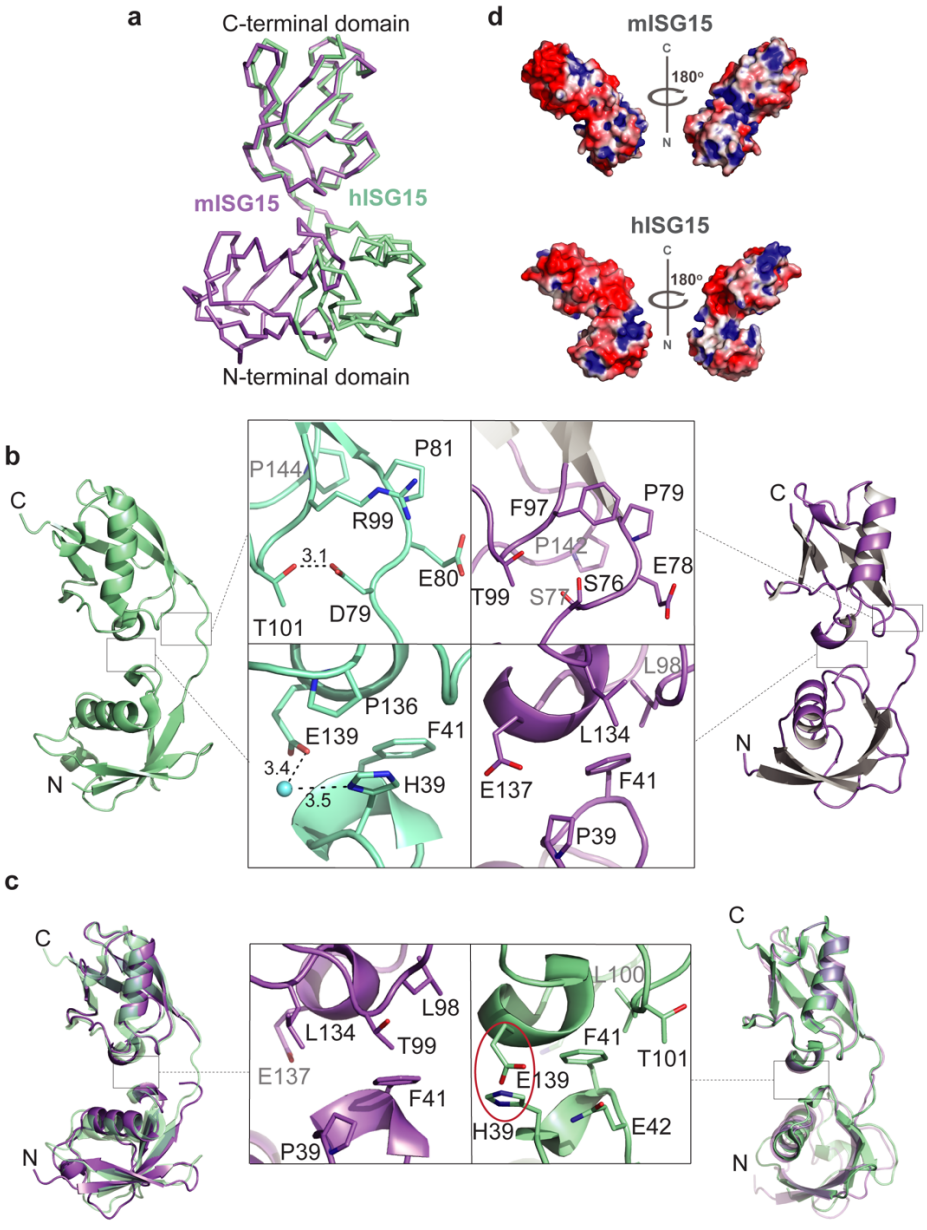

Figure 3.8 (a) Overlay of mISG15 (purple) and hISG15 (green; PDB 1Z2M) shown in ribbons. (b) Comparison of interactions responsible for the structural conformations of hISG15 (green) and

subunit A mISG15 (purple) with dashed lines representing bond lengths in Å. (c) Interactions observed when mISG15 is forced into the hISG15 conformation (left panel) and vice versa (right panel). (d) Electrostatic surface of mISG15 and hISG15.

While amino acids in the hinge may play a part in the different conformational trajectory allowed in the region between the two domains in mISG15, the twisted feature of mISG15 may be stabilized by amino acid interactions in the core region of the protein. This core region is centered near Phe41, at the interface between the two domains. The hydrophobic interaction between the N-terminal and C-terminal domain at Leu134 and Phe41 may stabilize mISG15s' twisted arrangement (Figure 3.8b). Other residues in close proximity, such as Pro39, appear to further stabilize this hydrophobic interaction in mISG15. Specifically, Pro39 in mISG15 forms hydrophobic interactions with Phe41 contributing to the stabilization of mISG15s' tertiary arrangement (Figure 3.8b).

In addition to the presence of favorable interactions, steric clashes are also likely responsible for preventing the occurrence of a shared tertiary arrangement between the mISG15 and hISG15 species. When the N-terminal and C-terminal domains of mISG15 are configured to the arrangement of hISG15, there are no obvious clashes that prohibit mISG15 from adopting this conformation (Figure 3.8c). However, hISG15 may be incapable of adopting the mouse conformation due to the potential steric clash between His39 and Glu139 that typically form a water mediated interaction (Figure 3.8c). Thus, the presence of the His39 residue may prevent hISG15 from configuring to the mISG15 conformation.

Beyond the effects on tertiary structure, the sequence divergence between mISG15 and hISG15 also impacts the potential binding surfaces. These differences in amino acid sequence also give rise to different electrostatic potential plots. Unlike mISG15, hISG15 contains an uninterrupted negative surface band spanning across the two domains (Figure 3.8d). When the

surface of mISG15 corresponding to the same area is examined, this negative band dissipates as the comparable area on mISG15 is scattered with positive and neutral areas.

Discussion

Differences in hISG15 and mISG15 structure influence recognition by PLPs

Among Ub and Ub-like proteins, ISG15 is unique for more than its divergent amino acid sequence. Similar to other Ub-like proteins, ISG15 has not been observed to form polymeric chains like Ub [31]. However, ISG15 is the sole family member of ubiquitin-like modifiers that is comprised of two Ub-like folded domains. These two domains are tethered by a polypeptide linker that would suggest that the two domains can move freely and independent of each other. However, the four structures of hISG15 alone, or bound to viral proteins suggest the opposite (Figure 3.7c) [27; 28; 29; 30]. Akin to polymeric Ub, ISG15 appears to have relatively limited conformations between the two domains. The structure of mISG15 (Figure 3.7b) furthers this assertion with one important caveat, one species ISG15s domain configuration may not be necessarily representative of others, or ISG15s in general.

In both hISG15 and mISG15 there is a hydrophobic interface mediated by a conserved phenylalanine (Phe41, see Figure 3.8). The highly-conserved nature of this phenylalanine and other surrounding residues suggests that ISG15s in general likely utilize hydrophobic forces to adhere the two domains together (Figure 3.1b, residues involved are boxed in blue). However, as shown with mISG15, the influence of the core on orientation of the domains can vary. In mISG15, residues forming the core solely dictate its inter-domain orientation, whereas in hISG15 additional electrostatic interactions involving Glu139 and His39, and to a lesser extent Thr101 and Asp79, appear to play an additional role to favor one orientation over another (Figure 3.8b,c). Intriguingly, the pairing of Glu139 and His39 is extremely unique to hISG15. Although Glu139 or another

acidic residue is well conserved at that position, His39 is typically a proline. In hISG15, it appears that this favorable electrostatic interaction may promote hISG15's domain orientations. Multiple crystal structures reveal this conformation to be consistent despite differences in space groups and crystallization conditions, suggesting the observed tertiary structure a stable and likely preferred conformation (Figure 3.7c). In addition to favoring hISG15's conformation, His39 may also act as a steric block preventing hISG15 from adopting a similar tertiary structure and conformation as that of mISG15.

The observation of a potential steric block may result in MHV PLP2 not being able to recognize hISG15 which is why no cleavage of pro-hISG15 is observed (Figure 3.2). In contrast, no apparent steric hurdle is present for mISG15 in adopting a hISG15 like inter-domain orientation which maybe why SARS and MERS PLpro are able to readily recognize mISG15. The lack of a steric hurdle might suggest that there are more allowable domain arrangements of mISG15 than hISG15 in solution that allow for a broader spectrum of PLPs to recognize mISG15. The potential uniqueness of hISG15's structure may also fall in line with the inability of other viral proteins, such as influenza NS1, to effectively engage ISG15s beyond those of human and primates [30]. Moreover, the distinctiveness of hISG15 may also fit into the recent assertions that hISG15 plays a divergent immune regulation role in humans than in other animals [32].

Viral USP-Like PLPs accommodation of Ub versus ISG15s

Ub interactions with proteins possessing an ubiquitin binding site have been observed to be reliant largely on the involvement of a hydrophobic patch comprised of several residues surrounding Ile44 [15]. The absence of such a comparable patch in ISG15 as well as the more generally charged surface of hISG15 naturally spurred speculation on mechanisms behind how PLPs may engage ISG15s. The SARS-CoV PLpro-ChISG15 complex reveals that in PLPs the

binding interface may have evolved to recognize specific features of ISG15s from different species outside the five amino acid, C-terminal sequence (Arg-Leu-Arg-Gly-Gly), they share with Ub. For hISG15, this includes not only the highly conserved Trp123 of ISG15s, but also specific interactions that are unique to hISG15. For instance, Arg87 in hISG15 is often substituted for a lysine residue that is too short form any water mediated interactions with the SARS-CoV PLpro's Asp230 and Ser222. Interestingly, Phe149, which forms a second hydrophobic interaction site with the protease's Pro224, is one of the three amino acids recently implicated in species specificity among nairovirus vOTUs [23]. Residue changes between hISG15 and mISG15 at the other two positions, Asn151 and Asn89, appear to impede the accommodation of mISG15 in the active site of SARS-CoV PLpro compared to the more favorable hISG15 orientation. This appears to advocate that differences at these three ISG15 positions have a broader range of influence beyond only one class of viral proteases and could conceivable represent an evolutionary pressure that underlies part of ISG15 sequence diversity. Also, SARS-CoV residues that interact with these residues as well as SARS-CoV PLpro deubiquitinating and deISGylating altering mutants, R167E, M209A, and Q233E, may offer advantageous starting points for developing SARS-CoV PLpros with directed shifts in substrate specificities.

Beyond the C-terminal domains interaction with PLPs, the N-terminus of human ISG15 has been previous proposed to interact with a ridge helix spanning the conical PLP thumb domain with the Ubl domain to enhance affinity. Currently, no X-ray structures of an PLP with full-length ISG15 exist and previous computational models utilizing existing SARS-CoV PLpro structures bound with mono-Ub have had difficulty reconciling the significant gap that occurs between hISG15's N-terminal domain and the protease when anchoring C-terminal hISG15 domain on bound Ub. The SARS-CoV PLpro-CxISG15 structures offer two synergistic explanations. First,

the 6.3 Å shift of ChISG15 relative to bound Ub translates the N-terminal domain towards the ridge helix (Figure 3.9a). In addition, the alternate Ubl conformation found in the SARS-CoV PLpro-CmISG15 structure reveals that such a conformation translates the ridge helix up to 14 Å toward the location of the ridge helix (Figure 3.9b/c). Interestingly, comparing this model to the X-ray structure of SARS-CoV PLpro bound to K48-linked di-Ub highlights that different facets of the Ub-like fold found in the N-terminal domain ISG15 are likely involved in the interaction (Figure 3.9d). Specifically, in this model a triple serine repeat, Ser20-22, and Glu27 located in hISG15's $\beta 2\alpha 3$ loop and $\alpha 3$ respectively point toward the protease's ridge helix creating a surface that is available to engaged by the bevy of charged and polar residues located on SAR-CoV PLpro's ridge helix that has been previously implicated in binding[15]. The impact of mISG15's divergent domain orientation from hISG15 is also apparent. Initial molecular modeling of the hISG15 structure onto the CmISG15-bound SARS-CoV PLpro structure with CmISG15 as an anchor reveals a steric clash with the ridge helix. This is the same for hISG15 drawn from any of its known X-ray structures. However, the divergent inter-domain orientation found in full-length mISG15 structure determined here allows for the mISG15's N-terminal domain to fit unobstructed (Figure 3.9e). The significant domain-domain orientations differences between hISG15 and mISG15 also result in a much smaller mISG15 and more barren surface. Specifically, mISG15's $\alpha 1\beta 3$ loop comprises the surface oriented towards the ridge helix. Intriguingly, this surface is also devoid of sidechains due to its composition and structure. Overall suggesting that ISG15's N-terminal domains may engage to differing degrees with the protease's ridge helix, or at all. The need for PLPs not only to accommodate surface differences between species ISG15s, but also divergent inter-domain orientations highlight the difficulties for a CoV PLP to be active to all species ISG15s. This could also be perceived as a possible benefit to ISG15's unique tandem Ub-

like arrangement. Also, the improved structural perspective on how the N-terminus of ISG15s from different species may engage CoV PLPs provides a clearer path towards utilizing this region to influence deIGylating activities of CoV PLPs. As a result, combining this information along with the alterations possible in the C-terminal domain, fresh tools to addressing the role of deubiqutination and deISGylation through the use of reverse genetics systems can be envisioned.

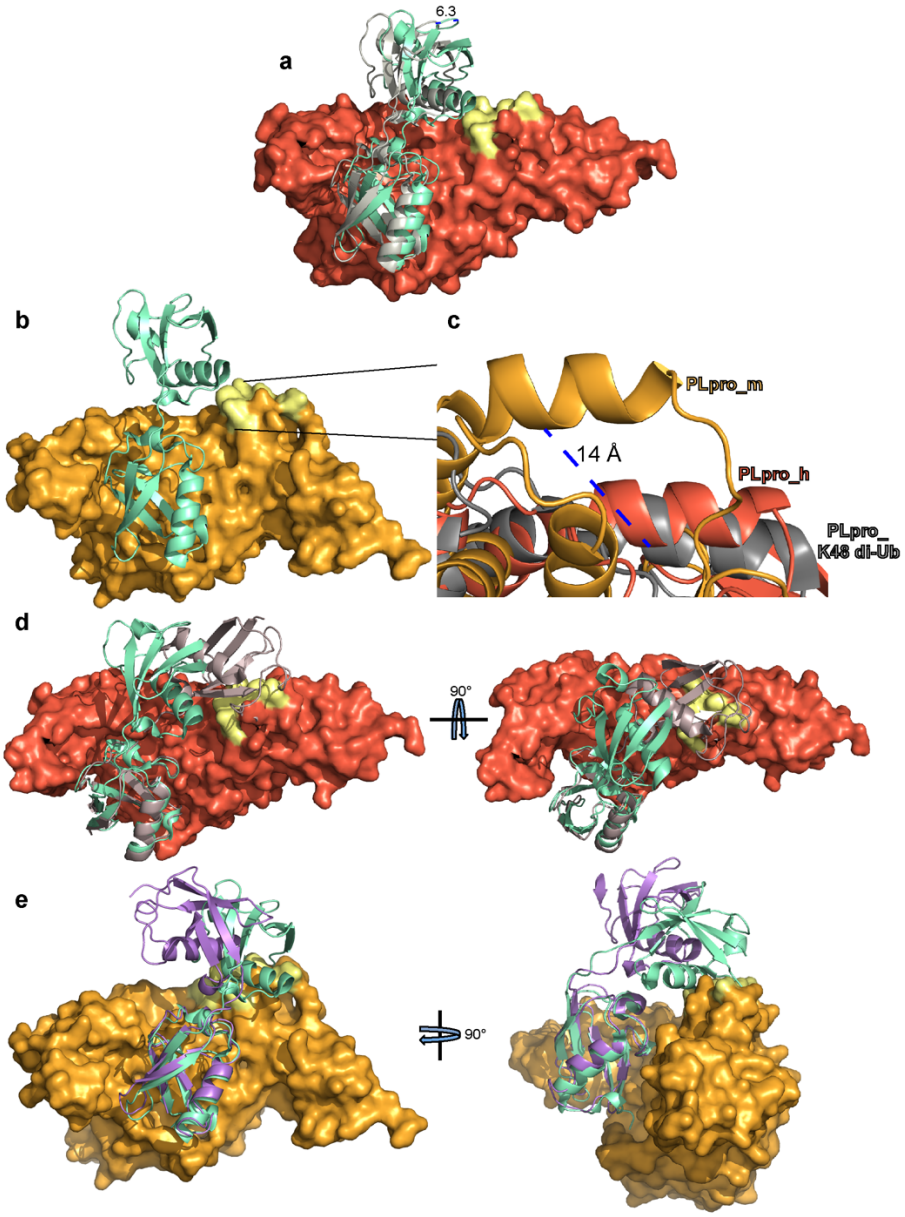

Figure 3.9 (a) SARS-CoV PLpro (reddish orange) from the ChISG15 bound structure with full-length human (green; PDB 1Z2M) overlaid with full-length human based off of a secondary

alignment using Ub (light gray; PDB 4MM3). The distance between the two-overlaid full-length human structures is measured in Å and is indicated by a blue dashed line. For all figures the highlighted yellow portion demonstrates the secondary binding site ridgeline. (b) SARS-CoV PLpro (gold) from the CmISG15 bound structure with full-length human (green; PDB 1Z2M) based off of a secondary structure alignment using ChISG15. (c) Close-up overlay of the secondary binding site helix from SARS-CoV PLpro (gold) from the CmISG15 bound structure, SARS-CoV PLpro (reddish orange) from the ChISG15 bound structure, and SARS-CoV PLpro (dark gray; PDB 5E6J) from the K48 di-Ub bound structure. The distance between the helix from SARS-CoV PLpro (gold) from the CmISG15 bound structure and the helix from SARS-CoV PLpro (reddish orange) from the ChISG15 bound structure is measured in Å and is indicated by a blue dashed line. (d) SARS-CoV PLpro (reddish orange) from the ChISG15 bound structure with full-length human (green; PDB 1Z2M) overlayed with K48 di-Ub (dark brown; PDB 5E6J) both based off of a secondary alignment using ChISG15. (e) SARS-CoV PLpro (gold) from the CmISG15 bound structure with full-length mouse overlayed with full-length human (green; PDB 1Z2M) both based off a secondary structure alignment using CmISG15.

Possible evolution of CoV PLP recognition of species variances in ISG15s

Overall, the X-ray structural, enzymatic and biophysical data point to CoV PLP deISGylase activities being sensitive to species specific amino acid differences within ISG15. Intriguingly, SARS-CoV and MERS-CoV PLpros, whose viruses replicate in a wide range of hosts, recognize and cleave proISG15 from almost all of the species tested. In contrast, the mouse specific MHV PLP2 is limited predominantly to the mouse substrate. This wider range of specificities appears substantially larger than that found recently in nairovirus vOTUs. This may imply that with the greater binding interface provided by the palm, fingers and thumb domains of the ubiquitin specific protease fold, CoV PLPs can either engage a wider array of ISG15s then that of vOTUs, or be highly selective for just one or two ISG15s as in the case of MHV.

Intriguingly, in all of the PLPs examined, their potential ability to engage different species ISG15s is not fully restricted to only those from species their parent viruses infect. Understandably, this could be a by-product in the evolutionary process of a specific viral protease seeking to optimize towards a certain species ISG15 and inadvertently picking up enzymatic

activity towards another ISG15. Or, in an environment where a virus only has to optimize its replication in one species, there is less selective pressure and hence a greater chance of losing the ability of recognizing ISG15s from other species. Alternatively, some of these types of off-species PLP activities could be indicative of evolutionary memory for ISG15s. In essence, this could give a possible view into the zoonotic evolutionary history, or potential future zoonotic drift for a certain virus. Naturally, a wider sampling of CoV PLPs affinities for certain species ISG15s, knowledge of what species their parent viruses infect, and a multitude of reverse genetics experiments will be necessary to discern which of the above scenarios in taking place in the evolution of virus recognition of host ISG15s.

Materials and Methods

Construct, Expression and Purification of PLPs for the ISG15 Protease Activity Assay and ITC

MHV PLP2 was expressed and purified as previously described [24; 33]. SARS-CoV PLpro in expression vector pET21a and MERS-CoV PLpro in pET15b were transformed into *Escherichia coli* BL21(DE3) competent cells (New England Biolabs) by heat shock. Cells were grown at 37°C in LB broth supplemented with 100 μg/mL of ampicillin to OD_{600} 0.6-0.8 and expression induced with 0.8 mM isopropyl-β-D-thiogalactopyranoside (IPTG) at 25°C overnight for SARS-CoV PLpro and 1 mM IPTG at 18°C overnight for MERS-CoV PLpro. Cells were collected by centrifugation at 6000xg for 10 minutes and stored at -80°C. Cells were lysed in Buffer A (20 mM Tris [pH 7.5 for SARS-CoV PLpro, pH 7.0 for MERS-CoV PLpro], 500 mM NaCl, 10 mM β-mercaptoethanol [BME]) supplemented with lysozyme for 30 minutes at 4°C, followed by sonication on ice at 50% power with a 50% duty cycle for a total of 6 minutes. Insoluble protein was removed by centrifugation at 70,600xg for 30 minutes and the supernatant filtered through a 0.80 μm filter. The clarified supernatant was flowed over high density nickel agarose beads (Gold

Biotechnology, Olivette, MO) pre-equilibrated with Buffer A. The column was washed with 10 column volumes of Buffer A supplemented with 30 mM imidazole, and the protein eluted with 10 column volumes of Buffer A supplemented with 300 mM imidazole. The PLpro was further purified by size exclusion chromatography using a Superdex 200 column (GE Healthcare, Pittsburgh, PA) pre-equilibrated with 100 mM NaCl, 5 mM HEPES [pH 7.5 for SARS-CoV PLpro, pH 7.0 for MERS-CoV PLpro] and 2 mM DTT.

Purification of SARS-CoV PLpro for Complexation and Crystallization

Purification of SARS-CoV PLpro in expression vector pET11a for complexing with the C-terminal domain of human ISG15 (ChISG15) and mouse ISG15 (CmISG15) was adapted from the previously described method [7]. The cells were chemically lysed by resuspending them in 150 mL of Buffer B (20 mM Tris [pH 7.5], 10 mM BME) and lysozyme and incubated at 4°C for 30 minutes. The suspension was sonicated on ice at 50% power with a 50% duty cycle for a total of 6 minutes and centrifuged for 30 minutes at 40,900xg. The cell lysate was filtered and subjected to a 40% ammonium sulfate fractionation then centrifuged again for 30 minutes at 40,900xg. The resulting pellet was resuspended in 250 mL of 1 M ammonium sulfate, 20 mM Tris [pH 7.5], and 10 mM BME and incubated at room temperature for 1 hour. The suspension was filtered and loaded onto a 50 mL Phenyl-Sepharose CL-4B column (GE Healthcare, Pittsburgh, PA) equilibrated with 1.5 M ammonium sulfate, 20 mM Tris [pH 7.5], and 10 mM BME. The protein was eluted using a 10-column-volume gradient to 100% Buffer B and washed with 2 additional column-volumes of 100% Buffer B. The fractions were pooled together and then diluted fivefold with Buffer B. The protein was loaded onto a MonoQ 10/100 column (GE Healthcare, Pittsburgh, PA) equilibrated with Buffer B. The protein was eluted using a 10-column-volume gradient to 100% of a buffer composed of 0.5M NaCl, 20 mM Tris [pH 7.5], and 10 mM BME with the initial

flow-through off the column collected. The flow through was concentrated and put into dialysis in a 50 mM NaCl, 20 mM Tris [pH 7.5], and 10 mM BME buffer at 4°C overnight.

Construct, Expression and Purification of proISG15s and mature ISG15s

ISG15s from human (*Homo sapiens*; Accession: AAH09507.1), mouse (*Mus musculus*; Accession: AAB02697.1), northern tree shrew (*Tupaia belangeri*; Accession: AFH66859.1), sheep (*Ovis aries;* Accession: AF152103.1), dromedary camel (*Camelus dromedarius*; Accession: XP_010997700.1), vesper bat (*Myotis davidii*; Accession: ELK23605.1), and jackknife fish (*Oplegnathus fasciatus*; Accession: BAJ16365.1) in both pro and mature forms were prepared as described elsewhere [23].

ISG15 Protease Activity Assay

Activity assays of SARS-CoV PLpro, MERS-CoV PLpro, and MHV PLP2 with purified northern tree shrew proISG15 (pro-nsISG15), sheep proISG15 (pro-shISG15), fish proISG15 (pro-fISG15), mouse proISG15 (pro-mISG15), camel proISG15 (pro-cISG15), bat proISG15 (pro-bISG15), and human proISG15 (pro-hISG15) were adapted from the previously described methods [23].

ITC of ISG15 with PLpros from MERS-CoV and SARS-CoV

ITC was performed using a Microcal PEAQ-ITC (Malvern, Worcestershire, UK). There were 19 injections of 2 μL each at 25°C with a reference power of 6 μcal/s. The mature forms of ISG15s along with PLpros from MERS-CoV and SARS-CoV were dialyzed at 4°C in 50 mM HEPES [pH 7.4], 200 mM NaCl, and 1 mM DTT. All experiments were run in duplicate. For direct binding experiments, 227 μM and 276 μM of SARS-CoV and MERS-CoV PLpro respectively were placed in the cell with 2.3-2.6 mM of mature hISG15 in the syringe. For competitive experiments related to SARS-CoV PLpro, mixtures containing 100 μM of protease

with 50 μM of either sheep ISG15 (shISG15), or mISG15 was placed in the cell with 1 mM of mature hISG15 in the syringe. For competitive experiments related to MERS-CoV PLpro, mixtures containing 220 μM and 270 μM of protease with 110 μM and 170 μM of shISG15 and mISG15 respectively was placed in the cell. The syringe contained 2.3 mM and 2.7 mM of mature hISG15 in the syringe for shISG15 and mISG15 assays respectively. The data were processed using Microcal PEAQ-ITC Analysis Software.

Functional studies of SARS-CoV PLpro Mutants

The SARS-CoV pET-15b-PLpro mutants (residues 1541-1855 of the SARS-CoV viral polyprotein) were generated using site-directed mutagenesis and the QuickChange® approach (Agilent). Expression and purification for the wild type and each mutant of the SARS-CoV PLpro were performed as previously described [34].

The steady-state kinetic parameters of SARS-CoV PLpro wild-type and mutants were determined for three different ubiquitin-based fluorescent substrates, utilizing 7-amino-4-methylcoumarin (AMC), commonly used to assess the protease, deubiquitinating, and deISGylating activity of PLPs, including a small peptide substrate, Z-RLRGG-AMC (Bachem), Ub-AMC (LifeSensors, Inc.), and ISG15-AMC (Boston Biochem/R&D Systems). Kinetic assays with Ub-AMC and ISG15-AMC were performed on the same day and side-by-side in the same assay plate to directly compare the enzymatic activity of SARS-CoV PLpro to that of each of the mutants. The steady-state kinetic studies were also repeated for the wild-type and mutants approximately five months apart and the resulting duplicate data were combined for analysis. Kinetic assays with the peptide substrate were also performed in triplicate. For all experiments, the assay conditions, i.e. buffering conditions and assay volume etc, were setup as previously described [24]. The exception was that the stock substrates purchased from the vendors had different

lot numbers. The steady-state kinetic data obtained from separate experiments performed on different days and with different substrates lot numbers helped to ensure that the trends in the resulting kinetic parameters were reproducible.

The enzymatic activity of PLpro-mediated hydrolysis of the fluorophore, AMC group was determined using a BioTEK Synergy H1 multimode microplate reader at 25°C with a wavelength of excitation at 360 nm (bandwidth=40 nm) and an emission wavelength of 460 nm (bandwidth=40 nm). The change in the relative fluorescence as a function of time (RFU/min) was monitored over a sufficient time period to allow determination of the enzymatic rate in the steady-state region. For the ISG15-AMC assay, the substrate concentrations were varied from 0.2 μM up to 19.2 μM. The reactions were initiated by the addition of enzyme with the final enzyme concentrations as follows: 0.48 nM WT, 0.23 nM Q233E, 0.23 nM M209A, or 7.3 nM R167E. For the Ub-AMC assay, substrate concentrations were varied from 0.5 μM to 17.6 μM. The final enzyme concentrations were 3.7 nM WT, 7.3 nM Q233E, 7.3 nM M209A, or 0.23 nM R167E. For the Z-RLRGG-AMC assay, the concentrations of substrate were varied from 0.8 μM to 50 μM and the final concentration of the wild type enzyme was 0.14 μM. To capture the initial rate of peptide hydrolysis for the M209A mutant a lower enzyme concentration of 25 nM was used. As is typical for SARS-CoV PLpro, the enzyme could not be saturated with the Ub-AMC and Z-RLRGG-AMC substrates. As such, the kinetic response of the enzyme to these substrates was linear and thus the data were fit to a line to approximate the catalytic efficiency (k_{cat}/K_m) for each enzyme. For the ISG15-AMC assays, the data were fit to the Michaelis-Menten equation to determine the associated kinetic parameters (k_{cat}, K_m, and k_{cat}/K_m) for each enzyme [24]. Saturation was not attained with the R167E mutant enzyme for ISG15-AMC and therefore this kinetic data was also fit to a line to determine the apparent (k_{cat}/K_m). The errors associated with each kinetic parameter

were obtained from the best-fit line or curves for each mutant. All data, from separate experiments, were included in the fits to arrive at the final errors (Table 1).

SARS-CoV PLpro-CmISG15 and SARS-CoV PLpro-ChISG15 Complex Formation

Expression of CmISG15, or ChISG15 occurred using a vector pTYB2 and was purified as previously described to form a propargylamine-derivatized thioester product (CmISG15-PA, ChISG15-PA) [23]. Briefly, to obtain complex, purified protease was added directly to the mixture in equi-molar ratios, and incubated for 2-4 hours at room temperature and left 4°C overnight. To further purify the complex, anion exchange chromatography was used, eluting from a MonoQ 10/100 column using a linear gradient from 0 to 1 M NaCl (SARS-CoV PLpro-CmISG15) or 250 mM NaCl (SARS-CoV PLpro-ChISG15) with 50 mM Tris (pH 8.0 for SARS-CoV PLpro-CmISG15 and pH 9.0 for SARS-CoV PLpro-ChISG15), followed by size exclusion chromatography on a Superdex 75 column (GE Healthcare, Pittsburgh, PA) pre-equilibrated with 100 mM NaCl, 5 mM HEPES [pH 7.5], and 2 mM DTT. For SARS-CoV PLpro-ChISG15, an additional purification step prior to anion exchange chromatography was used to eliminate residual ChISG15 by size exclusion chromatography using a Superdex 200 column (GE Healthcare, Pittsburgh, PA) pre-equilibrated with 100 mM NaCl, 50 mM Tris [pH 7.5], 2 mM DTT.

Crystallization of SARS-CoV PLpro-CmISG15, SARS-CoV PLpro-ChISG15, and mISG15

Purified SARS-CoV PLpro-CmISG15, SARS-CoV PLpro-ChISG15, and mISG15 were screened against a series of Qiagen NeXtal suites by hanging drop using a TTP Labtech Mosquito (TTP Labtech, Herfordshire, UK) at 8.8 mg/ml, 8.88 mg/ml, and 16 mg/ml respectively. For SARS-CoV PLpro-CmISG15, the initial screen yielded the best crystals in a solution containing 65% (vol/vol) MPD and 0.1 M Tris (pH 8.0). These crystals were optimized using the Additive HT Screen from Hampton Research. The final SARS-CoV PLpro-CmISG15 crystals were

obtained through vapor diffusion using a 500 µL reservoir with 4 µL hanging drops mixed 1:1 with protein solution and reservoir solution, which also contained 0.25 µl of 30% (w/v) Trimethylamine N-oxide dihydrate. For SARS-CoV PLpro-ChISG15, the initial screen yielded the best crystals in a solution containing 0.2 M lithium sulfate, 0.1 M Bis-Tris (pH 6.5) and 25% (w/v) PEG3350. The initial crystal conditions for SARS-CoV PLpro-ChISG15 crystals were optimized along salt and PEG3350 gradients as well as using the Additive Screen from Hampton Research. The final SARS-CoV PLpro-ChISG15 crystals were obtained through vapor diffusion using a 500 µL reservoir with 4 µL hanging drops mixed 1:1 with protein solution (6.99 mg/mL) and reservoir solution (0.1 M lithium sulfate, 0.1 M Bis-Tris, [pH 6.5], 22% PEG3350), which also contained 0.25 µl of 30% (v/v) glycerol. For mISG15, the initial screen yielded the best crystals in a solution containing 0.2 M ammonium sulfate, 0.1 M tri-sodium citrate pH 5.6, 15% (w/v) PEG4000. This condition was further optimized along buffer, pH, and PEG4000 gradients in addition to using the Additive Screen from Hampton Research. In conjunction with using these optimization methods, the mISG15 was shorted by five amino acids. The final crystals of the five amino acid shortened mISG15 were obtained through vapor diffusion using a 500 µL reservoir with 4 µL hanging drops mixed 1:1 with protein solution (6.9 mg/mL) and reservoir solution (0.2 M ammonium sulfate, 0.1 M sodium acetate pH 4.6, 12% PEG4000 and 0.2 M sodium malonate).

Crystals of SARS-CoV PLpro-CmISG15, SARS-CoV PLpro-ChISG15, and mISG15 were collected and flash frozen in liquid N_2. Cryogenic solutions for SARS-CoV PLpro-CmISG15, SARS-CoV PLpro-ChISG15 constituted their respective mother liquors. For mISG15 crystals, they were passed from a 5% to a 12% solution 1:1:1 of glycerol, dimethyl sulphoxide (DMSO), and polyethylene glycol known as EDG [35]. Data sets were collected at the Advanced Photon Source (Argonne National Labs, Argonne, IL). A data set for SARS-CoV PLpro-CmISG15 was

collected at the LS-CAT beamline 21G at a wavelength of 0.9786 Å using a MAR300 detector, whereas data sets for SARS-CoV PLpro-ChISG15 and mISG15 were collected at the SER-CAT beamlines 22ID and 22BM at 1 Å using MAR300hs detectors. All data sets were collected at 100 K.

Data Processing and Structure Solutions

Data sets were indexed, integrated and scaled using HKL-2000 [36]. All the structures were solved by molecular replacement using Phaser [37]. Subsequently, each structure was rebuilt initially using Autobuild [38] followed by successive rounds of manual model building and refinement using Coot [39] and Phenix [40]. The initial solution for the SARS-CoV PLpro-CmISG15 complex was achieved by using the catalytic core of a previous SARS-CoV PLpro structure (PDB entry 3E9S). Density from the last 10 amino acids of the CmISG15 molecule served as an anchor for the initial global placement of the CmISG15 from a Erve nairovirus vOTU-CmISG15 complex (PDB entry 5JZE). This partial model was then used as a search model along with the Ub-like SARS-CoV PLpro domain from PDB entry 4MM3 to obtain a complete global model using Phaser [37]. For the SARS-CoV PLpro-ChISG15 complex, an initial molecular replacement solution was obtained by using the core and other elements from the SARS-CoV PLpro-CmISG15 as a search model. A partial molecular replacement solution using Phaser [37] for mISG15 was obtained by searching with the CmISG15 from the Erve nairovirus vOTU-CmISG15 complex structure (PDB entry 5JZE). This partial model was used in a sequential Phaser [37] run using a mISG15 N-terminal domain homology model based on the previously solved hISG15 structure (PDB entry 1Z2M). All structures were validated using Molprobity [41] and have good Ramachandran statistics: SARS-CoV PLpro-CmISG15 (96% favored and 4% allowed), SARS-CoV PLpro-ChISG15 (96% favored and

4% allowed) and mISG15 (99.08% favored and 0.92% allowed). All structures have been deposited in the protein data bank. Codes can be found on Table 3.

Electropotential plots

Figure renderings involving electropotential plots were performed using the PDB2PQR server and the surface generated using the adaptive Poisson-Boltzmann solver (APBS) [42].

References

1. Perlman, S. & Netland, J. (2009). Coronaviruses post-SARS: update on replication and pathogenesis. *Nat Rev Microbiol* **7**, 439-50.
2. Hilgenfeld, R. & Peiris, M. (2013). From SARS to MERS: 10 years of research on highly pathogenic human coronaviruses. *Antiviral Research* **100**, 286-295.
3. (2015). Middle East respiratory syndrome coronavirus (MERS-CoV) - Saudi Arabia. WHO.
4. Korea Centers for Disease, C. & Prevention. (2015). Middle East Respiratory Syndrome Coronavirus Outbreak in the Republic of Korea, 2015. *Osong Public Health and Research Perspectives* **6**, 269-278.
5. WHO. (2016). Middle East respiratory syndrome coronavirus (MERS-CoV) - Saudi Arabia. World Health Organization.
6. Thiel, V., Ivanov, K. A., Putics, Á., Hertzig, T., Schelle, B., Bayer, S., Weißbrich, B., Snijder, E. J., Rabenau, H., Doerr, H. W., Gorbalenya, A. E. & Ziebuhr, J. (2003). Mechanisms and enzymes involved in SARS coronavirus genome expression. *Journal of General Virology* **84**, 2305-2315.
7. Barretto, N., Jukneliene, D., Ratia, K., Chen, Z., Mesecar, A. D. & Baker, S. C. (2005). The papain-like protease of severe acute respiratory syndrome coronavirus has deubiquitinating activity. *J Virol* **79**, 15189-98.
8. Ratia, K., Saikatendu, K. S., Santarsiero, B. D., Barretto, N., Baker, S. C., Stevens, R. C. & Mesecar, A. D. (2006). Severe acute respiratory syndrome coronavirus papain-like protease:

Structure of a viral deubiquitinating enzyme. *Proceedings of the National Academy of Sciences* **103**, 5717-5722.

9. Harcourt, B. H., Jukneliene, D., Kanjanahaluethai, A., Bechill, J., Severson, K. M., Smith, C. M., Rota, P. A. & Baker, S. C. (2004). Identification of Severe Acute Respiratory Syndrome Coronavirus Replicase Products and Characterization of Papain-Like Protease Activity. *Journal of Virology* **78**, 13600-13612.

10. Mielech, A. M., Deng, X., Chen, Y., Kindler, E., Wheeler, D. L., Mesecar, A. D., Thiel, V., Perlman, S. & Baker, S. C. (2015). Murine Coronavirus Ubiquitin-Like Domain Is Important for Papain-Like Protease Stability and Viral Pathogenesis. *Journal of Virology* **89**, 4907-4917.

11. Lindner, H. A., Lytvyn, V., Qi, H., Lachance, P., Ziomek, E. & Ménard, R. (2007). Selectivity in ISG15 and ubiquitin recognition by the SARS coronavirus papain-like protease. *Archives of Biochemistry and Biophysics* **466**, 8-14.

12. Devaraj, S. G., Wang, N., Chen, Z., Chen, Z., Tseng, M., Barretto, N., Lin, R., Peters, C. J., Tseng, C.-T. K., Baker, S. C. & Li, K. (2007). Regulation of IRF-3-dependent Innate Immunity by the Papain-like Protease Domain of the Severe Acute Respiratory Syndrome Coronavirus. *Journal of Biological Chemistry* **282**, 32208-32221.

13. Frieman, M., Ratia, K., Johnston, R. E., Mesecar, A. D. & Baric, R. S. (2009). Severe acute respiratory syndrome coronavirus papain-like protease ubiquitin-like domain and catalytic domain regulate antagonism of IRF3 and NF-kappaB signaling. *J Virol* **83**, 6689-705.

14. Bailey-Elkin, B. A., Knaap, R. C., Johnson, G. G., Dalebout, T. J., Ninaber, D. K., van Kasteren, P. B., Bredenbeek, P. J., Snijder, E. J., Kikkert, M. & Mark, B. L. (2014). Crystal structure of the Middle East respiratory syndrome coronavirus (MERS-CoV) papain-like protease bound to ubiquitin facilitates targeted disruption of deubiquitinating activity to demonstrate its role in innate immune suppression. *J Biol Chem* **289**, 34667-82.

15. Ratia, K., Kilianski, A., Baez-Santos, Y. M., Baker, S. C. & Mesecar, A. (2014). Structural Basis for the Ubiquitin-Linkage Specificity and deISGylating Activity of SARS-CoV Papain-Like Protease. *PLoS Pathog* **10**, e1004113.

16. Békés, M., van der Heden van Noort, Gerbrand J., Ekkebus, R., Ovaa, H., Huang, Tony T. & Lima, Christopher D. (2016). Recognition of Lys48-Linked Di-ubiquitin and Deubiquitinating Activities of the SARS Coronavirus Papain-like Protease. *Molecular Cell* **62**, 572-585.

17. Zaki, A. M., van Boheemen, S., Bestebroer, T. M., Osterhaus, A. D. M. E. & Fouchier, R. A. M. (2012). Isolation of a Novel Coronavirus from a Man with Pneumonia in Saudi Arabia. *New England Journal of Medicine* **367**, 1814-1820.

18. Tsoleridis, T., Onianwa, O., Horncastle, E., Dayman, E., Zhu, M., Danjittrong, T., Wachtl, M., Behnke, J. M., Chapman, S., Strong, V., Dobbs, P., Ball, J. K., Tarlinton, R. E. & McClure, C. P. (2016). Discovery of Novel Alphacoronaviruses in European Rodents and Shrews. *Viruses* **8**, 84.

19. Compton, S. R., Stephensen, C. B., Snyder, S. W., Weismiller, D. G. & Holmes, K. V. (1992). Coronavirus species specificity: murine coronavirus binds to a mouse-specific epitope on its carcinoembryonic antigen-related receptor glycoprotein. *Journal of Virology* **66**, 7420-7428.

20. Sridharan, H., Zhao, C. & Krug, R. M. (2010). Species specificity of the NS1 protein of influenza B virus: NS1 binds only human and non-human primate ubiquitin-like ISG15 proteins. *J Biol Chem* **285**, 7852-6.

21. Lai, C., Struckhoff, J. J., Schneider, J., Martinez-Sobrido, L., Wolff, T., Garcia-Sastre, A., Zhang, D. E. & Lenschow, D. J. (2009). Mice lacking the ISG15 E1 enzyme UbE1L demonstrate increased susceptibility to both mouse-adapted and non-mouse-adapted influenza B virus infection. *J Virol* **83**, 1147-51.

22. Versteeg, G. A. & García-Sastre, A. (2010). Viral tricks to grid-lock the type I interferon system. *Current Opinion in Microbiology* **13**, 508-516.

23. Deaton, M. K., Dzimianski, J. V., Daczkowski, C. M., Whitney, G. K., Mank, N. J., Parham, M. M., Bergeron, E. & Pegan, S. D. (2016). Biochemical and Structural Insights into the Preference

of Nairoviral DeISGylases for Interferon-Stimulated Gene Product 15 Originating from Certain Species. *Journal of Virology* **90**, 8314-8327.

24. Baez-Santos, Y. M., Mielech, A. M., Deng, X., Baker, S. & Mesecar, A. D. (2014). Catalytic function and substrate specificity of the papain-like protease domain of nsp3 from the Middle East respiratory syndrome coronavirus. *J Virol* **88**, 12511-27.

25. Ma, X. Z., Bartczak, A., Zhang, J., He, W., Shalev, I., Smil, D., Chen, L., Phillips, J., Feld, J. J., Selzner, N., Levy, G. & McGilvray, I. (2014). Protein interferon-stimulated gene 15 conjugation delays but does not overcome coronavirus proliferation in a model of fulminant hepatitis. *J Virol* **88**, 6195-204.

26. Deng, X., Agnihothram, S., Mielech, A. M., Nichols, D. B., Wilson, M. W., StJohn, S. E., Larsen, S. D., Mesecar, A. D., Lenschow, D. J., Baric, R. S. & Baker, S. C. (2014). A chimeric virus-mouse model system for evaluating the function and inhibition of papain-like proteases of emerging coronaviruses. *J Virol* **88**, 11825-33.

27. Akutsu, M., Ye, Y., Virdee, S., Chin, J. W. & Komander, D. (2011). Molecular basis for ubiquitin and ISG15 cross-reactivity in viral ovarian tumor domains. *Proceedings of the National Academy of Sciences* **108**, 2228-2233.

28. James, T. W., Frias-Staheli, N., Bacik, J.-P., Levingston Macleod, J. M., Khajehpour, M., García-Sastre, A. & Mark, B. L. (2011). Structural basis for the removal of ubiquitin and interferon-stimulated gene 15 by a viral ovarian tumor domain-containing protease. *Proceedings of the National Academy of Sciences* **108**, 2222-2227.

29. Narasimhan, J., Wang, M., Fu, Z., Klein, J. M., Haas, A. L. & Kim, J.-J. P. (2005). Crystal Structure of the Interferon-induced Ubiquitin-like Protein ISG15. *Journal of Biological Chemistry* **280**, 27356-27365.

30. Guan, R., Ma, L.-C., Leonard, P. G., Amer, B. R., Sridharan, H., Zhao, C., Krug, R. M. & Montelione, G. T. (2011). Structural basis for the sequence-specific recognition of human ISG15

by the NS1 protein of influenza B virus. *Proceedings of the National Academy of Sciences* **108**, 13468-13473.

31. Zhao, C., Beaudenon, S. L., Kelley, M. L., Waddell, M. B., Yuan, W., Schulman, B. A., Huibregtse, J. M. & Krug, R. M. (2004). The UbcH8 ubiquitin E2 enzyme is also the E2 enzyme for ISG15, an IFN-alpha/beta-induced ubiquitin-like protein. *Proc Natl Acad Sci U S A* **101**, 7578-82.

32. Speer, S. D., Li, Z., Buta, S., Payelle-Brogard, B., Qian, L., Vigant, F., Rubino, E., Gardner, T. J., Wedeking, T., Hermann, M., Duehr, J., Sanal, O., Tezcan, I., Mansouri, N., Tabarsi, P., Mansouri, D., Francois-Newton, V., Daussy, C. F., Rodriguez, M. R., Lenschow, D. J., Freiberg, A. N., Tortorella, D., Piehler, J., Lee, B., García-Sastre, A., Pellegrini, S. & Bogunovic, D. (2016). ISG15 deficiency and increased viral resistance in humans but not mice. *Nature Communications* **7**, 11496.

33. Mielech, A. M., Deng, X., Chen, Y., Kindler, E., Wheeler, D. L., Mesecar, A. D., Thiel, V., Perlman, S. & Baker, S. C. (2015). Murine coronavirus ubiquitin-like domain is important for papain-like protease stability and viral pathogenesis. *J Virol* **89**, 4907-17.

34. Baez-Santos, Y. M., Barraza, S. J., Wilson, M. W., Agius, M. P., Mielech, A. M., Davis, N. M., Baker, S. C., Larsen, S. D. & Mesecar, A. D. (2014). X-ray structural and biological evaluation of a series of potent and highly selective inhibitors of human coronavirus papain-like proteases. *J Med Chem* **57**, 2393-412.

35. Sanchez, J. E., Gross, P. G., Goetze, R. W., Walsh, R. M., Peeples, W. B. & Wood, Z. A. (2015). Evidence of Kinetic Cooperativity in Dimeric Ketopantoate Reductase from Staphylococcus aureus. *Biochemistry* **54**, 3360-3369.

36. Otwinowski, Z. & Minor, W. (1997). Processing of X-ray diffraction data collected in oscillation mode. In *Methods in Enzymology* (Charles W. Carter, Jr., ed.), Vol. Volume 276, pp. 307-326. Academic Press.

37. McCoy, A. J., Grosse-Kunstleve, R. W., Adams, P. D., Winn, M. D., Storoni, L. C. & Read, R. J. (2007). Phaser crystallographic software. *Journal of Applied Crystallography* **40**, 658-674.

38. Terwilliger, T. C., Grosse-Kunstleve, R. W., Afonine, P. V., Moriarty, N. W., Zwart, P. H., Hung, L.-W., Read, R. J. & Adams, P. D. (2008). Iterative model building, structure refinement and density modification with the PHENIX AutoBuild wizard. *Acta Crystallographica Section D* **64**, 61-69.

39. Emsley, P. & Cowtan, K. (2004). Coot: model-building tools for molecular graphics. *Acta Crystallographica Section D* **60**, 2126-2132.

40. Adams, P. D., Afonine, P. V., Bunkoczi, G., Chen, V. B., Davis, I. W., Echols, N., Headd, J. J., Hung, L.-W., Kapral, G. J., Grosse-Kunstleve, R. W., McCoy, A. J., Moriarty, N. W., Oeffner, R., Read, R. J., Richardson, D. C., Richardson, J. S., Terwilliger, T. C. & Zwart, P. H. (2010). PHENIX: a comprehensive Python-based system for macromolecular structure solution. *Acta Crystallographica Section D* **66**, 213-221.

41. Chen, V. B., Arendall, W. B., III, Headd, J. J., Keedy, D. A., Immormino, R. M., Kapral, G. J., Murray, L. W., Richardson, J. S. & Richardson, D. C. (2010). MolProbity: all-atom structure validation for macromolecular crystallography. *Acta Crystallographica Section D* **66**, 12-21.

42. Dolinsky, T. J., Nielsen, J. E., McCammon, J. A. & Baker, N. A. (2004). PDB2PQR: an automated pipeline for the setup of Poisson-Boltzmann electrostatics calculations. *Nucleic Acids Res* **32**, W665-7.

CHAPTER 4

STRUCTUALLY GUIDED REMOVAL OF DEISGYLASE BIOCHEMICAL ACTIVITY FROM PAPAIN-LIKE PROTEASE ORIGINATING FROM THE MIDDLE EAST RESPIRATORY SYNDROME VIRUS[1]

[1]Daczkowski, C.M., O. Goodwin, J.V. Dzimianski, J.J. Farhat, and S.D. Pegan. 2017. *Journal of Virology*. 91(23): 1067-17.

Reprinted here with permission of publisher

Abstract

Middle East respiratory syndrome coronavirus (MERS-CoV) is an emerging human pathogen that is the causative agent for Middle East respiratory syndrome (MERS). With MERS outbreaks resulting in over 35% fatalities and now spread to 27 countries, MERS-CoV poses a significant on-going threat to global human health. As part of its viral genome, MERS-CoV encodes for a papain-like protease (PLpro) that has been observed to act as a deubiquitinase and deISGylase to antagonize IFN-I immune pathways. This activity is in addition to its viral polypeptide cleavage function. Although the overall impact of MERS-CoV PLpro function is observed to be essential, difficulty has been encountered in delineating the importance of its separate functions, particularly its deISGylase activity. As a result, the interface of MERS-CoV and human interferon stimulated gene product 15 (hISG15) was probed with isothermal calorimetry suggesting the C-terminal domain of hISG15 to be principally responsible for interactions. Subsequently, the structure of MERS-CoV PLpro was solved to 2.4 Å in complex with the C-terminal domain of hISG15. Utilizing this structural information, mutants were generated that lacked appreciable deISGylase activity but retained wild-type deubiquitinase and peptide cleavage activities. Hence, this provides a new platform for understanding viral deISGylase activity within MERS-CoV and other CoVs.

Importance

Coronaviruses, such as Middle East respiratory syndrome coronavirus (MERS-CoV), encode a papain-like protease (PLpro) that possesses the ability to antagonize interferon immune pathways through the removal of ubiquitin and interferon-stimulated gene product 15 (ISG15) from target proteins. The lack of CoV proteases with attenuated deISGylase activity has been a key obstacle in delineating the impact between deubiquitinase and deISGylase activities on viral host evasion and pathogenesis. Here, biophysical techniques revealed that MERS-CoV PLpro chiefly engages human ISG15 occurs through its C-terminal domain. The first structure of MERS-CoV PLpro in complex with this domain exposed the interface between these two entities. Employing these structural insights, mutations were employed to selectively remove deISGylase activity with no appreciable impact to its other deubiquitinase and peptide cleavage biochemical properties. Excitingly, this study introduces a new tool to probe pathogenesis of MERS-CoV and related viruses through the removal of viral deISGylase activity.

Introduction

Middle East respiratory syndrome (MERS) is a devastating human disease involving more than 1,700 cases spanning 27 different countries with an overall case fatality rate of just over 35% (1). The causative agent for MERS, MERS coronavirus (MERS-CoV), is an enveloped, positive-sense single stranded RNA (ssRNA) virus classified as belonging to the *Betacoronavirus* genus of the Coronaviridae family. MERS-CoV was first isolated in 2012 from a 60-year-old man originating from Saudi Arabia who suffered from respiratory symptoms and later died from severe progressive respiratory and renal failure (2). Shortly thereafter additional MERS-CoV cases were observed originating from infected dromedary camels as well as human-human transmission (3, 4). Due to the resemblance and severity in the symptoms brought on by infection, proven human-

human transmission, as well as its zoonotic nature, MERS-CoV is often compared to severe acute respiratory syndrome coronavirus (SARS-CoV) (4). With SARS-CoV causing a pandemic with more than 8,000 cases (~10% case-fatality rate) in 2003, there is considerable concern about a potential, similar MERS-CoV outbreak (5, 6). As a result, MERS-CoV is currently seen as an emerging global human health threat.

As with other positive stranded RNA viruses, coronaviruses encode long viral polyprotein containing 16 different nonstructural proteins (Nsps 1-16) that are cleaved by viral encoded proteases (7-9). For coronaviruses in general, they encode one 3C-like protease, also known as the main protease, as well as up to two papain-like proteases (PLPs). In the case of MERS-CoV, only one PLP is encoded, PLpro. The MERS-CoV PLpro and 3C-like protease are responsible for cleaving Nsps 1-3 and 4-16 respectively in order to generate the membrane-bound replicase complex necessary for RNA replication (8, 10). Intriguingly, CoV PLpros have been observed to have additional roles beyond simply cleaving Nsps 1-3 to promote viral replication (11).

Similar to SARS-CoV PLpro and some other CoV PLPs, MERS-CoV PLpro possesses the ability to reverse post-translational modifications by ubiquitin (Ub) and interferon-stimulated gene product 15 (ISG15; Figure 4.1) (12). Ubiquitination and ISGylation of viral and host proteins has been observed to play essential roles in several immune pathways to include the IFN-I, which is often viewed as the first line of defense against viral infection (13, 14). This includes the production and release of IFNs within the IFN-I response as well as the NFκB inflammation response (15). Additionally, these post-translational modifications are central to the increased production of chemokines and cytokines as well as other IFN-stimulated gene products with antipathogenic properties (15, 16). In line with the importance of ubiquitination and ISGylation in host immunity, the dual deubiquitinase and deISGylase activities of the SARS-CoV PLpro were

observed to antagonize the IFN-I response and was suggested to be a key viral evasion mechanism (15, 16). This was further supported by the diminishment of deubiquitinase and deISGylase activity in Mouse hepatitis coronavirus' (MHV) PLpro equivalent through use of a destabilizing mutation (10). Also, direct disruption of MERS-CoV PLpro's deubiquitinase and deISGylase proteolytic activity together was shown to remove antagonism of IFN-I response in part due to suppression of Ub-dependent mitochondrial antiviral-signaling protein (MAVS)-mediated signaling (17).

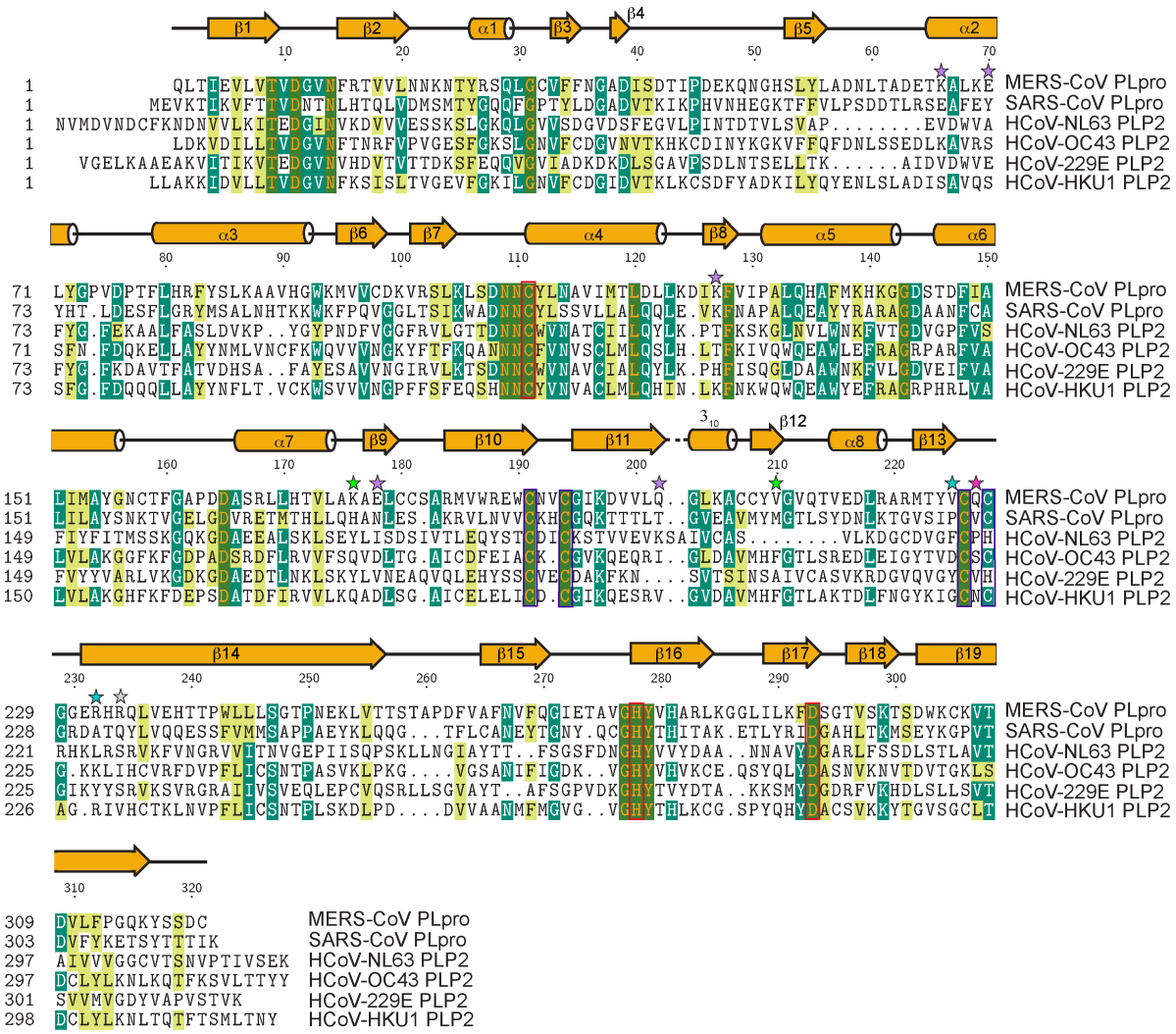

Figure 4.1. Sequence alignment of PLpros and PLP2s from coronaviruses. The PLpro or PLP2 from MERS-CoV (accession number AFS88944), SARS-CoV (accession number P0C6U8),

HCoV-NL63 (accession number YP_003766), HCoV-OC43 (accession number AMK59674), HCoV-229E (accession number APT69896), and HCoV-HKU1 (accession number ARB07606). The residue numbering ruler is based on MERS-CoV PLpro. The secondary structure predicted by DSSP is shown for MERS-CoV PLpro. Residues that form the catalytic triad are boxed in red, while residues forming the zinc finger motif are boxed in purple. The residues mutated in this study are denoted by stars, which are coloured based on the enzymatic activity results.

Regrettably, as pointed out by the authors in the latter study, a lack of structural information pertaining to how MERS-CoV PLpro accommodates ISG15s limited their ability to delineate whether the MERS-CoV PLpro's deubiquitinase, deISGylase, or both activities were critical for effective IFN-I antagonism by MERS-CoV, or other CoV PLPs (17). To date several structures of MERS-CoV PLpro bound to Ub have been solved illuminating the specific amino acid residues involved in ubiquitin binding (17, 18). However, no structures illuminating the interface of MERS-CoV and ISG15s has similarly been elucidated. Some structural information on the interactions between a CoV PLpros and ISG15 has recently become available through the structures of SARS-CoV PLpro in complex with the C-terminal domain from two species ISG15s (19). This study highlighted significant differences in how SARS-CoV PLpro accommodated not only ubiquitin differently than human ISG15, but also how the accommodation of ISG15s from different species could differ. However, it also demonstrated that the thermodynamic factors governing MERS-CoV engagement of human ISG15 differ from that of SARS-CoV PLpro (Table 4.1)(19). Additionally, MERS-CoV preferred a different subset of species ISG15 suggesting that mutations that may shift, or limit certain deubiquitinase and species-specific deISGylase activities in SARS-CoV PLpro may not be directly translatable to MERS-CoV PLpro (19).

Table 4.1. Isothermal Titration Calorimetry of human ISG15 and Mono-Ub binding to CoV PLpros.

Protein	N[a] (sites)	K_D (μM)	ΔH[b] (kJ/mol)	ΔG[c] (kJ/mol)	-TΔS[d] (kJ/mol)
MERS-CoV PLpro					
Human ISG15[e]	0.785 ± 0.027	59.30 ± 12.7	-11.34 ± 0.268	-24.15	-12.80
C-Human ISG15[f]	0.721 ± 0.025	27.06 ± 3.04	-15.22 ± 0.521	-26.08	-10.87
Mono-Ub[f]	0.692 ± 0.011	9.56 ± 0.233	-21.20 ± 0.141	-6.85	14.30
SARS-CoV PLpro					
Human ISG15[e]	0.932 ± 0.032	20.50 ± 4.48	-27.20 ± 1.90	-26.80	0.38
C-Human ISG15[e]	1.31 ± 0.015	57.60 ± 3.21	-4.03 ± .019	-24.18	-20.17
MERS-CoV PLpro K176E					
Human ISG15	-	>50 mM	-	-	-
Mono-Ub[f]	0.655 ± .036	7.41 ± .643	-19.90 ± 0.00	-7.00	12.9
MERS-CoV PLpro V210D					
Human ISG15	-	>50 mM	-	-	-
Mono-Ub[f]	0.708 ± .0041	200.50 ± 7.77	-16.00 ± .566	-5.045	10.95

[a] Binding stoichiometry. [b] Binding enthalpy. [c] Gibb's free energy. [d] Entropy factor.
[e] Data taken from Daczkowski et al., 2017
[f] Average with error calculated using standard deviation

To address these issues, we determined through isothermal titration calorimetry (ITC) and mutational data that MERS-CoV PLpro principally engages human ISG15 through its C-terminal domain. Additionally, we solved the crystal structure of the MERS-CoV PLpro in complex with the C-terminal domain of human ISG15 (ChISG15). Leveraging this structural information, amino acid sites within the MERS-CoV and hISG15 interface were probed to gain insight into the explicit interactions driving the ISG15 – MERS-CoV PLpro binding event. This has resulted in the generation of altered MERS-CoV PLpros lacking appreciable biochemical deISGylase activity while still retaining wild-type deubiquitinase and peptide catalytic activities.

Results and Discussion

MERS-CoV PLpro's affinity for hISG15

MERS-CoV PLpro as well as other PLPs originating from CoVs have widely been observed to possess a dual role in promoting viral replication through the processing of the viral

polypeptide and the removal of post-translational modifications of Ub and ISG15 (7-9, 11). For the former, the viral polypeptide cleavage activity appears to be largely dependent on the protease's ability to cleave the peptide bond after the LXGG recognition sequence found throughout the polypeptide (7, 9, 20). This differs for Ub and ISG15 where these proteases not only recognize a conserved LRLRGG sequence but also have been suggested to engage other tertiary elements of Ub and ISG15 (12, 17, 18). Recently, ITC data, as well as other mutational data, supported that this interaction extends to the N-terminal domain of ISG15 for SARS CoV PLpro (19, 20). Specifically, the C-terminal domain of hISG15 (ChISG15) was found to have weaker affinity and a different thermodynamic profile that differed from full-length hISG15 supporting a role of the N-terminal domain in shaping the interactions between ISG15s and SARS CoV PLpro (12, 19).

To assess whether the presence of the N-terminal domain of hISG15 had a similar influence on hISG15 binding to MERS CoV PLpro, the affinity of MERS-CoV PLpro for ChISG15 was assessed utilizing ITC. The dissociation constant (K_D) for ChISG15 and MERS-CoV was 27.06 ± 3.04 μM, which was weaker when compared to mono-Ub (K_D = 9.56 ± 0.233 μM), but slightly tighter binding compared to the previously published ITC data pertaining to the full-length (K_D = 59.3 ± 4.5 μM) (Table 4.1 and Figure 4.2). Surprisingly, the overall thermodynamics driving the interaction of the ChISG15 and the protease were strikingly similar to that of full-length ISG15. Specifically, like hISG15, ChISG15 binding event was driven by a combination of favorable entropic and enthalpic components with similar ratios. This was orthogonal to the striking thermodynamic differences previously observed between SARS-CoV PLpro's interactions with hISG15 and ChISG15. Naturally, the full-length hISG15 could bind to MERS-CoV PLpro in a manner were the entropic and enthalpic contributions of the N-terminus are masked by offsets in

other interactions. However, a simpler explanation may be that the N-terminal domain of hISG15 does not play as significant a role for MERS-CoV PLpro as it does for SAR-CoV PLpro. The latter would also imply the C-terminal domain of hISG15 plays the dominant role in forming favorable interactions with MERS CoV PLpro.

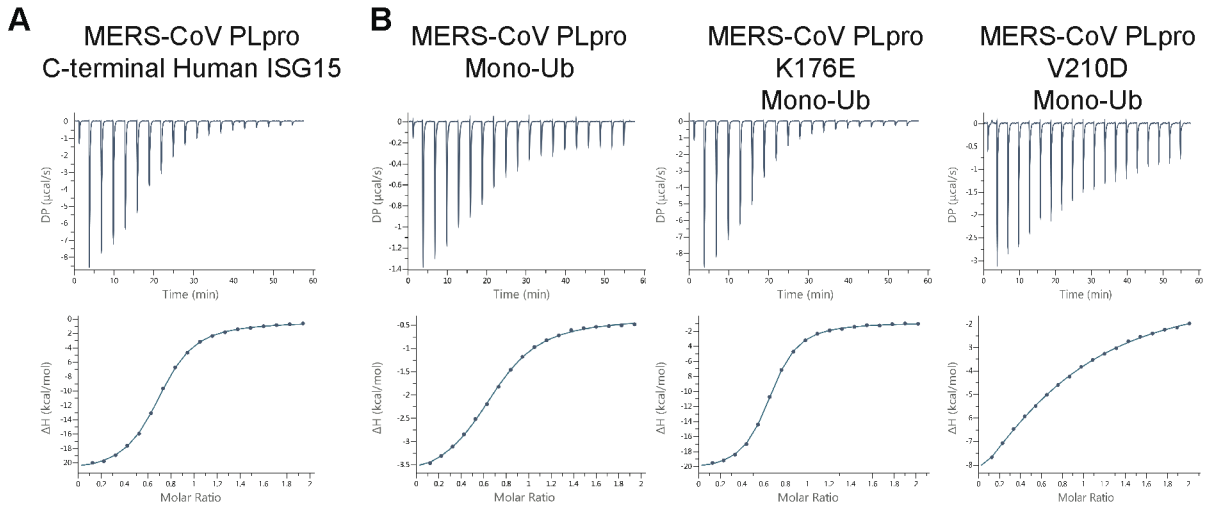

Figure 4.2. Isothermal titration calorimetry. (A) ITC binding isotherm with the raw heat (top panel) and integrated heats of injection (bottom panel) shown for the interaction between MERS-CoV PLpro and ChISG15. (B) ITC binding isotherm with the raw heat (top panel) and integrated heats of injection (bottom panel) shown for the interaction between MERS-CoV PLpro and MERS-CoV PLpro mutants, K176E and V210D, and mono-Ub.

Binding interface of MERS-CoV PLpro and ChISG15

To reveal key interactions with the C-terminal domain of hISG15 with MERS-CoV PLpro, the X-ray structure of the MERS-CoV PLpro – ChISG15 complex was initially determined to 2.7 Å in the $P4_3$ space group by collecting on the zinc absorption edge and utilizing SAD. This structure was used as a search model to perform molecular replacement into a higher resolution native data set. The subsequent 2.4 Å structure was found to possess two copies of the MERS-CoV PLpro – ChISG15 complex within the asymmetric unit (Table 4.2). Within each complex, density for the protease's Ub-like domain, palm, thumb, and zinc bound finger domains were

present. In addition, the Ub-like fold of ChISG15 was found in close proximity with the fingers and palm domains of MERS-CoV PLpro (Figure 4.3).

Table 4.2. Data collection and refinement statistics for MERS-CoV PLpro-ChISG15

	Zn-SAD (PDB entry 5W8T)	Native (PDB entry 5W8U)
Data collection		
Space group	$P4_3$	$P4_3$
Wavelength (Å)	1.2837	1
Cell dimensions		
a, *b*, *c* (Å)	86.3, 86.3, 223.6	86.4, 86.4, 224.1
α, β, γ (°)	90, 90, 90	90, 90, 90
Resolution (Å)	50.00-2.76 (2.81-2.76)†	50.00-2.41 (2.45-2.41)†
R_{merge}	0.090 (0.922)	0.062 (0.766)
$CC_{1/2}$	0.999 (0.838)	0.998 (0.728)
$I / \sigma I$	24.1 (1.5)	31.6 (1.49)
Completeness (%)	99.73 (99.59)	99.45 (98.59)
Redundancy	8.5 (7.8)	4.9 (3.5)
Phasing statistics		
No. of Zn sites found	7	
Phasing figure of merit	0.279	
Refinement		
Resolution (Å)	41.23-2.76 (2.86-2.76)	38.63-2.41 (2.45-2.41)
No. reflections	41,870	62,588
R_{work} (%)/ R_{free} (%)	18.8/22.4	21.3/23.7
No. atoms		
Protein	6200	6216
Ligand/ion‡	62	78
Water	31	161
B-factors		
Protein	84.42	67.43
Ligand/ion‡	94.42	68.37
Water	62.77	63.37
R.m.s. deviations		
Bond lengths (Å)	0.006	0.004
Bond angles (°)	0.80	0.62

†Values in parentheses denote the highest resolution shell
‡Includes the propargyl linker, MPD from the crystallization condition, and Zn

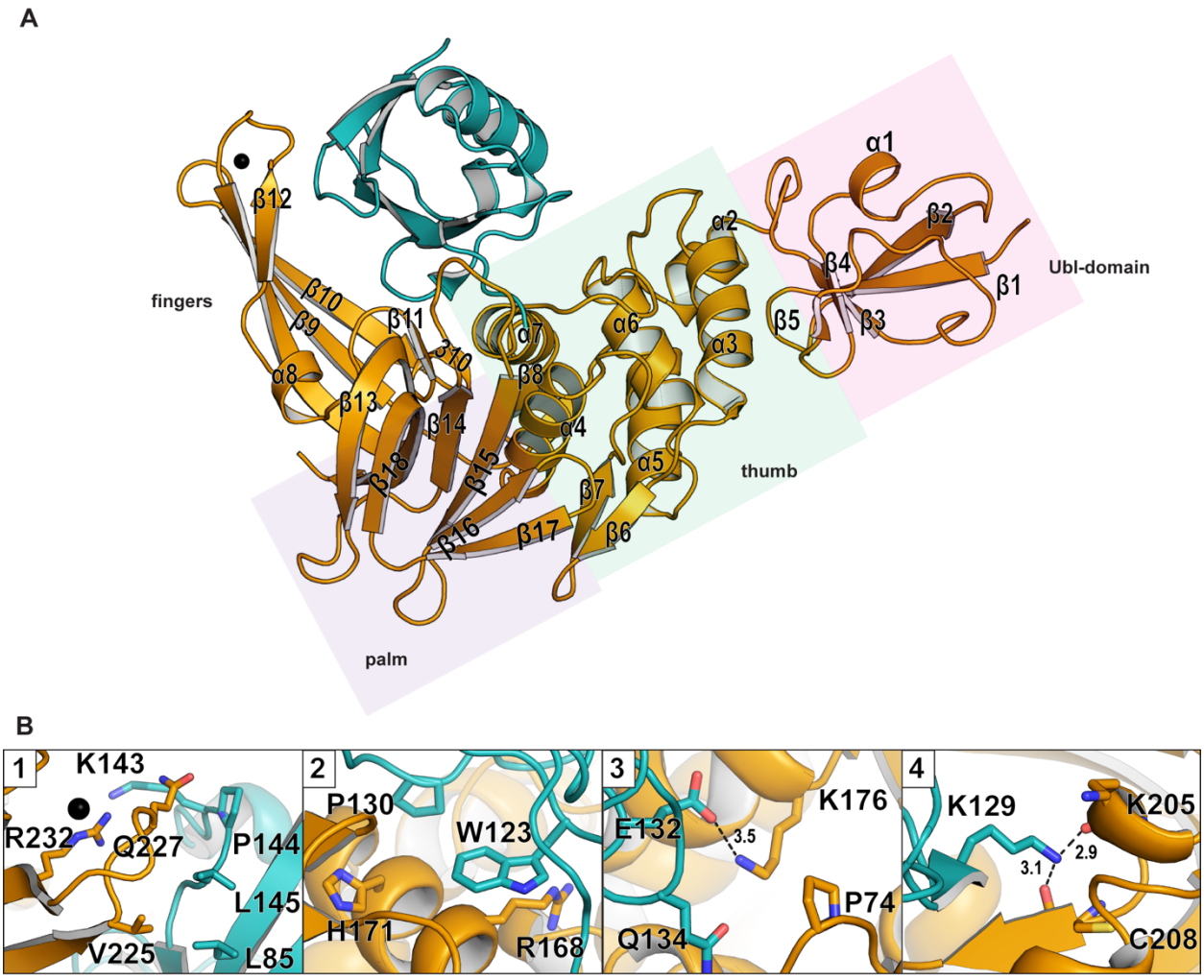

Figure 4.3. Structure of MERS-CoV PLpro bound to ChISG15. (A) Cartoon rendering of the MERS-CoV PLpro bound to ChISG15. The PLpro is shown in gold, with ChISG15 colored teal. The structural domains of MERS-CoV PLpro consist of the fingers (white), palm (lavender), thumb (green), and Ubl-domain (pink). (B) Interactions at the interface between PLpro and ChISG15 colored as in (A). Hydrogen bonds are represented with black dashed lines with distances labeled in black.

Examination of the MERS-CoV PLpro – ChISG15 binding interface revealed a mix of hydrophobic and electrostatic interactions that appears reflective of favorable entropic and enthalpic thermodynamic forces observed by ITC. Specifically, the MERS-CoV PLpro – ChISG15 structure revealed two sets of hydrophobic interactions. The most extensive of these

hydrophobic interactions is generated by the accommodation of Leu85 and Pro144 along with the alkyl part of Lys143 and Leu145 sidechains of the ChISG15 interacting with a hydrophobic seam running along the fingers domain and Zn binding site of MERS-CoV PLpro. Specifically, this seam on the protease includes Val225 as well as the alkyl parts of the sidechains belonging to Gln227, and Arg232 (Figure 4.3B; panel 1). In addition, a smaller hydrophobic pocket, within the thumb and palm domains of the protease, is made up of interactions between His171 and Arg168 of the MERS-CoV PLpro and ChISG15 residues Pro130 and Trp123 (Figure 4.3B; panel 2). Beyond hydrophobic interactions, two principle sets of electrostatic interactions are observed. One of these interactions are made via H-bonds between Glu132 and Lys176 of the ChISG15 and MERS-CoV PLpro respectively (Figure 4.3B; panel 3). The other is comprised of the insertion of ChISG15's Lys129 sidechain into a pocket generated by the carbonyl groups of the PLpro's Lys205 and Cys208 (Figure 4.3B; panel 4). Overall, the mix of interactions appears to mirror the favorable entropic and enthalpic thermodynamic forces observed when the ISG15 product binds to the protease via ITC.

Differences in the accommodation of ChISG15 and Ub by CoV PLpros

Comparison of the MERS-CoV PLpro's accommodation of ChISG15 within its Ub binding motif (UIM) to that of Ub highlights the likely dynamic nature of PLpros' engagement of their substrates. Previously, MERS-CoV PLpro has been observed to adopt at least two states upon binding Ub in what has been proposed as a closed state and an open state (17). Alignment of the MERS-CoV PLpro bound to ChISG15 with these Ub bound structures reveals that the protease in the MERS-CoV PLpro – ChISG15 adopts a conformation mirroring that of a closed state (Figure 4.4A) (17). More explicitly, the Zn finger domain found in MERS-CoV PLpro – ChISG15 structure forms addition interactions by wrapping around the ChISG15. This interaction is similar

to that found in the previously described closed state of MERS-CoV proteases bound to Ub (PDB: 4FR0) (17). This differs from the open state of the protease (PDB: 4RF1) where the Zn fingers are found peeled away from Ub limiting the protease's interaction with the substrate (Figure 4.4A).

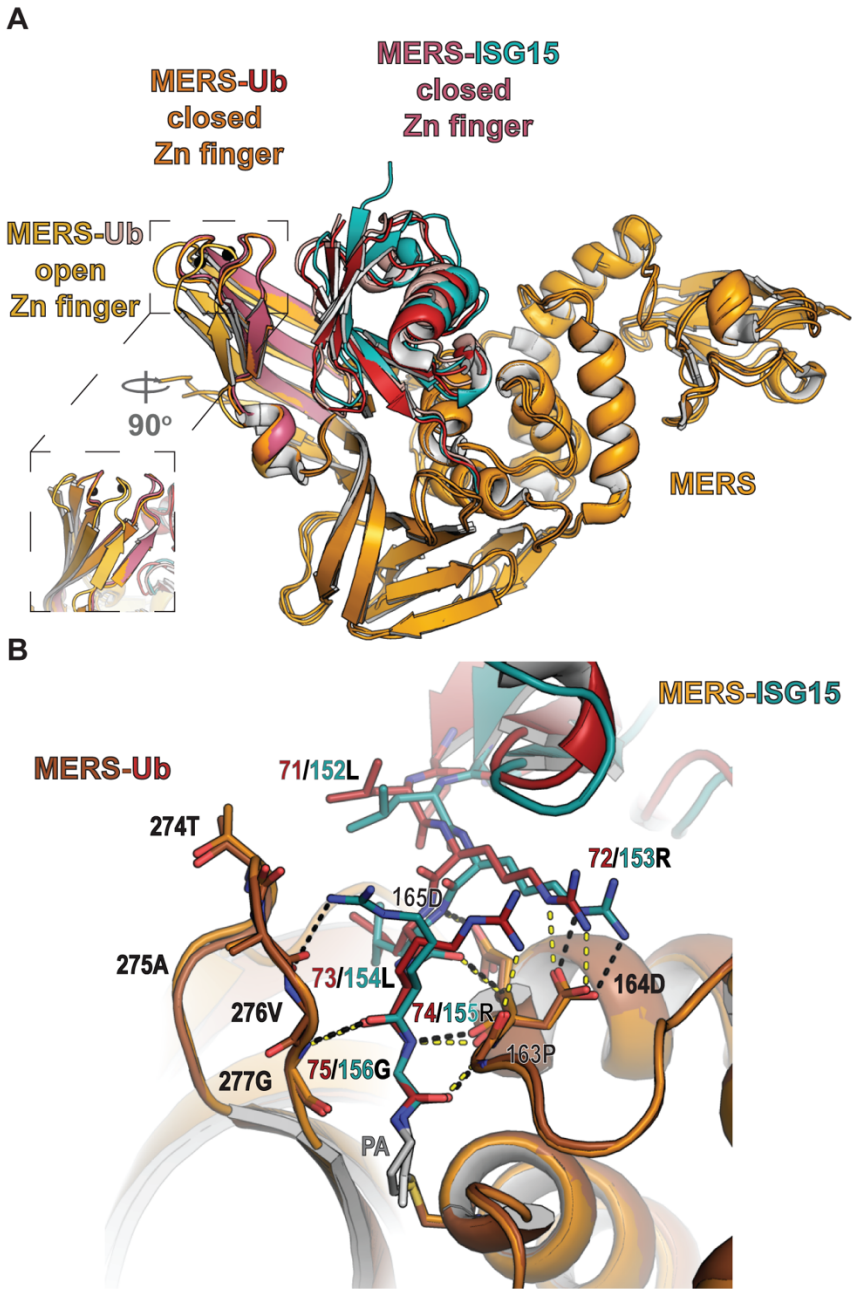

Figure 4.4. Comparison of ChISG15 and Ub binding by MERS-CoV. (A) Overlay of MERS-CoV PLpro-ChISG15 rendered as cartoons with the "open" and "closed" conformations of MERS-CoV PLpro bound to Ub (pink and burgundy respectively) (PDB: 4RF1; yellow and PDB: 4RF0; orange respectively). The MERS-CoV in complex with ChISG15 is colored as in (3A) with the

zinc finger colored in raspberry. The zinc atom is shown as a black sphere. (B) Close up of ChISG15 and Ub recognition sequence (LRLRGG) in MERS-CoV active site. The MERS-CoV in complex with ChISG15 is colored as in (3A) and MERS-CoV in complex with Ub colored in brown and burgundy, respectively.

Although MERS-CoV PLpro – ChISG15 resembles the closed state of MERS-CoV PLpro – Ub, the Ub molecule is oriented slightly different within the UIM pocket relative to CISG15. Closer examination of the active site illustrates that this deviation from the backbone prospective begins after Leu 154 of ISG15, and grows moving towards the Ub fold motif of ChISG15 (Figure 4.4B). In large part, the shared residues of the RLRGG C-terminal tail of Ub and ISG15 engage the protease in a similar manner. The lone exception is ISG15's Arg 155, whose long flexible side chain forms hydrostatic interactions with the carbonyl of Val276 of the protease instead of Pro163 as seen with Ub's Arg74. However, this change appears to have minimal impact on the backbone suggesting that the differences in orientation of ISG15 versus Ub within the UIM is likely the primary driver of the backbone deviations between the ISG15 and Ub residues within the active site. Given that the k_{cat} of MERS-CoV PLpro for ISG15 and Ub are relatively comparable, these changes do not appear to infer that there is a substantial difference in catalysis due to these differences (Table 4.3).

Table 4.3. Kinetic analysis of MERS-CoV PLpro and MERS-CoV PLpro mutants, K176E and V210D, with ISG15-AMC and Ub-AMC.

		ISG15-AMC	Ub-AMC
MERS-CoV PLpro WT			
k_{cat}/K_m	($\mu M^{-1}min^{-1}$)	7.13 ± 0.124	3.26 ± 0.0842
k_{cat}	(min^{-1})	15.62 ± 0.510	10.57 ± 0.270
K_m	(μM)	2.19 ± 0.255	3.24 ± 0.266
MERS-CoV PLpro K176E			
k_{cat}/K_m	($\mu M^{-1}min^{-1}$)	0.74 ± 0.170[†]	3.85 ± 0.120
k_{cat}	(min^{-1})	-	12.22 ± 0.430
K_m	(μM)	-	3.17 ± 0.366
MERS-CoV PLpro V210D			
k_{cat}/K_m	($\mu M^{-1}min^{-1}$)	0.23 ± 0.050[†]	2.93 ± 0.252
k_{cat}	(min^{-1})	-	29.44 ± 2.40
K_m	(μM)	-	10.04 ± 2.33

[†]Approximate k_{cat}/K_m values derived from the slope of the best fit line of the data presented in Figure 8B
Error determined using standard deviation

Intriguingly, the latter open state of MERS-CoV PLpro – Ub is more representative of the recently elucidated SARS-CoV PLpro – ChISG15 structure. This could advocate that much like PLpro's interaction with Ub, more than one bound state of hISG15 in a PLpro may also exist (Figure 4.5A). For the SARS-CoV PLpro, this may offer an explanation of how the remaining distance found in current models between the N-terminal domain of hISG15 and SARS-CoV PLpro's ridgeline helix residues close (19). Specifically, the movement of the Zn fingers in the SARS-CoV PLpro to a similar position in MERS-CoV PLpro would require movement of the bound ChISG15 domain.

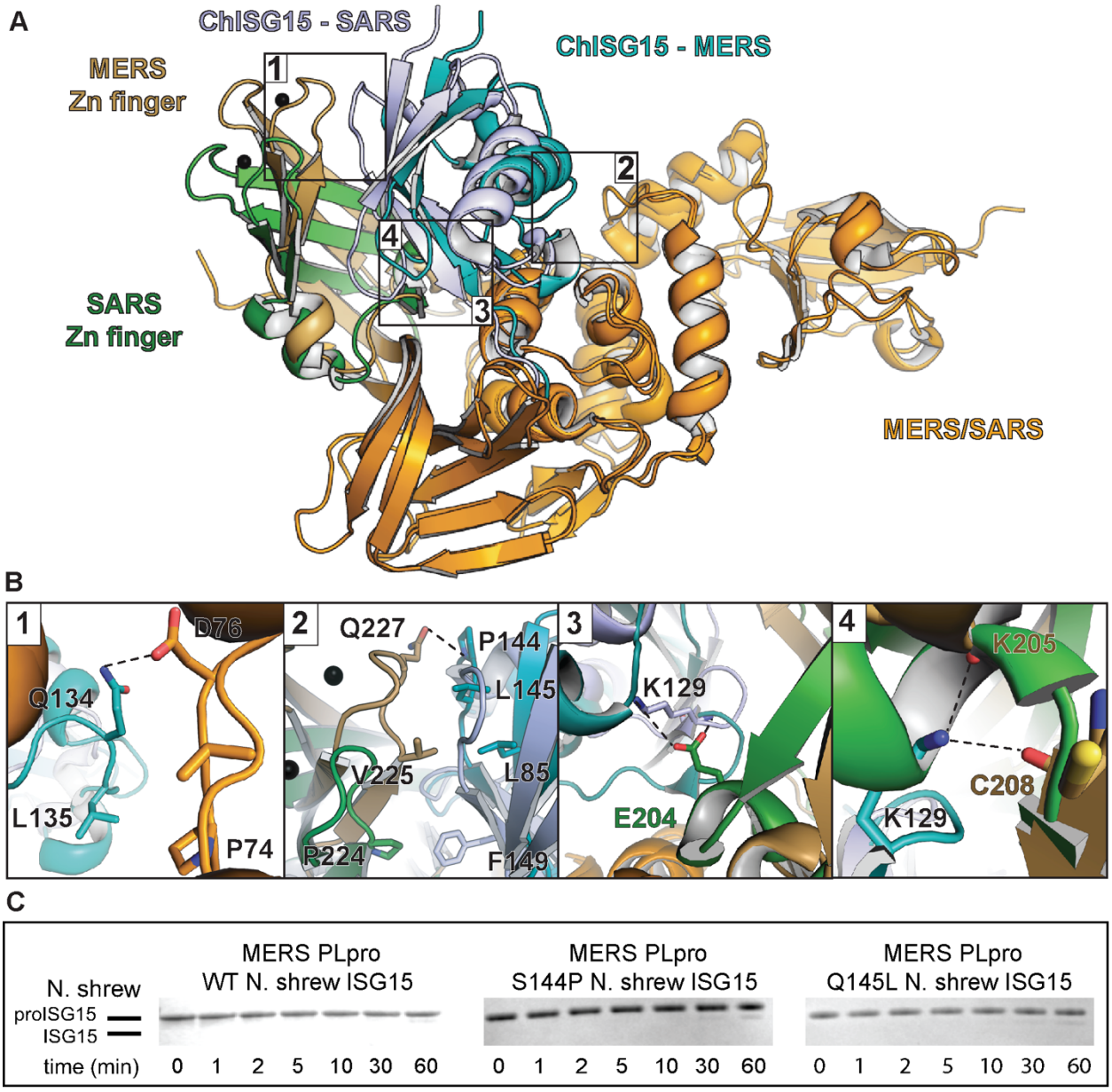

Figure 4.5. Comparison of ChISG15 and Ub binding by SARS-CoV. (A) Overlay of MERS-CoV PLpro-ChISG15 with SARS-CoV PLpro-ChISG15, shown as cartoons. MERS-CoV PLpro-ChISG15 is colored as in (3A) with its zinc finger highlighted in light brown, SARS-CoV PLpro colored like MERS with its zinc finger highlighted in forest green, and ChIS15 from the SARS-CoV PLpro complex colored in lavender. (B) Close up interactions illustrating the differences in the way the PLpros accommodate ChISG15 with hydrogen bonds represented with black dashed lines. (C) Cleavage assay of MERS-CoV against wild type shrew ISG15 and human derived mutant shrew ISG15.

Naturally, the global differences between SARS-CoV PLpro and MERS-CoV PLpro bound ChISG15 structures are reflected in specific amino acid interactions. Two of the hydrophobic interactions that drive the MERS-CoV PLpro's interaction with the ChISG15 are absent from the SARS-CoV PLpro and ChISG15 complex due to the more closed conformation of the zinc finger of the MERS-CoV PLpro. This closed conformation allows for one of the loops that coordinate the zinc to come in closer proximity to the ChISG15 creating the large hydrophobic seam. This conformation also allows for the interaction with the top of the thumb domain and helix connecting the Ubl-domain by the ChISG15, which creates the second hydrophobic interaction absent in the SARS-CoV PLpro – hISG15 interface (Figure 4.5B; panel 1). In addition, the hydrophobic interaction between the Pro224 of the SARS-CoV PLpro and Phe149 of the ChISG15 is lost in the MERS-CoV complex due to the replacement with a valine, which is not close enough to make an interaction (Figure 4.5B; panel 2). The only similarities between the two structures are that both proteases contain a hydrophobic interaction with Trp123, which is a highly-conserved residue amongst ISG15s, and that Lys129 from the ChISG15 makes hydrogen bonding networks with, although different, residues in the protease (Figure 4.5B; panels 3,4).

Given that the PLpros from MERS-CoV and SARS-CoV engage ChISG15 through different interactions, this may provide insight into how the two proteases' preference for ISG15 from certain species can differ. For instance, MERS-CoV PLpro was shown to have minimal activity towards ISG15 from the northern tree shrew, whereas PLpro from SARS-CoV rapidly processed this ISG15 (19). With the additional structural information surrounding MERS-CoV PLpro, this lack of efficacy towards northern tree shrew ISG15 for MERS-CoV PLpro may originate from differences between northern tree shrew ISG15 and hISG15 at positions 144 and 145. Instead of proline and leucine residues at these positions, northern tree shrew has a serine and

glutamine respectively (Figure 4.5B; panel 2). Through swapping these residues out in northern shrew ISG15 and assessing their relevance using a pro-form ISG15 cleavage assay, a minor improvement of MERS-CoV PLpro for northern shrew was observed. Specifically, a faint cleavage product was observed at the 30-minute mark in line with greater cleavage at the 60-minute mark. However, this improvement was very minor suggesting that additional differences between northern shrew and human ISG15, to possibly include the N-terminus, likely also play a factor in the species specificity of MERS-CoV PLpro.

N-terminal domain of hISG15

Despite the ITC affinity data between hISG15 and ChISG15 with MERS-CoV PLpro inferring possibly minimal interactions of the N-terminal domain of hISG15 with MERS-CoV PLpro, the additional rotation of ChISG15 within the binding site of MERS-CoV PLpro suggested the N-terminal domain of ISG15 might interact with MERS-CoV PLpro. To investigate this possibility, a model of MERS-CoV PLpro bound to hISG15 using a hISG15 structure (PDB: 1Z2M) with ChISG15 as an anchor was generated. Within this model, a number of residues potentially pointed towards where the N-terminal domain of hISG15 could be located (Figure 4.6A). To probe potential interaction of these residues with hISG15, the activity of wild-type MERS-CoV PLpro as well as MERS-CoV PLpro containing disruptive mutations at those sites were assessed using three substrates. These were Ub-, ISG15-, and a small peptide Z-RLRGG-AMC, which are designed utilizing the 7-amino-4-methylcoumarin (AMC) leaving group. The small peptide represents the consensus sequence for both Ub and ISG15 and is used as a control to ensure intrinsic catalytic activity is not significantly impacted. Although this set even contained some sites homologous to SARS-CoV PLpro's ridge helix, which were previously implicated in interacting with the N-terminal domain of hISG15, the potentially disruptive mutations failed to

reduce deISGylase activity (Figure 4.6B). Intriguingly, one mutation, E70A, located in the Ub-like domain had a significant uptick in deISGylase activity implying that residues in the Ubl potentially could play a role in some CoV PLpro-ISG15 interactions.

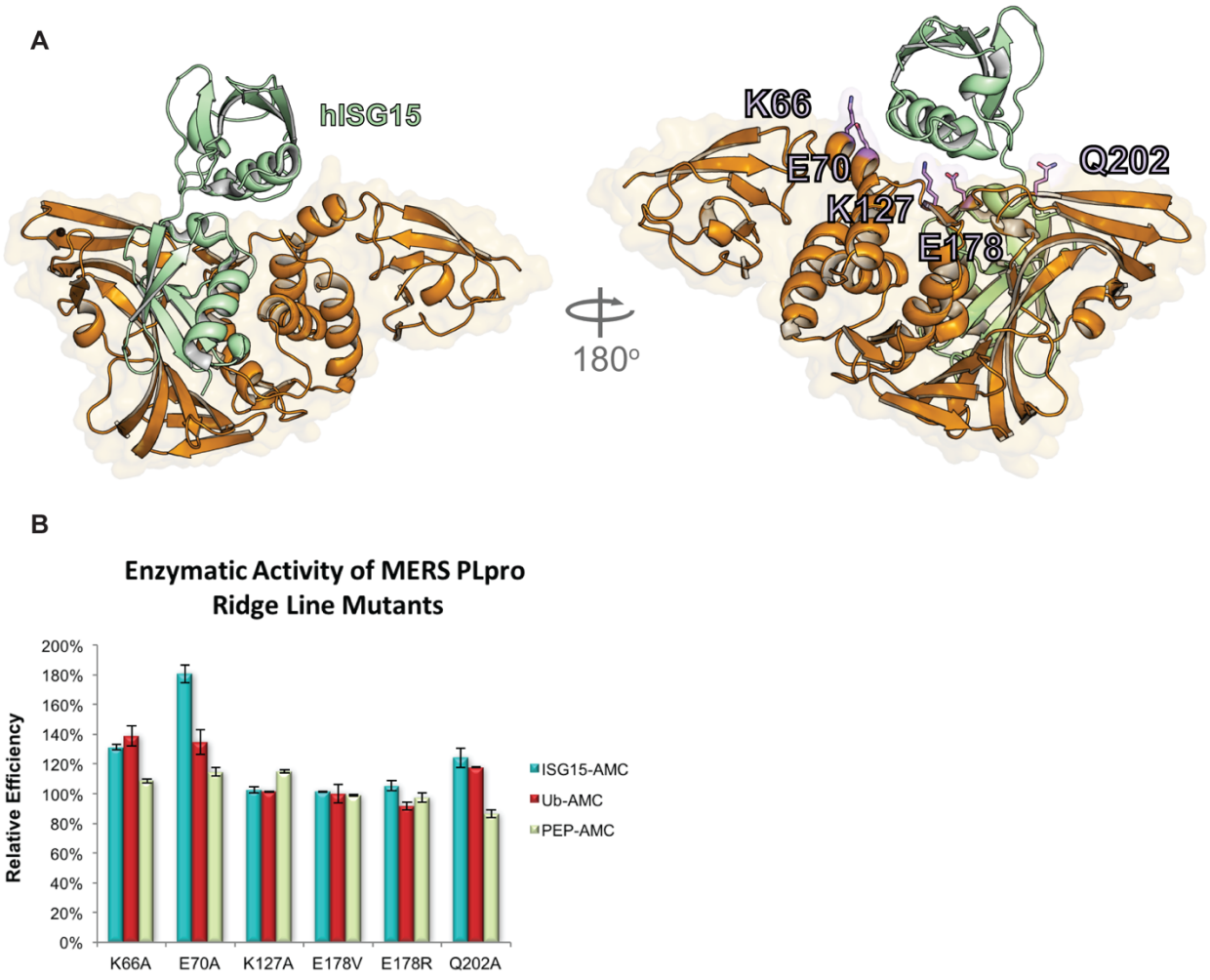

Figure 4.6. Model of full length ISG15 binding to MERS-CoV PLpro. (A) The C-terminal domain from full-length hISG15 (PDB: 1Z2M; light green), rendered as a cartoon, was aligned by LSQ using the ChISG15 from the MERS-CoV PLpro - ChISG15 structure as an anchor. The PLpro is shown as a cartoon with a transparent surface rendering, colored as in (3A). Mutation sites in the ridgeline helix are labeled in purple and shown as lavender sticks. (B) Enzyme activity of the ridgeline mutants, relative to the wildtype.

Structurally guided mutations to reduce deISGylase activity

One of the primary obstacles to observing the impact and role that viral deISGylase activity plays in viral host evasion and pathogenesis has been the inability to create attenuated viruses lacking this function. Specifically creating an attenuated PLP that decreases viral deISGylase activity while not significantly altering its other functionalities. Utilizing the newly available structural information related to the MERS-CoV PLpro – ChISG15 binding interface, along with ITC and mutational data advocating the C-terminal domain as the principle-binding domain, MERS-CoV PLpros with attenuated deISGylase activity was sought. Specifically, eleven mutations were designed for their potential to selectively disrupt the interface between MERS-CoV PLpro and hISG15 without appreciably impacting deubiquitinase and peptidase activities (Figure 4.7A,B).

Four of these mutations, V225D, V225A, Q227A, and R232V, had no substantial impact on any activity. However, one mutation, V225P, unexpectedly increases activity towards both Ub-AMC and ISG15-AMC (Figure 4.7B). For V225P, the original desired effect was to alter the size of the hydrophobic residue in a manner to discourage interaction with ISG15's Leu85 while encouraging tighter interactions with Ub's Phe4 (Figure 4.7C; panel 1). The over 80% increase in activity towards Ub-AMC and ISG15-AMC implies this strategy was ineffective (Figure 4.7B). One explanation might be that this mutation increased hydrophobic interactions of the protease with both substrates. A mutation having the opposite effect was R232A. The R232A mutation was designed take advantage of a H-bond interaction between the protease and hISG15 that is not present with Ub (Figure 4.7C; panel 2). This mutation resulted in a ~50% decrease in both deISGylase and deubiquitinase activity (Figure 4.7B). As a result, this appears to imply that the salt-bridge formed between Arg232 and Glu189 observed in the Zn finger of the MERS-CoV

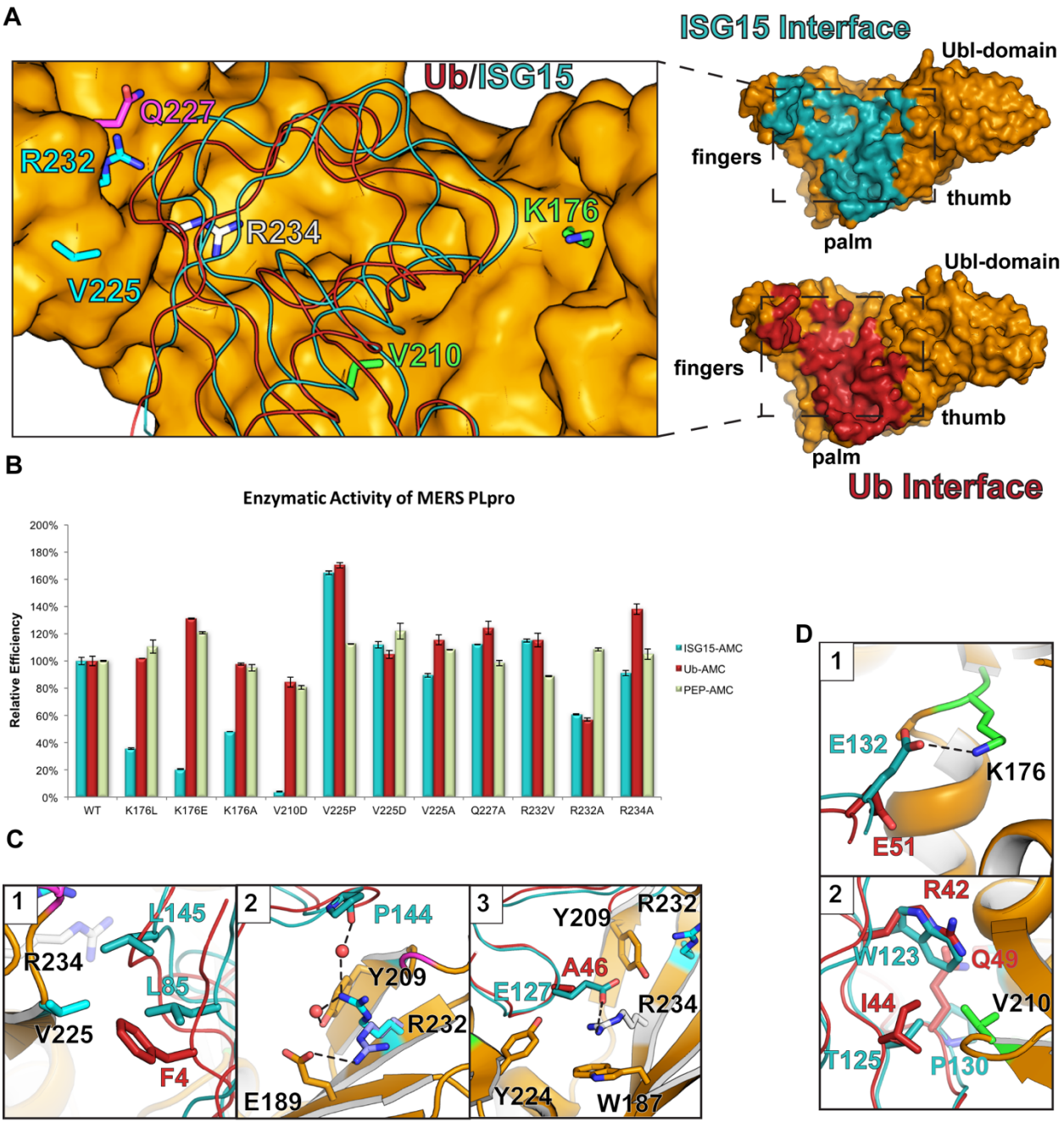

Figure 4.7. Structurally guided mutations utilizing the MERS-CoV PLpro bound to ChISG15. (A) Mutated resides highlighted based on activity, mutants in green reduce activity towards ISG15-AMC, mutants colored in cyan increase activity toward ISG15-AMC, the mutant colored in magenta shows little change in activity, and the mutant colored in grey increases activity towards Ub-AMC. ChISG15 and Ub from the closed conformation of MERS-CoV PLpro – Ub complex, rendered as ribbons, were overlayed based on an alignment with the MERS-CoV PLpros and colored as in (3A) and (4A). In the inset MERS PLpro's interaction surface with ISG15 and Ub is highlighted in teal and burgundy, respectively. (B) Enzyme activity of the mutants, at the

interface, relative to the wildtype. (C) Close up interactions of mutants that have an overall affect on ISG15-AMC and/or Ub-AMC activity with the electrostatic interactions represented with black dashed lines. In panel 2, R232 from the closed conformation of MERS-CoV PLpro bound to Ub is colored lilac. (D) Close up interactions of mutants that specifically reduce activity toward ISG15-AMC with electrostatic interactions represented with black dashed lines.

PLpro – Ub structure is key in the protease's engagement of Ub. Another mutation that gave a surprising result is R234A. Although it did give a slight decrease in activity towards ISG15-AMC, significant increase in activity towards Ub-AMC was observed (Figure 4.7B). This mutation was initially designed to disrupt salt-bridge interactions between MERS-CoV PLpro's Arg234 and hISG15's Glu127 (Figure 7C; panel 3). In light of the increased protease activity towards Ub-AMC, this alteration inadvertently boosted protease activity towards Ub-AMC. A possible explanation for this unexpected activity could be that the removal of the charged residue leaves a predominantly hydrophobic surface. This surface may be more likely to interact with the opposing hydrophobic surface of Ub (Figure 4.7C; panel 3).

Intriguingly, the most successful mutants to remove deISGylase activity occurred at positions 176 and 210. Mutations, K176L, K176E, and K176A, showed a significant decrease in ISG15 with little to no change in overall Ub activity (Figure 4.7B). These mutations were designed to disrupt the salt bridge formed by Lys176 with hISG15's Glu132 (Figure 4.7D; panel 1). This interaction is not observed between Ub and the protease due to the differences in the orientation of both residues. As a result, loss of the electrostatic interaction, for K176L and K176A, or introduction of an electrostatic repulsion, for K176E reduced the ability of the protease to engage hISG15. Of these, the electrostatic repulsion appeared to be the most effective at squelching deISGylase activity with little impact to other functionalities (Figure 4.7B). In addition to Lys176, the mutation of Val210 to an aspartic acid was the most successful in eliminating deISGylase

activity. The introduction of aspartic acid was designed to take advantage of the differences at Ub's Arg42, Ile44, and Gln49 and hISG15's Trp123, Thr125, and Pro130 respectively (Figure 4.7D; panel 2). The V210D mutation creates a steric hindrance and electrostatic repulsion with Trp123 of hISG15. There was the concern that this might also disrupt the nearby hydrophobic path involving Ub's Ile44. However, the deubiquitinase activity remains near wild-type levels suggesting that this either does not occur, or perhaps any disruption is offset with the formation of other interactions with nearby residues, possibly Arg42. The overall effect of the V210D mutation is a reduction of deISGylase activity to 4% (Figure 4.7B).

With V210D and K176E offering the most promising options to eliminate deISGylase activity without disrupting catalysis and retaining deubiquitinase activity, their impact on MERS-CoV function was further examined. Utilizing the pro-human form of ISG15 assay, the effects of V210D and K176E are considerable. Whereas MERS-CoV PLpro typically cleaves pro-hISG15 almost completely after 10 minutes, no complete cleavage of pro-hISG15 is observed for K176E after 60 minutes (Figure 4.8A). To gain insights on these mutations effect on binding Ub and ISG15, ITC was performed. Excitingly, no binding event was observed between either mutant and hISG15 (data not shown). In contrast, binding was detected with K176E and V210D for Ub. In detail, the K176E exhibited a dissociation constant of 7.41 ± 0.643 μM that mirrored that of wild-type MERS-CoV PLpro. The V210D mutant exhibited weaker binding to Ub with a K_D = 200.50 ± 7.77 μM that could be the source of the ~20% reduction of deubiquitinase activity observed for V210D during the 1 μM Ub-AMC assay (Table 4.1, Figure 4.2B). To provide further insight into the effects of the mutants, enzyme kinetic analysis of K176E and V210D was performed. The mutant K176E possessed a K_M = 3.17 ± 0.366 μM and k_{cat} = 12.22 ± 0.430 μM^{-1} min^{-1} for Ub that is virtually indistinguishable from that of wild-type MERS-CoV. The mutant V210D had a

threefold elevated K_M = 10.04 ± 2.33 echoing the weaker binding of Ub observed on the ITC. However, it also possessed a threefold higher k_{cat} of 29.44 ± 2.40 μM^{-1} min^{-1} (Figure 4.8B). As a result, the overall catalytic efficiencies for V210D and K176E were nearly identical to that of wild-type MERS-CoV for the Ub substrate (Table 4.3). In stark contrast to the Ub substrate, both V210D and K176E were unable to be saturated with the hISG15 substrate. Therefore, their apparent (k_{cat}/K_M) values were calculated from the slope of the line in Figure 8B. The mutants K176E and V210D had a five-fold and order of magnitude decrease of catalytic efficiency compared to wild-type MERS-CoV respectively (Table 4.3).

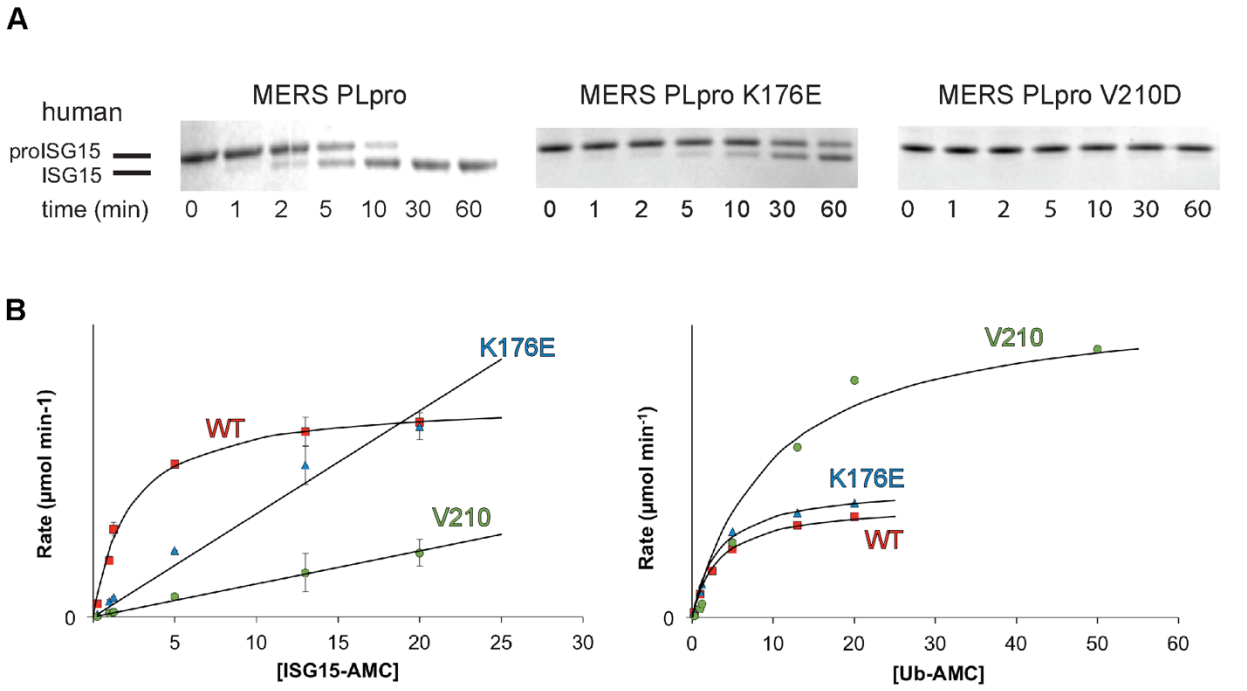

Figure 4.8. Analysis of MERS-CoV PLpro mutants K176E and V210D. (A) Cleavage assay of MERS-CoV PLpro and MERS-CoV PLpro mutants K176E and V210D against pro-human ISG15. (B) Graphs of steady state kinetics for MERS-CoV PLpro (red square) and MERS-CoV PLpro mutants K176E (blue triangle) and V210D (green circle) for ISG15- and Ub-AMC. Error was calculated using the standard deviation.

In perspective, V210D's k_{cat}/K_M of 0.23 ± 0.050 μM^{-1} min^{-1} and K176E's k_{cat}/K_M of 0.74 ± 0.170 μM^{-1} min^{-1} for the hISG15 substrate was more reflective of the k_{cat}/K_M of 0.3 ± 0.1 reported for SARS-CoV PLpro catalytic efficacy of the peptide-AMC(21). Additionally, a similar k_{cat}/K_M of 0.33 ± 0.066 μM^{-1} min^{-1} was observed for a Crimean-Congo Hemorrhagic Fever viral ovarian tumor domain (CCHFV vOTU) P77D mutant that had significant impaired ability to cleave cellular ISGylated substrates(22). As a result, the identification of the V210D and K176L/A/E mutants offer new tools for use in reverse genetic systems to probe how the removal of viral deISGylase activity impacts the pathogenesis of MERS-CoV and other deISGylase containing viruses.

Materials and Methods

Expression and purification of MERS-CoV PLpro

MERS-CoV PLpro in pET-15b was expressed as previously described (19). Purification was adapted from the previously described method (19). Briefly, cells expressing the recombinant protein were lysed in 500 mM NaCl, 50 mM Tris (pH 7.0), 10 mM β-mercaptoethanol (BME) for 30 minutes at 4 °C. The cells were subsequently sonicated on ice at 50% power, 50% duty cycle for a total of 6 minutes. The lysate was subjected to centrifugation at 70,600 xg for 30 minutes and the soluble fraction collected and filtered through a 0.8 μm filter. The protein was then poured over high density nickel agarose beads (Gold Biotechnology, Olivette, MO) pre-equilibrated with 500 mM NaCl, 50 mM Tris (pH 7.0) followed by a column wash with 10 column volumes of buffer supplemented with 10 mM imidazole, and elution with 10 column volumes of buffer supplemented with 300 mM imidazole. The eluted protein was furthered purified using a Superdex

200 column (GE Healthcare, Pittsburgh, PA) pre-equilibrated with 100 mM NaCl, 5 mM HEPES (pH 7.0), 2 mM DTT, and 0.1 mM $ZnCl_2$.

ITC of MERS-CoV PLpro binding with ChISG15, hISG15 and Ub

Expression and purification of ChISG15, hISG15 and Ub in pET-15b for ITC was done using the previously described protocol (23). ITC measurements of MERS-CoV PLpros with ChISG15, or Ub, were performed according to the previously published method (19). To summarize, ITC was performed using a Microcal PEAQ-ITC (Malvern, Worcestershire, UK). A series of 19 injections spaced at 180 seconds apart at 2 µl per injection was used. All injections were kept at a constant temperature of 25 °C utilizing a reference power of 4 µcal/s. Both the protease and substrate were dialyzed into 50 mM Hepes (pH 7.3), 200 mM NaCl, 1 mM DTT, and 0.1 mM $ZnCl_2$ overnight at 4 °C. For MERS-CoV PLpros and ChISG15, the protease was placed in the unit cell at 277 µM with ChISG15 in the syringe at 2.76 mM. This experiment was run at n=5. For MERS-CoV PLpros and either hISG15, or Ub, the protease was placed in the unit cell at 255 µM with the ligand in the syringe at 2.58 mM. These experiments were run in duplicate. The data was processed using Microcal PEAQ-ITC Analysis Software.

MERS-CoV PLpro-ChISG15 complex formation and purification

ChISG15 in the vector pTYB2 was expressed, purified, and derivatized as previously described (23). Complexation of the PLpro with the propargylamine-derivatized ChISG15 (ChISG15-PA) was adapted from the previously published method (19). In brief, approximately equimolar quantities of MERS-CoV PLpro and ChISG15-PA were mixed and incubated overnight night at 4 °C. The mixture was then dialyzed into 250 mM NaCl, 25 mM Hepes (pH 7.0) for 4 hours, filtered through a 0.8 µm filter, and poured over a nickel agarose column to eliminate

uncomplexed ChISG15. The column was washed with 10 CV buffer supplemented with 10 mM imidazole and the complex eluted with 10 CV buffer supplemented with 300 mM imidazole. The eluted complex was dialyzed in 250 mM NaCl, 25 mM Hepes (pH 7.0), 2 mM DTT, and 0.1 mM $ZnCl_2$. overnight with thrombin to cleave the His-6x tag. The Thrombin-cleaved complex was further purified by size exclusion chromatography using a Superdex 75 column (GE Healthcare, Pittsburgh, PA) pre-equilibrated with 100 mM NaCl, 5 mM HEPES (pH 7.0), 2 mM DTT, and 0.1 mM $ZnCl_2$.

Crystallization of MERS-CoV PLpro-ChISG15 complex

The purified complex was concentrated to 12.2 mg/mL and screened against a range of conditions in the QIAGEN NeXtal suites by hanging drop using a TTP Labtech Mosquito (TTP Labtech, Herfordshire, UK). The initial screen yielded the best crystals in a condition containing 200 mM $CaCl_2$, 100 mM $NaO_2C_2H_3$ pH 4.6, 30% (v/v) MPD. This condition was optimized using salt and precipitant gradients. The final optimized condition consisted of 200 mM $CaCl_2$, 100 mM $NaO_2C_2H_3$ pH 4.6, 28% (v/v) MPD. The final crystals for data collection were obtained by vapor diffusion using a 500 µL reservoir solution with 2 µL hanging drops consisting of protein and reservoir solution mixed in a 1:1 ratio.

Data Collection, processing, and structure refinement

Crystals of MERS-CoV PLpro-ChISG15 were soaked in mother liquor as a cryoprotectant and flash frozen in liquid N_2. Native and zinc single anomalous dispersion (Zn-SAD) data sets were collected at wavelengths 1.0 Å and 1.2837 Å respectively using 22-ID Argonne National Labs. Data sets were collected at 100K. Collected data sets were indexed, integrated, and scaled using HKL-2000 (24). Experimental phasing was employed using the PHENIX suite of programs.

In detail, Hybrid Substructure Search was used to find Zn sites, initially identifying seven, with Phaser solving the experimental phases (25, 26). Thereafter, autobuild and refinement using Coot and PHENIX generated a search model that was used for molecular replacement into the 2.4 Å native data set using Phaser. Subsequently, alternating rounds of model building and refinement in Coot and PHENIX were used to generate the final structure (27-30). The final structure was modelled with six Zn ions, with two occupying the Zn-ribbon motifs of the proteases and four involved in crystal packing between the proteases. The refined structure was validated using Molprobity (31). Statistics for data collection and refinement are presented in Table 2. Structures were deposited in the protein data bank with PDB codes 5W8T and 5W8U.

Generation of MERS-CoV PLpro and shrew proISG15 mutants

Mutations were introduced using the QuikChange Lightning kit according to the manufacturer's protocol (Agilent Technologies Inc.). The resultant plasmids were transformed into *Escherichia coli* NEB-5α cells by heat shock. Mutant plasmids were confirmed by sequencing and transformed into BL21(DE3) cells.

Mutational analysis of MERS-CoV PLpro enzymatic activity

Assessment of purified wildtype and mutant MERS-CoV PLpros activity was adapted from the described method (32). Briefly, each protease was tested against commercially available fluorogenic substrates of Ub, ISG15, and a peptide representing the shared C-terminal consensus sequence, Z-RLRGG, conjugated to 7-amino-4-methylcoumarin (AMC). All assays were performed in duplicate at 25 °C in 100 mM NaCl, 50 mM HEPES (pH 7.5), 0.01 mg/mL bovine serum albumin, 5 mM DTT in a 50 μL reaction volume using 96-well Corning Costar half-volume plates. For assays with Ub- and ISG15-AMC (Boston Biochem, MA), the enzyme was present at

5 nM and the substrate at 1 μM. For the Z-RLRGG-AMC (Bachem), the assay was run with 1 μM of enzyme and 50 μM of substrate. Fluorescence produced by cleavage of AMC from the substrate was measured using a CLARIOstar plate reader (BMG Labtech, Inc.) and the data analyzed using MARS (BMG Labtech, Inc.). Enzyme turnover rates were calculated utilizing steady-state kinetics.

Kinetic characterization of Ub-AMC and ISG15-AMC cleavage by MERS-CoV PLpro WT and V210D and K176E mutants

Further kinetic analysis for MERS-CoV PLpro and the V210D and K176E mutants was performed as for the initial assays with some modifications. Assays were run with 5 nM protease in a 30 μL reaction volume with concentrations of Ub- and ISG15-AMC varied from 0.25 μM to 20 μM. For MERS-CoV PLpro V210D with Ub-AMC an additional concentration was run at 50 μM. Reactions were initiated by the addition of protease. The initial reaction rates at each concentration of substrate were plotted and analyzed based on Michaelis-Menten kinetics using the Enzyme Kinetics software of SigmaPlot (v12 Systat Software Inc.). The plotted curves are shown in Figure 8, with values derived from the respective curves shown in Table 3. In the case of K176E with ISG15-AMC and V210D with ISG15-AMC and Ub-AMC for which the reaction rates did not approach saturation, apparent K_{cat}/K_m values were calculated based on linear regression of the initial velocity as a function of substrate concentration (21).

Cleavage of proISG15 by MERS-CoV PLpro

Shrew proISG15 mutants were expressed and purified based on the previously reported protocol (23). Cleavage assays of human with MERS-CoV PLpro V210D and K176E mutants, respectively, and shrew mutants S144P and Q145L with MERS-CoV PLpro WT were performed

as previously described (19, 23). Briefly, reactions were run in 100 mM NaCl, 5 mM HEPES (pH 7.5), 2 mM DTT at 37 °C with 20 nM protease and 10 μM proISG15. Samples were taken at time points up to one hour and the reaction quenched by mixing in equal parts with 2 x SDS-tricine sample buffer and boiling at 98 °C for 5 minutes. Samples were subsequently analyzed by SDS PAGE on 10-20% Mini-PROTEAN tris-tricine Precast Gels (Bio-Rad, Hercules, CA).

References

1. **WHO.** 2017. Middle East respiratory syndrome coronavirus (MERS-CoV), *on* World Heath Organization. http://www.who.int/mediacentre/factsheets/mers-cov/en/. Accessed
2. **Zaki AM, van Boheemen S, Bestebroer TM, Osterhaus ADME, Fouchier RAM.** 2012. Isolation of a Novel Coronavirus from a Man with Pneumonia in Saudi Arabia. New England Journal of Medicine **367:**1814-1820.
3. **Azhar EI, El-Kafrawy SA, Farraj SA, Hassan AM, Al-Saeed MS, Hashem AM, Madani TA.** 2014. Evidence for camel-to-human transmission of MERS coronavirus. N Engl J Med **370:**2499-2505.
4. **Vergara-Alert J, van den Brand JM, Widagdo W, Munoz Mt, Raj S, Schipper D, Solanes D, Cordon I, Bensaid A, Haagmans BL, Segales J.** 2017. Livestock Susceptibility to Infection with Middle East Respiratory Syndrome Coronavirus. Emerg Infect Dis **23:**232-240.
5. **Perlman S, Netland J.** 2009. Coronaviruses post-SARS: update on replication and pathogenesis. Nat Rev Microbiol **7:**439-450.
6. **Hilgenfeld R, Peiris M.** 2013. From SARS to MERS: 10 years of research on highly pathogenic human coronaviruses. Antiviral Research **100:**286-295.
7. **Thiel V, Ivanov KA, Putics Á, Hertzig T, Schelle B, Bayer S, Weißbrich B, Snijder EJ, Rabenau H, Doerr HW, Gorbalenya AE, Ziebuhr J.** 2003. Mechanisms and enzymes involved in SARS coronavirus genome expression. Journal of General Virology **84:**2305-2315.

8. **Barretto N, Jukneliene D, Ratia K, Chen Z, Mesecar AD, Baker SC.** 2005. The papain-like protease of severe acute respiratory syndrome coronavirus has deubiquitinating activity. J Virol **79:**15189-15198.

9. **Harcourt BH, Jukneliene D, Kanjanahaluethai A, Bechill J, Severson KM, Smith CM, Rota PA, Baker SC.** 2004. Identification of Severe Acute Respiratory Syndrome Coronavirus Replicase Products and Characterization of Papain-Like Protease Activity. Journal of Virology **78:**13600-13612.

10. **Mielech AM, Deng X, Chen Y, Kindler E, Wheeler DL, Mesecar AD, Thiel V, Perlman S, Baker SC.** 2015. Murine Coronavirus Ubiquitin-Like Domain Is Important for Papain-Like Protease Stability and Viral Pathogenesis. Journal of Virology **89:**4907-4917.

11. **Ratia K, Saikatendu KS, Santarsiero BD, Barretto N, Baker SC, Stevens RC, Mesecar AD.** 2006. Severe acute respiratory syndrome coronavirus papain-like protease: Structure of a viral deubiquitinating enzyme. Proceedings of the National Academy of Sciences **103:**5717-5722.

12. **Ratia K, Kilianski A, Baez-Santos YM, Baker SC, Mesecar A.** 2014. Structural Basis for the Ubiquitin-Linkage Specificity and deISGylating Activity of SARS-CoV Papain-Like Protease. PLoS Pathog **10:**e1004113.

13. **Davis ME, Gack MU.** 2015. Ubiquitination in the antiviral immune response. Virology **479-480:**52-65.

14. **Sadler AJ, Williams BR.** 2008. Interferon-inducible antiviral effectors. Nat Rev Immunol **8:**559-568.

15. **Frieman M, Ratia K, Johnston RE, Mesecar AD, Baric RS.** 2009. Severe acute respiratory syndrome coronavirus papain-like protease ubiquitin-like domain and catalytic domain regulate antagonism of IRF3 and NF-kappaB signaling. J Virol **83:**6689-6705.

16. **Devaraj SG, Wang N, Chen Z, Chen Z, Tseng M, Barretto N, Lin R, Peters CJ, Tseng C-TK, Baker SC, Li K.** 2007. Regulation of IRF-3-dependent Innate Immunity by the Papain-like

Protease Domain of the Severe Acute Respiratory Syndrome Coronavirus. Journal of Biological Chemistry **282:**32208-32221.

17. **Bailey-Elkin BA, Knaap RC, Johnson GG, Dalebout TJ, Ninaber DK, van Kasteren PB, Bredenbeek PJ, Snijder EJ, Kikkert M, Mark BL.** 2014. Crystal structure of the Middle East respiratory syndrome coronavirus (MERS-CoV) papain-like protease bound to ubiquitin facilitates targeted disruption of deubiquitinating activity to demonstrate its role in innate immune suppression. J Biol Chem **289:**34667-34682.

18. **Lei J, Hilgenfeld R.** 2016. Structural and mutational analysis of the interaction between the Middle-East respiratory syndrome coronavirus (MERS-CoV) papain-like protease and human ubiquitin. Virol Sin **31:**288-299.

19. **Daczkowski CM, Dzimianski JV, Clasman JR, Goodwin O, Mesecar AD, Pegan SD.** 2017. Structural Insights into the Interaction of Coronavirus Papain-Like Proteases and Interferon-Stimulated Gene Product 15 from Different Species. J Mol Biol **429:**1661-1683.

20. **Lindner HA, Lytvyn V, Qi H, Lachance P, Ziomek E, Ménard R.** 2007. Selectivity in ISG15 and ubiquitin recognition by the SARS coronavirus papain-like protease. Archives of Biochemistry and Biophysics **466:**8-14.

21. **Baez-Santos YM, Mielech AM, Deng X, Baker S, Mesecar AD.** 2014. Catalytic function and substrate specificity of the papain-like protease domain of nsp3 from the Middle East respiratory syndrome coronavirus. J Virol **88:**12511-12527.

22. **Akutsu M, Ye Y, Virdee S, Chin JW, Komander D.** 2011. Molecular basis for ubiquitin and ISG15 cross-reactivity in viral ovarian tumor domains. Proceedings of the National Academy of Sciences **108:**2228-2233.

23. **Deaton MK, Dzimianski JV, Daczkowski CM, Whitney GK, Mank NJ, Parham MM, Bergeron E, Pegan SD.** 2016. Biochemical and Structural Insights into the Preference of Nairoviral DeISGylases for Interferon-Stimulated Gene Product 15 Originating from Certain Species. Journal of Virology **90:**8314-8327.

24. **Otwinowski Z, Minor W.** 1997. Processing of X-ray diffraction data collected in oscillation mode, p 307-326. *In* Charles W. Carter, Jr. (ed), Methods in Enzymology, vol Volume 276. Academic Press.

25. **Grosse-Kunstleve RW, Adams PD.** 2003. Substructure search procedures for macromolecular structures. Acta Crystallographica Section D **59:**1966-1973.

26. **McCoy AJ, Storoni LC, Read RJ.** 2004. Simple algorithm for a maximum-likelihood SAD function. Acta Crystallographica Section D **60:**1220-1228.

27. **Emsley P, Cowtan K.** 2004. Coot: model-building tools for molecular graphics. Acta Crystallographica Section D **60:**2126-2132.

28. **McCoy AJ, Grosse-Kunstleve RW, Adams PD, Winn MD, Storoni LC, Read RJ.** 2007. Phaser crystallographic software. J Appl Crystallogr **40:**658-674.

29. **Terwilliger TC, Grosse-Kunstleve RW, Afonine PV, Moriarty NW, Zwart PH, Hung LW, Read RJ, Adams PD.** 2008. Iterative model building, structure refinement and density modification with the PHENIX AutoBuild wizard. Acta Crystallogr D Biol Crystallogr **64:**61-69.

30. **Adams PD, Afonine PV, Bunkoczi G, Chen VB, Davis IW, Echols N, Headd JJ, Hung LW, Kapral GJ, Grosse-Kunstleve RW, McCoy AJ, Moriarty NW, Oeffner R, Read RJ, Richardson DC, Richardson JS, Terwilliger TC, Zwart PH.** 2010. PHENIX: a comprehensive Python-based system for macromolecular structure solution. Acta Crystallogr D Biol Crystallogr **66:**213-221.

31. **Chen VB, Arendall WB, 3rd, Headd JJ, Keedy DA, Immormino RM, Kapral GJ, Murray LW, Richardson JS, Richardson DC.** 2010. MolProbity: all-atom structure validation for macromolecular crystallography. Acta Crystallogr D Biol Crystallogr **66:**12-21.

32. **Capodagli GC, Deaton MK, Baker EA, Lumpkin RJ, Pegan SD.** 2013. Diversity of Ubiquitin and ISG15 Specificity among Nairoviruses' Viral Ovarian Tumor Domain Proteases. Journal of Virology **87:**3815-3827 %! Diversity of Ubiquitin and ISG3815 Specificity among Nairoviruses' Viral Ovarian Tumor Domain Proteases.

CHAPTER 5

DISCUSSION

Coronavirus PLP substrate specificity

PLPs originating from CoVs have been observed to play a key role in the suppression of the innate immune response through the reversal of post-translational modification by Ub and ISG15. Ub and ISG15 have been shown to play a direct role in the antiviral innate immune response and later stages of immunity respectively (72). Understanding how the removal of these post-translational modifications, processes known as deubiquitination and deISGylation, could be vital to understand the immune pathways affected and the underlying differences in pathogenicity of these different viral species. Utilizing at least one CoV PLP representative from three of the subfamilies, *Alphacoronavirus* PEDV, *Betacoronavirus* SARS- and MERS-CoV, and PDCoV from *Deltacoronavirus*, a wide array of PLP substrate specificities was revealed. Specifically, the PLP from PEDV and the PLpro from PDCoV seemed to possess either deubiquitinating or deISGylating activity respectively with equal overall catalytic efficiency. This is in contrast to the SARS- and MERS-CoV PLpro, which contain both activities in relative equal capacity (75, 76).

In the context of the two porcine viruses, PDCoV's prevalence is lower in swine populations compared to that of PEDV; however, PEDV and PDCoV are often present as co-infections, seen to occur together in up to 78% of cases (77, 78). There is a potential for these two viruses' PLPs to have coevolved because they infect the same species in the same geographical areas and have taken advantage of the opposing PLP's substrate preference. Because deubiquitinating and deISGylating activities have been found to occur at different points in the

innate immune response, these two viruses could attack the porcine's immune system at different times ensuring lasting viral infections. Another example of a coinfection being advantageous for viruses, in a swine host, is that of coinfections with porcine respiratory reproductive syndrome virus (PRRSV) and influenza B (79). In this case, PRRSV PLP2 is a known deubiquitinase and deISGylase while the NS1 protein of influenza B virus (NS1B) is known to bind and sequester ISG15; however, only ISG15 from human and nonhuman primates (80-82). As a result, the deISGylase activity of the PRRSV PLP2 could potentially make up for the inability of influenza B to sequester porcine ISG15, possibly still suppressing the innate immune response and positively influencing pathogenesis. The SARS- and MERS-CoV are not seen in co-infection systems and potentially one reason why their PLPs have prominent deubiquitinating and deISGylating activities.

Ubiquitination, and subsequent deubiquitination by the PLP, goes beyond a single Ub moiety and extends to the poly-Ub linkages at either one of seven lysine positions or the amino terminal methionine. K48- and K63-linkages are the most well studied in terms of the antiviral innate immune response with K48-linkages involved in proteasomal degradation and K63-linkages involved in signal transduction and substrate stabilization (3). PLPs have been shown to prefer K48-linked poly-Ub over any of the other possible positions (83). This holds true for the PLpro from SARS- and MERS-CoV and the PLP2 from PEDV, which suggests the PLP's main route of innate immune suppression is through downregulating the pro-inflammatory cytokines produced through the NF-κB pathway. The PLP from PEDV however, also had a significantly higher preference for K11-, K6-, and K63-linkages compared to the PLpro from SARS- and MERS-CoV. This implies the PLP has the ability to evolve in substrate preferences due to evolutionary pressures to overcome the host immunity in new ways. Significant K11 and K63 poly-Ub preference could

suggest new pathway targets for the PLP, such as the STING and the RIG-I/MAVS complex, respectively. This could begin to explain an increase in pathogenicity in the highly pathogenic PEDV compared its other porcine coronavirus counterpart, PDCoV, because the entire type-I interferon regulation system would be significantly downregulated.

Coronavirus PLP species specificity

Compared to the almost completely conserved Ub, ISG15 can vary in sequence identity from species to species as low as 35% across a broad sampling of animals. Recently, work done with the nairovirus vOTU, the other prominent DUB protease class, begins to explain how ISG15 works at later stages of the immune system and can be species dependent (23, 72). In addition, the vOTU from several different nairovirus species were shown to have the ability to cleave a wide variety of species' ISG15 especially species they are known to infect (23). This held true for the CoV PLPs as well (75). SARS- and MERS-CoV PLpro were able to recognize and cleave a wide variety of species' ISG15, especially those that they have known to previously infect or species that are the current host for these coronaviruses. For example, MERS-CoV is known to readily infect camels, ruminants, and humans and said to have originated first in a bat host before jumping to these other animals (84, 85). The MERS-CoV PLpro was able to recognize and readily cleave all of these species of ISG15. Interestingly, MHV is known to only infect mice, which was also represented in the ISG15 species panel assay (74). The MHV PLP2 was able to recognize and readily cleave the ISG15 from mouse over most of the other ISG15 species that were assessed. However, MHV PLP2 was also able to readily cleave fish ISG15, but that could potentially be because the fish ISG15 sequence more closely resembles Ub and from other studies the MHV PLP2 contains deubiquitinating activity as well (74). This was also seen for the PLpro from

PDCoV where the only known host is porcine and the only ISG15 species the PLpro could recognize was exactly that of the porcine.

Utilizing the information from the proISG15 assay and the diverse set of species of ISG15s assessed, a glimpse into these CoV's evolution is now possible. If a CoV can effectively recognize and cleave a certain species of ISG15 it potentially means that at one point this species was a host for that particular coronavirus or even an unknown current reservoir. This information can provide a predictive model to assess the species these CoV infected in the past, how they could have or currently are moving from species to species, and any species they might infect in the future. This tool becomes very powerful for the prediction of future zoonotic outbreaks of these viruses in that if a CoV PLP can cleave a certain species' ISG15 it can potentially infect that given species. All viruses have selective pressures to evolve and better overcome the host immune system and if possible spread to other reservoirs to maintain circulation in populations. For CoVs specifically, having the ability to recognize different species' ISG15 could potentially allow them to move to new reservoirs and take advantage of these later immune down regulation processes to now circulate in a completely different host/environment and survive.

Coronavirus PLPs' engagement and accommodation of ISG15

Recent studies showing the CoV PLPs to not only have robust deubiquitinating activity but also have robust deISGylase activity that is species dependent, a clear need for a detailed understanding of the molecular interactions between CoV PLPs and ISG15 became evident. The first structural data of how different CoV PLPs could engage ISG15 provided much needed evidence in the development of molecular tools, which can be used to engineer CoV PLPs to delve deeper into understanding how deubiquitinating and deISGylating activity relates to CoV pathogenesis. These structures provided evidence that: 1. The N-terminal domain of ISG15 could

or could not play a role in binding, 2. The CoV PLP can adopt different conformations to accommodate different species of ISG15, 3. A closer look at the specific amino acids responsible for driving the interaction between the MERS-CoV PLpro and human ISG15 (hISG15).

The structures and accompanying biochemical data from the SARS-CoV PLpro in complex with both the C-terminal domains of hISG15 (ChISG15) and mouse ISG15 (mISG15/CmISG15) showed the Ub-like (UBL) domain of the PLP to adopt more than one conformation. The UBL domain of SARS-CoV PLpro was shown to rotate almost 90° depending on which species of ISG15 was bound. Again, making the argument that the CoV PLP has the ability to evolve, especially within their binding interface, to potentially accommodate a wide variety of specie ISG15s. These structures also provided evidence on how a PLP can engage both the C-terminal and N-terminal domains of ISG15, which was previously still in question.

The alternate conformations that were observed for the CoV PLP extend beyond the movement of the UBL domain and rather to the entire PLP domain itself. The MERS-CoV PLpro bound to the ChISG15 revealed a closed conformation of the PLpro, which was in contrast to the open conformation seen in the SARS-CoV PLpro-hISG15. The closed confirmation, where the zinc fingers move making the binding pocket smaller, could potentially explain the space between the N-terminal domain of hISG15 and the ridgeline helix of the SARS-CoV PLpro. In addition, the closed conformation of MERS-CoV PLpro has allowed insight into the potential binding of the PLpro and ISG15 that occurs in nature. This structural information revealed a more realistic depiction of the binding event with the MERS-CoV PLpro wrapping around the ChISG15, which has provided insight into the exact molecular drivers behind the interaction between the MERS-CoV PLpro and hISG15.

Up until now, there were no existing disruptive CoV mutants with attenuated deISGylase activity, which makes studying viral pathogenesis and viral host evasion very difficult. Utilizing the structural and biochemical information from the MERS-CoV PLpro – ChISG15 structure, specific amino acids were identified that are directly involved in the interaction between the MERS-CoV and hISG15. These mutants, K176E and V210D, are the first CoV PLP disruptive mutants identified that contain sole attenuated deISGylase activity. The molecular tools gained from this study now allow for the development of reverse genetic systems to study the role of deISGylase activity on pathogenesis and viral evasion of the host without the influence of deubiquitinase activity. Taken together with the insight into the more realistic conformation of PLPs in nature, this study has created a multitude of new possibilities in the way of engineering PLPs to further advance our understanding of CoVs during infection.

Future Directions

The above studies provide the first opportunity to assess the function of the CoV PLP, in the context of viral infection, in the way of recombinant virus variants with altered deISGylase ability. Again, these MERS-CoV PLpro mutations with altered deISGylase function provide a tool to begin investigating the delineated role of deubiquitinase and deISGylase activity in terms of pathogenesis. They can be used in cellular studies to evaluate which pathways, for example if ISG15 is required for stabilizing IRF3 for further regulation and production of type-I interferons within the antiviral innate immune response, in order to determine if ISG15 is acting in later stages of the immune response similar to that observed in vOTUs (72). Potentially, cellular studies utilizing luciferase reporter genes controlled by downstream immune system promoters, for example the IFN-β promoter, can be used to determine where ISG15 might be playing a role in type-I interferon stimulation and regulation. In addition, the disruptive MERS-CoV mutants can

be used in mouse model studies to further investigate the role of PLP deISGylase function. The future mouse studies were made possible because the MERS-CoV PLpro mutants were observed to no longer have the ability to cleave mISG15 as well as hISG15 (data not shown). This will allow the ISGylation systems to remain intact and potentially lead to the discovery of how ISG15 is acting in the immune system in response to viral infection and also how deISGylase activity by the PLPs is involved in pathogenicity and viral host evasion.

REFERENCES

1. Bailey-Elkin BA, Knaap RCM, Kikkert M, Mark BL. 2017. Structure and Function of Viral Deubiquitinating Enzymes. J Mol Biol 429:3441-3470.
2. Ivashkiv LB, Donlin LT. 2014. Regulation of type I interferon responses. Nat Rev Immunol 14:36-49.
3. Davis ME, Gack MU. 2015. Ubiquitination in the antiviral immune response. Virology 479-480:52-65.
4. Sadler AJ, Williams BR. 2008. Interferon-inducible antiviral effectors. Nat Rev Immunol 8:559-68.
5. Schneider WM, Chevillotte MD, Rice CM. 2014. Interferon-stimulated genes: a complex web of host defenses. Annu Rev Immunol 32:513-45.
6. Heaton SM, Borg NA, Dixit VM. 2016. Ubiquitin in the activation and attenuation of innate antiviral immunity. J Exp Med 213:1-13.
7. Hu H, Sun SC. 2016. Ubiquitin signaling in immune responses. Cell Res 26:457-83.
8. Jiang X, Chen ZJ. 2011. The role of ubiquitylation in immune defence and pathogen evasion. Nature reviews Immunology 12:10.1038/nri3111.
9. Chiang C, Gack MU. 2017. Post-translational Control of Intracellular Pathogen Sensing Pathways. Trends Immunol 38:39-52.
10. Lei J, Hilgenfeld R. 2017. RNA-virus proteases counteracting host innate immunity. FEBS Lett 591:3190-3210.

11. McFadden MJ, Gokhale NS, Horner SM. 2017. Protect this House: Cytosolic Sensing of Viruses. Current opinion in virology 22:36-43.

12. Sparrer KM, Gack MU. 2015. Intracellular detection of viral nucleic acids. Curr Opin Microbiol 26:1-9.

13. Okamoto M, Kouwaki T, Fukushima Y, Oshiumi H. 2017. Regulation of RIG-I Activation by K63-Linked Polyubiquitination. Frontiers in Immunology 8:1942.

14. Seth RB, Sun L, Ea CK, Chen ZJ. 2005. Identification and characterization of MAVS, a mitochondrial antiviral signaling protein that activates NF-kappaB and IRF 3. Cell 122:669-82.

15. Kawai T, Takahashi K, Sato S, Coban C, Kumar H, Kato H, Ishii KJ, Takeuchi O, Akira S. 2005. IPS-1, an adaptor triggering RIG-I- and Mda5-mediated type I interferon induction. Nat Immunol 6:981-8.

16. Xu LG, Wang YY, Han KJ, Li LY, Zhai Z, Shu HB. 2005. VISA is an adapter protein required for virus-triggered IFN-beta signaling. Mol Cell 19:727-40.

17. Meylan E, Curran J, Hofmann K, Moradpour D, Binder M, Bartenschlager R, Tschopp J. 2005. Cardif is an adaptor protein in the RIG-I antiviral pathway and is targeted by hepatitis C virus. Nature 437:1167-72.

18. Chen Q, Sun L, Chen ZJ. 2016. Regulation and function of the cGAS-STING pathway of cytosolic DNA sensing. Nat Immunol 17:1142-9.

19. Lazear HM, Daniels BP, Pinto AK, Huang AC, Vick SC, Doyle SE, Gale M, Jr., Klein RS, Diamond MS. 2015. Interferon-lambda restricts West Nile virus neuroinvasion by tightening the blood-brain barrier. Sci Transl Med 7:284ra59.

20. Schoggins JW, Rice CM. 2011. Interferon-stimulated genes and their antiviral effector functions. Curr Opin Virol 1:519-25.

21. Levy DE, Marie IJ, Durbin JE. 2011. Induction and function of type I and III interferon in response to viral infection. Curr Opin Virol 1:476-86.

22. Hermann M, Bogunovic D. 2017. ISG15: In Sickness and in Health. Trends Immunol 38:79-93.

23. Deaton MK, Dzimianski JV, Daczkowski CM, Whitney GK, Mank NJ, Parham MM, Bergeron E, Pegan SD. 2016. Biochemical and Structural Insights into the Preference of Nairoviral DeISGylases for Interferon-Stimulated Gene Product 15 Originating from Certain Species. Journal of Virology 90:8314-8327.

24. Hershko A, Ciechanover A. 1998. The ubiquitin system. Annu Rev Biochem 67:425-79.

25. Hershko A, Heller H, Elias S, Ciechanover A. 1983. Components of ubiquitin-protein ligase system. Resolution, affinity purification, and role in protein breakdown. J Biol Chem 258:8206-14.

26. Ciechanover A, Elias S, Heller H, Hershko A. 1982. "Covalent affinity" purification of ubiquitin-activating enzyme. J Biol Chem 257:2537-42.

27. Kirisako T, Kamei K, Murata S, Kato M, Fukumoto H, Kanie M, Sano S, Tokunaga F, Tanaka K, Iwai K. 2006. A ubiquitin ligase complex assembles linear polyubiquitin chains. EMBO J 25:4877-87.

28. Chau V, Tobias JW, Bachmair A, Marriott D, Ecker DJ, Gonda DK, Varshavsky A. 1989. A multiubiquitin chain is confined to specific lysine in a targeted short-lived protein. Science 243:1576-83.

29. Chen ZJ, Sun LJ. 2009. Nonproteolytic functions of ubiquitin in cell signaling. Mol Cell 33:275-86.

30. Zinngrebe J, Montinaro A, Peltzer N, Walczak H. 2014. Ubiquitin in the immune system. EMBO Rep 15:28-45.

31. Wu-Baer F, Lagrazon K, Yuan W, Baer R. 2003. The BRCA1/BARD1 heterodimer assembles polyubiquitin chains through an unconventional linkage involving lysine residue K6 of ubiquitin. J Biol Chem 278:34743-6.

32. Nishikawa H, Ooka S, Sato K, Arima K, Okamoto J, Klevit RE, Fukuda M, Ohta T. 2004. Mass spectrometric and mutational analyses reveal Lys-6-linked polyubiquitin chains catalyzed by BRCA1-BARD1 ubiquitin ligase. J Biol Chem 279:3916-24.

33. Morris JR, Solomon E. 2004. BRCA1 : BARD1 induces the formation of conjugated ubiquitin structures, dependent on K6 of ubiquitin, in cells during DNA replication and repair. Hum Mol Genet 13:807-17.

34. Wickliffe KE, Williamson A, Meyer HJ, Kelly A, Rape M. 2011. K11-linked ubiquitin chains as novel regulators of cell division. Trends Cell Biol 21:656-63.

35. Boname JM, Thomas M, Stagg HR, Xu P, Peng J, Lehner PJ. 2010. Efficient internalization of MHC I requires lysine-11 and lysine-63 mixed linkage polyubiquitin chains. Traffic 11:210-20.

36. Dynek JN, Goncharov T, Dueber EC, Fedorova AV, Izrael-Tomasevic A, Phu L, Helgason E, Fairbrother WJ, Deshayes K, Kirkpatrick DS, Vucic D. 2010. c-IAP1 and UbcH5 promote K11-linked polyubiquitination of RIP1 in TNF signalling. EMBO J 29:4198-209.

37. Gerlach B, Cordier SM, Schmukle AC, Emmerich CH, Rieser E, Haas TL, Webb AI, Rickard JA, Anderton H, Wong WW, Nachbur U, Gangoda L, Warnken U, Purcell AW, Silke J, Walczak H. 2011. Linear ubiquitination prevents inflammation and regulates immune signalling. Nature 471:591-6.

38. Glauser L, Sonnay S, Stafa K, Moore DJ. 2011. Parkin promotes the ubiquitination and degradation of the mitochondrial fusion factor mitofusin 1. J Neurochem 118:636-45.

39. Geisler S, Holmstrom KM, Skujat D, Fiesel FC, Rothfuss OC, Kahle PJ, Springer W. 2010. PINK1/Parkin-mediated mitophagy is dependent on VDAC1 and p62/SQSTM1. Nat Cell Biol 12:119-31.

40. Peng DJ, Zeng M, Muromoto R, Matsuda T, Shimoda K, Subramaniam M, Spelsberg TC, Wei WZ, Venuprasad K. 2011. Noncanonical K27-linked polyubiquitination of TIEG1 regulates Foxp3 expression and tumor growth. J Immunol 186:5638-47.

41. Al-Hakim AK, Zagorska A, Chapman L, Deak M, Peggie M, Alessi DR. 2008. Control of AMPK-related kinases by USP9X and atypical Lys(29)/Lys(33)-linked polyubiquitin chains. Biochem J 411:249-60.

42. Huang H, Jeon MS, Liao L, Yang C, Elly C, Yates JR, 3rd, Liu YC. 2010. K33-linked polyubiquitination of T cell receptor-zeta regulates proteolysis-independent T cell signaling. Immunity 33:60-70.

43. Haas TL, Emmerich CH, Gerlach B, Schmukle AC, Cordier SM, Rieser E, Feltham R, Vince J, Warnken U, Wenger T, Koschny R, Komander D, Silke J, Walczak H. 2009. Recruitment of the linear ubiquitin chain assembly complex stabilizes the TNF-R1 signaling complex and is required for TNF-mediated gene induction. Mol Cell 36:831-44.

44. Tokunaga F, Sakata S, Saeki Y, Satomi Y, Kirisako T, Kamei K, Nakagawa T, Kato M, Murata S, Yamaoka S, Yamamoto M, Akira S, Takao T, Tanaka K, Iwai K. 2009. Involvement of linear polyubiquitylation of NEMO in NF-kappaB activation. Nat Cell Biol 11:123-32.

45. Chang M, Jin W, Sun SC. 2009. Peli1 facilitates TRIF-dependent Toll-like receptor signaling and proinflammatory cytokine production. Nat Immunol 10:1089-95.

46. Hacker H, Redecke V, Blagoev B, Kratchmarova I, Hsu LC, Wang GG, Kamps MP, Raz E, Wagner H, Hacker G, Mann M, Karin M. 2006. Specificity in Toll-like receptor signalling through distinct effector functions of TRAF3 and TRAF6. Nature 439:204-7.

47. May MJ, Ghosh S. 1998. Signal transduction through NF-kappa B. Immunol Today 19:80-8.

48. Wang Q, Liu X, Cui Y, Tang Y, Chen W, Li S, Yu H, Pan Y, Wang C. 2014. The E3 ubiquitin ligase AMFR and INSIG1 bridge the activation of TBK1 kinase by modifying the adaptor STING. Immunity 41:919-33.

49. Malynn BA, Ma A. 2010. Ubiquitin makes its mark on immune regulation. Immunity 33:843-52.

50. van der Veen AG, Ploegh HL. 2012. Ubiquitin-like proteins. Annu Rev Biochem 81:323-57.

51. Korant BD, Blomstrom DC, Jonak GJ, Knight E, Jr. 1984. Interferon-induced proteins. Purification and characterization of a 15,000-dalton protein from human and bovine cells induced by interferon. J Biol Chem 259:14835-9.

52. Morales DJ, Lenschow DJ. 2013. The antiviral activities of ISG15. J Mol Biol 425:4995-5008.

53. Yuan W, Krug RM. 2001. Influenza B virus NS1 protein inhibits conjugation of the interferon (IFN)-induced ubiquitin-like ISG15 protein. EMBO J 20:362-71.

54. Krug RM, Zhao C, Beaudenon S. 2005. Properties of the ISG15 E1 enzyme UbE1L. Methods Enzymol 398:32-40.

55. Zhao C, Beaudenon SL, Kelley ML, Waddell MB, Yuan W, Schulman BA, Huibregtse JM, Krug RM. 2004. The UbcH8 ubiquitin E2 enzyme is also the E2 enzyme for ISG15, an IFN-alpha/beta-induced ubiquitin-like protein. Proc Natl Acad Sci U S A 101:7578-82.

56. Zou W, Zhang DE. 2006. The interferon-inducible ubiquitin-protein isopeptide ligase (E3) EFP also functions as an ISG15 E3 ligase. J Biol Chem 281:3989-94.

57. Dastur A, Beaudenon S, Kelley M, Krug RM, Huibregtse JM. 2006. Herc5, an interferon-induced HECT E3 enzyme, is required for conjugation of ISG15 in human cells. J Biol Chem 281:4334-8.

58. Potter JL, Narasimhan J, Mende-Mueller L, Haas AL. 1999. Precursor processing of pro-ISG15/UCRP, an interferon-beta-induced ubiquitin-like protein. J Biol Chem 274:25061-8.

59. Hsiang TY, Zhao C, Krug RM. 2009. Interferon-induced ISG15 conjugation inhibits influenza A virus gene expression and replication in human cells. J Virol 83:5971-7.

60. Pincetic A, Kuang Z, Seo EJ, Leis J. 2010. The interferon-induced gene ISG15 blocks retrovirus release from cells late in the budding process. J Virol 84:4725-36.

61. Okumura F, Zou W, Zhang DE. 2007. ISG15 modification of the eIF4E cognate 4EHP enhances cap structure-binding activity of 4EHP. Genes Dev 21:255-60.

62. Kuang Z, Seo EJ, Leis J. 2011. Mechanism of inhibition of retrovirus release from cells by interferon-induced gene ISG15. J Virol 85:7153-61.

63. Giannakopoulos NV, Luo JK, Papov V, Zou W, Lenschow DJ, Jacobs BS, Borden EC, Li J, Virgin HW, Zhang DE. 2005. Proteomic identification of proteins conjugated to ISG15 in mouse and human cells. Biochem Biophys Res Commun 336:496-506.

64. Malakhova OA, Kim KI, Luo JK, Zou W, Kumar KG, Fuchs SY, Shuai K, Zhang DE. 2006. UBP43 is a novel regulator of interferon signaling independent of its ISG15 isopeptidase activity. EMBO J 25:2358-67.

65. Zhao C, Denison C, Huibregtse JM, Gygi S, Krug RM. 2005. Human ISG15 conjugation targets both IFN-induced and constitutively expressed proteins functioning in diverse cellular pathways. Proc Natl Acad Sci U S A 102:10200-5.

66. Shi HX, Yang K, Liu X, Liu XY, Wei B, Shan YF, Zhu LH, Wang C. 2010. Positive regulation of interferon regulatory factor 3 activation by Herc5 via ISG15 modification. Mol Cell Biol 30:2424-36.

67. Lu G, Reinert JT, Pitha-Rowe I, Okumura A, Kellum M, Knobeloch KP, Hassel B, Pitha PM. 2006. ISG15 enhances the innate antiviral response by inhibition of IRF-3 degradation. Cell Mol Biol (Noisy-le-grand) 52:29-41.

68. Capodagli GC, Deaton MK, Baker EA, Lumpkin RJ, Pegan SD. 2013. Diversity of Ubiquitin and ISG15 Specificity among Nairoviruses' Viral Ovarian Tumor Domain Proteases. Journal of Virology 87:3815-3827 %! Diversity of Ubiquitin and ISG15 Specificity among Nairoviruses' Viral Ovarian Tumor Domain Proteases.

69. Thiel V, Ivanov KA, Putics Á, Hertzig T, Schelle B, Bayer S, Weißbrich B, Snijder EJ, Rabenau H, Doerr HW, Gorbalenya AE, Ziebuhr J. 2003. Mechanisms and enzymes

involved in SARS coronavirus genome expression. Journal of General Virology 84:2305-2315.

70. Barretto N, Jukneliene D, Ratia K, Chen Z, Mesecar AD, Baker SC. 2005. The papain-like protease of severe acute respiratory syndrome coronavirus has deubiquitinating activity. J Virol 79:15189-98.

71. Ratia K, Saikatendu KS, Santarsiero BD, Barretto N, Baker SC, Stevens RC, Mesecar AD. 2006. Severe acute respiratory syndrome coronavirus papain-like protease: Structure of a viral deubiquitinating enzyme. Proceedings of the National Academy of Sciences 103:5717-5722.

72. Scholte FEM, Zivcec M, Dzimianski JV, Deaton MK, Spengler JR, Welch SR, Nichol ST, Pegan SD, Spiropoulou CF, Bergeron E. 2017. Crimean-Congo Hemorrhagic Fever Virus Suppresses Innate Immune Responses via a Ubiquitin and ISG15 Specific Protease. Cell Rep 20:2396-2407.

73. Holland J, Spindler K, Horodyski F, Grabau E, Nichol S, VandePol S. 1982. Rapid evolution of RNA genomes. Science 215:1577-85.

74. Mielech AM, Deng X, Chen Y, Kindler E, Wheeler DL, Mesecar AD, Thiel V, Perlman S, Baker SC. 2015. Murine Coronavirus Ubiquitin-Like Domain Is Important for Papain-Like Protease Stability and Viral Pathogenesis. Journal of Virology 89:4907-4917.

75. Daczkowski CM, Dzimianski JV, Clasman JR, Goodwin O, Mesecar AD, Pegan SD. 2017. Structural Insights into the Interaction of Coronavirus Papain-Like Proteases and Interferon-Stimulated Gene Product 15 from Different Species. J Mol Biol 429:1661-1683.

76. Daczkowski CM, Goodwin OY, Dzimianski JV, Farhat JJ, Pegan SD. 2017. Structurally Guided Removal of DeISGylase Biochemical Activity from Papain-Like Protease Originating from Middle East Respiratory Syndrome Coronavirus. J Virol 91.

77. Marthaler D, Jiang Y, Collins J, Rossow K. 2014. Complete Genome Sequence of Strain SDCV/USA/Illinois121/2014, a Porcine Deltacoronavirus from the United States. Genome Announc 2.

78. Zhang J. 2016. Porcine deltacoronavirus: Overview of infection dynamics, diagnostic methods, prevalence and genetic evolution. Virus Res 226:71-84.

79. Ran Z, Shen H, Lang Y, Kolb EA, Turan N, Zhu L, Ma J, Bawa B, Liu Q, Liu H, Quast M, Sexton G, Krammer F, Hause BM, Christopher-Hennings J, Nelson EA, Richt J, Li F, Ma W. 2015. Domestic Pigs Are Susceptible to Infection with Influenza B Viruses. Journal of Virology 89:4818-4826.

80. Sun Y, Han M, Kim C, Calvert JG, Yoo D. 2012. Interplay between interferon-mediated innate immunity and porcine reproductive and respiratory syndrome virus. Viruses 4:424-46.

81. Zhao C, Sridharan H, Chen R, Baker DP, Wang S, Krug RM. 2016. Influenza B virus non-structural protein 1 counteracts ISG15 antiviral activity by sequestering ISGylated viral proteins. Nat Commun 7:12754.

82. Guan Y, Zheng BJ, He YQ, Liu XL, Zhuang ZX, Cheung CL, Luo SW, Li PH, Zhang LJ, Guan YJ, Butt KM, Wong KL, Chan KW, Lim W, Shortridge KF, Yuen KY, Peiris JSM, Poon LLM. 2003. Isolation and Characterization of Viruses Related to the SARS Coronavirus from Animals in Southern China. Science 302:276-278.

83. Ratia K. 2008. Structure, function, and inhibition of the papain-like protease from SARS coronavirus. . Doctor of Philosophy University of Illinois at Chicago.

84. Azhar EI, El-Kafrawy SA, Farraj SA, Hassan AM, Al-Saeed MS, Hashem AM, Madani TA. 2014. Evidence for camel-to-human transmission of MERS coronavirus. N Engl J Med 370:2499-505.

85. Vergara-Alert J, van den Brand JM, Widagdo W, Munoz Mt, Raj S, Schipper D, Solanes D, Cordon I, Bensaid A, Haagmans BL, Segales J. 2017. Livestock Susceptibility to Infection with Middle East Respiratory Syndrome Coronavirus. Emerg Infect Dis 23:232-240.